FORCE-GRADIENT DETECTION OF NUCLEAR MAGNETIC RESONANCE

A Dissertation

Presented to the Faculty of the Graduate School

of Cornell University

in Partial Fulfillment of the Requirements for the Degree of

Doctor of Philosophy

by

Sean Roark Garner

August 2005

FORCE-GRADIENT DETECTION OF NUCLEAR MAGNETIC RESONANCE

Sean Roark Garner, Ph.D.

Cornell University 2005

This thesis presents experiments in which magnetic resonance is detected as a force or a force gradient on a microcantilever, a technique known as magnetic resonance force microscopy (MRFM). A new type of MRFM is described with which unprecedented sensitivity for nuclear MRFM was achieved. These experiments represent an advance in the ongoing effort to reach single-nucleus sensitivity.

First an apparatus was built in which a millimeter-scale magnetic particle was used to exert a force on paramagnetic samples which were mounted on an atomic-force-microscope cantilever. This device was used to detect electron spin resonance in diphenyl-picrylhydrazyl at 77 kelvin, and nuclear magnetic resonance in ammonium nitrate at room temperature. These experiments formed the foundation for later high-sensitivity work by providing essential information about many aspects of the apparatus.

A more advanced set-up was then created for the demonstration of a new MRFM method in which the gradient of the force from spins in the sample alters the effective spring constant of the cantilever, causing a shift in its mechanical resonance frequency. Using a custom, magnet-tipped, low-spring-constant cantilever cooled to 4 kelvin, magnetization from ^{71}Ga in GaAs was detected at a sensitivity of 7.5×10^{-21} J/T in a one-hertz measurement bandwidth, the highest nuclear-MRFM sensitivity ever reported at that time. The method has highly

favorable spin-relaxation characteristics when compared with the other existing high-sensitivity MRFM technique.

BIOGRAPHICAL SKETCH

Sean Roark Garner, first son of Margaret Roark and James Kirkland Garner, was born on November 1, 1975, in Loma Linda, California. His academic career began in earnest in 1993 at the University of California, Santa Cruz, which sits nestled in the redwoods on a hill above a meadow at the northern end of the Monterey Bay. He pursued a number of subjects—one might say far too many to succeed at any of them—and was alerted to the need for focus by failing to pass the piano-performance section of a class necessary to the music major. In 1995, Sean took time off to travel in India for a few months and returned certain that either mathematics or physics was the right major for him. Indecisive as usual, he chose to stay an extra year so as to complete both, and graduated with a B.A. in mathematics and a B.S. in physics in 1999. He then moved on to Cornell University for graduate study in physics, eventually producing the artifact you now hold in your hands.

What is a thesis? A junkyard of words. Nobody cares, man.

—Kartikeya Pant

ACKNOWLEDGEMENTS

I would like to thank the following people for their contributions to this work.

My advisor John Marohn, whose support and guidance made this thesis possible. Thanks for being a friend as well as an advisor, and for having the faith in me to let me make my own mistakes. My other committee members Paul McEuen, Jeevak Parpia, and Erich Mueller. Thanks especially Jeevak, for pointing me towards John's group early on, and Paul, for some much-needed career advice. All the other members of the Marohn group, especially Seppe Kuehn and Jahan Dawlaty, for all the work we did together, and Neil Jenkins, Bill Silveira, Tse Nga Ng, and Erik Muller. Zack Schlesinger, who guided me towards Cornell, and experimental physics in general. Jim Kempf, with whom I had many useful discussions. Jim, thanks for telling us all the stories about John's grad school days! David Zax, who taught me many things about NMR, experimental and theoretical. Robert "Sned" Snedeker, who gave me a great training in machining. T. Michael Duncan, who let us use his NMR magnet.

My parents, who (besides creating me, feeding me, clothing me, etc.) got me interested in science in the first place, and, more importantly, gave me confidence that I could succeed at what I tried. And thanks, Mom, for forcing me to apply to college! My brother Kirk, who always made me feel that what I was doing here was worthwhile. Thanks for being an all-around cool dude.

Karyn, who reminded me that grad school is not the most important thing in life. Thanks for saying yes when I asked you to marry me!

All the friends I've made while I was here, Bill, Ivan, Steve, Étienne, Carrie, Connie, Maurizio, Hande and many more. I would especially like to thank Ivan Daykov for destroying my car in the Trumansburg Fair demolition derby.

TABLE OF CONTENTS

LIST OF TABLES

LIST OF FIGURES

CHAPTER 1

INTRODUCTION

Magnetic resonance force microscopy (MRFM) is the name given to a variety of techniques with a common objective: to combine the spatial selectivity and chemical specificity of magnetic resonance imaging with the high-resolution scanning capabilities of scanned-probe microscopy to achieve subsurface, three-dimensional, atomic-scale imaging of solid samples. Although still somewhat distant as of this writing, this goal, and the applications it would allow, are what propel the field.

The most cited potential application by far is protein structure determination. If atomic-scale imaging were achieved with MRFM, it might be possible to read out the full three-dimensional structure of a single copy of a protein in a time on the order of hours or days. In fact, MRFM was conceived with this goal in mind. It was first proposed in 1991 by Dr. John Sidles of the University of Washington, in a paper "offered in the hope that it may eventually contribute to better treatments for intractable disorders [1]." Magnetic resonance imaging (MRI) makes sense as a candidate technology for molecular imaging because it uses a low-energy excitation—radio waves—while in principle being able to achieve extremely high resolutions. The problem lies in the small signal size: the highest sensitivity MRI experiments require imaging voxels containing at least 10^{12} nuclei [2], or 10^7 electrons [3].

The problem of protein structure determination is a significant one because with proteins, structure is the key to understanding function. While there are tens of millions of known genetic sequences [4], there are only about 31 thousand solved structures in the Protein Data Bank (PDB) [5]. Cell membrane proteins, which play crucial roles in a number of diseases, are especially poorly represented. Despite

the fact that 20-25% of all proteins are membrane proteins, only about 70 of them have solved structures (as of May 2004) [6]. The two main techniques in current use for protein structure determination, namely X-ray diffraction [7] and liquid-state nuclear magnetic resonance (NMR) [8], have had little success. If MRFM were to allow the number of solved structures to catch up with the number of sequences it could revolutionize biochemical research, and quite possibly medicine.

Another proposed application is quantum computing [9]—nuclear spins, due to their long coherence times, and the wealth of techniques for manipulating their quantum states with solid-state NMR, provide an attractive system for possible future quantum computations, with all the needed quantum gates already in place [10]. All that is missing is a method of reading out the final spin state, which, at single-nucleus sensitivity, MRFM could provide [11, 12].

In a broader sense, atomic-scale MRFM would offer a new tool whose uses can hardly be imagined at present. Much as the introduction of scanning tunneling microscopy (STM) [13] and atomic force microscopy (AFM) [14] opened up entire new fields, and in many ways changed the way science is done, a similar tool which could "see" below the surface would have the potential to reveal whole new areas of inquiry. It is this exciting sense of a potentially revolutionary new tool which motivates many researchers in the field.

1.1 MRFM basics

A schematic of a simplified MRFM experiment is given in Figure 1.1. A cantilever with a magnetic tip is placed near a sample containing magnetic nuclei (or unpaired electrons), which are polarized in an external static field, $\mathbf{B}_0$. The spins in the sample interact with the field gradient produced by the magnetic particle

on the end of the cantilever to exert a force on the cantilever. Sample magnetization can be manipulated by transverse radiofrequency (rf) magnetic fields from a nearby coil, using standard magnetic resonance techniques. This allows the force due to the sample spins to be distinguished from the myriad other forces, many of them much larger than the spin force, which act on the cantilever. Resonance occurs when the rf field's frequency is equal to the so-called Larmor frequency of the spins, which depends on the magnetic field. The field gradient from the tip therefore causes the magnetic resonance to be confined to a certain spatial region, as in magnetic resonance imaging. This region, drawn as a bowl shape in Figure 1.1, is known as the *sensitive slice*. Scanning the sensitive slice throughout the sample allows a three dimensional image to be constructed.

1.1.1 Estimate of the size of the force

The force which bends the cantilever is produced by an interaction between the magnetic dipole moment of the sample and the field gradient from the tip—the so-called gradient-dipole force, given by

$$\mathbf{F} = (\boldsymbol{\mu} \cdot \nabla)\,\mathbf{B}, \tag{1.1}$$

where $\boldsymbol{\mu}$ is the magnetic dipole moment of a spin in the sample and $\mathbf{B}$ is the field from the tip [15]. Assuming a spherical tip magnet of radius a and magnetization M, magnetized along z, if the magnet is at the origin the field at a point $\mathbf{r}$ is given in SI units by

$$\mathbf{B} = \frac{\mu_0 M a^3}{3r^3}(3(\hat{\mathbf{z}} \cdot \hat{\mathbf{r}})\hat{\mathbf{r}} - \hat{\mathbf{z}}), \tag{1.2}$$

where $\hat{\mathbf{r}}$ is a unit vector pointing along $\mathbf{r}$ (and similarly for $\mathbf{z}$), and $r = |\mathbf{r}|$ [15]. If, as in Figure 1.1, both the sample and the tip are magnetized along z, which is

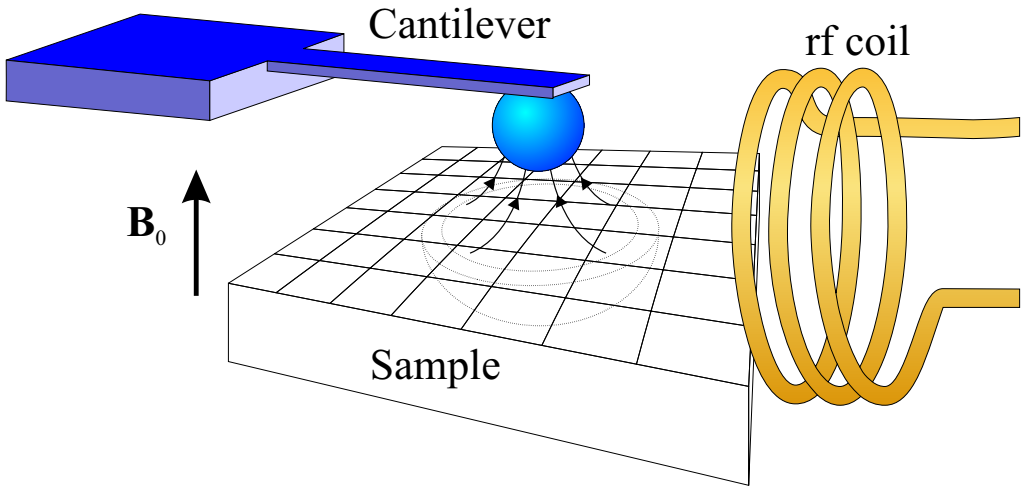

Figure 1.1: The MRFM concept: A magnet-tipped cantilever is placed near the surface of a paramagnetic sample, and is deflected by the force exerted on the tip by spins in the sample. A nearby rf coil is used to modulate the sample magnetization at the cantilever's mechanical resonance frequency, creating a resonant excitation. Resonance is confined to the bowl-shaped region, called the "sensitive slice", by the magnetic field gradient produced by the tip. The sensitive slice can be scanned throughout the sample to form and image.

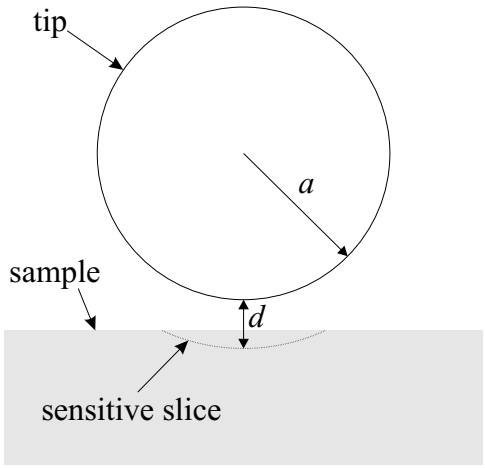

Figure 1.2: Scale diagram of idealized MRFM tip and sample.

also the cantilever's bending direction, the force between the tip and a spin in the sample reduces to

$$F_z = \mu B_{zz}, \tag{1.3}$$

where $B_{zz} \equiv \partial B_z/\partial z$ and $\mu \equiv |\boldsymbol{\mu}|$. In this case equation 1.2 gives

$$B_{zz} = 2\mu_0 M \frac{a^3}{(a+d)^4}, \tag{1.4}$$

where M is the tip magnetization, $d \equiv z - a$ is the distance from the tip's surface to the spin, and μ_0 is the permeability of free space. (The assumption of a spherical tip should be viewed as a lowest-multipole, or "far-field" approximation. Besides having the advantage of analytic tractability, this approximation is valid for many tips, and is increasingly so the larger the distance from the tip, since the higher multipole moments fall off with increasing powers of r. It also has the benefit for the experimentalist of providing a lower bound on the gradient, assuming the dipole term for the tip is estimated correctly.)

The gradient, and therefore the force, increases as the tip size is made smaller. It also increases as the spin and the tip are brought closer together. However, d

has a minimum value set by practical considerations. First, the tip will eventually contact the sample, rendering it useless as a force sensor since it can no longer bend. Also, it is often found that operating too close to the sample surface lowers the force sensitivity of a cantilever [16]. Fixing d at its minimum experimentally attainable value, there is an optimal tip size, namely $a = 3d$, obtained by maximizing equation 1.4, which gives a force of

$$F_z \approx 0.633\mu\mu_0 M \left(\frac{1}{a}\right). \tag{1.5}$$

Of course this expression could be cast equivalently in terms of a or d. (Despite the fact that d is fixed in the optimization, a is chosen in the above because this is the parameter which must be decided on beforehand; d can be adjusted during the experiment.) The above result makes the following important statement: the strength of the interaction between the tip and spins in the sample increases as the tip radius a decreases, provided the spin can be kept within $d = a/3$ of the tip's surface.

However, in apparent contradiction to this fact, in most cases the signal in MRFM experiments decreases as the tip is made smaller. The reason for this seeming paradox is that usually there is more than one spin in resonance, and the number of spins in resonance scales with cube of the tip size. The thickness t of the sensitive slice is determined by a number of factors, but it is usually inversely proportional to the field gradient from the tip. Assuming, in accordance with the analysis of the previous paragraph, that the experiment is arranged such that the distance of bottom of the sensitive slice is kept always at a depth $d = a/3$, the optimized gradient scales as $1/a$, and the thickness of the sensitive slice scales as a. The transverse extents of the slice will scale with the tip dimensions. (This is purely a geometrical fact—the slice shape will not change, and it is assumed all

distances are scaled simultaneously. See Figure 1.2) Therefore the sensitive slice volume will scale as a^3. Multiplying this factor into equation 1.5, the total signal from the sensitive slice then scales as

$$F_{\text{slice}} \propto a^2. \tag{1.6}$$

So while the per-spin single increases as the tip shrinks, the total signal decreases.

The large gradient from the tip is the key to MRFM's potential—in shrinking the tip to increase the per-spin force, the spatial resolution is also increased. However, something is lost in the exchange. The large field gradient smears out the spectral features, giving up a rich source of information about the chemical environment of the nuclei usually available in magnetic resonance[1].

A numerical example

Consider a single H nucleus, i.e. a proton ($\mu_{\text{proton}} \approx 1.4 \times 10^{-26}$ J/T [21]) interacting with a magnetic tip made of Fe ($\mu_0 M \approx 2$ T [22]), of diameter of 30 nm. This is the tip size which is optimized for a 5 nm spacing between the spin and the tip's surface. Equation 1.5 then gives $F_z \approx 1.2 \times 10^{-18}$ N. Thus the forces which characterize single-spin MRFM are in the attonewton range. (It should be said that the tip considered above is smaller than any that has been used do date in MRFM. However, tips of this size have been fabricated using a stencil-mask evaporation process [23].)

[1]Spectral information can be regained to some extent using refocusing pulse sequences [17, 18] or by placing compensating magnets around the tip [19, 20], as discussed in section 1.2.

1.2 Prior work

Initial experimental work in MRFM was performed by Dr. Daniel Rugar and coworkers at the IBM Almaden Research Center. The first demonstration of mechanical detection of magnetic resonance was in 1992, with electrons in a paramagnetic crystal [24]. Soon after, spatial scanning was added to the experiment, and the first MRFM imaging was demonstrated in 1993 [25]. Electrons were pursued first because of their relatively large magnetic moment of $\mu_e = 9.3 \times 10^{-24}$ J/T [21], almost 700 times higher than that of the proton. The first demonstration of nuclear MRFM came in 1994 [26], and three-dimensional imaging with (nuclear) MRFM was reported for the first time in 1996 [27].

A number of samples have been used in MRFM experiments, possessing different properties of interest. (Generally in MRFM experiments it is the techniques and apparatus which are under study, not the sample.) The first MRFM sample, and most widely used ESR MRFM sample, is diphenyl-picrylhydrazyl (DPPH) [24, 25, 28–34]. This organic molecule has one unpaired electron, and is widely used in conventional ESR as a "tune-up" sample [35]. Phosphorus-doped Si has also been used in ESR MRFM [36]. Later, the IBM group adopted γ-irradiated fused silica as an ESR sample [37–40]. Here, a piece of silica is bombarded with γ rays, producing defects called E$'$ centers. These dangling silicon bonds create localized states for unpaired electrons, and thus make the sample paramagnetic. This sample has the advantage of tunable paramagnetism—by changing the dose of the γ irradiation, the density of E$'$ centers can be predictably controlled.

The first sample used in nuclear MRFM was the inorganic salt ammonium nitrate (NH_4NO_3) [26, 27, 41]. Other salts have also been used, such as $(NH_4)_2SO_4$ [42], NaCl, and $Na_2C_2O_4$ [43]. In the latter experiment, 1-D imaging was demon-

strated in which the quadrupolar interactions of the ^{23}Na nuclei with the host crystal were used to create contrast. A multilayer sample consisting of NaCl and $Na_2C_2O_4$ was subjected to a "quadrupolar filter", in which the signal from ^{23}Na nuclei whose crystal environment had a strong electric field gradient was suppressed. A similar multilayer-sample, localized-spectroscopy experiment was performed recently, in which spin-echo (or Hahn-echo) spectroscopy was used to distinguish $Ba(ClO_3)_2{\cdot}H_2O$ from $(NH_4)_2SO_4$ [17]. Salts have been a popular sample because of their relatively large spin relaxation times at room temperature. Other nuclear MRFM samples include CaF_2 [44] and paraffin [45]. GaAs has been used in recent years [43, 46–48]. In [47], Thurber *et al.* demonstrated increased sample magnetization in GaAs by optical pumping.

In 1996 the group of P. Chris Hammel, then of the Los Alamos National Laboratory, demonstrated force-detected ferromagnetic resonance (FMR) for the first time, in a yttrium iron garnet (YIG) film [49], and later in Co [50]. FMR imaging of a ferromagnetic sample was performed by the IBM group in YIG [32] and by Hammel's group in Co [51]. More recently, the group of Olivier Klein at CEA in Saclay, France has performed a number of FMR MRFM studies on YIG, investigating the effect of the magnetic tip on the FMR spectra [52, 53] and making quantitative measurements ferromagnetic resonance in a single crystal of YIG [54, 55].

1.2.1 Techniques

Tip configuration

In early experiments the sample was affixed to the cantilever, and the magnetic field gradient source (usually referred to as the "tip", even when not at the end of a cantilever) was placed nearby. In this "sample-on-cantilever" configuration

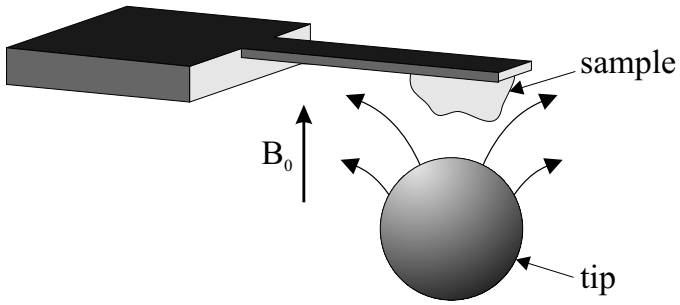

Figure 1.3: In the sample-on-cantilever configuration a sample is affixed to the cantilever and a relatively large magnetic tip is placed nearby.

(see Figure 1.3) a very large tip magnet can be used, which produces a lower field gradient, and therefore a thicker sensitive slice—as mentioned in section 1.1 this results in a lower per-spin force, but a higher signal overall, due to the large resonant volume. When magnetic resonance techniques, and not sensitivity, are the focus of an MRFM experiment, the sample-on-cantilever configuration is still often used. However, it was always understood that the magnet must eventually be moved to the tip. One reason is that as the tip is made smaller the problem of locating it with respect to the cantilever becomes formidable. Also, a "magnet-on-cantilever" microscope allows more general samples to be studied, which is important as MRFM moves toward application.

Magnet-on-cantilever MRFM was demonstrated by both Rugar's [32], and Sidles's [33] groups in 1998. The latter experiment featured a $\sim$ 1 µm SmCo tip magnet, which produced a field gradient of 2.5×10^5 T/m, about 10^7 times as large as the field gradients used in medical magnetic resonance imaging [33] and 10^4 times as large as those obtained in microcoil NMR imaging [2, 56]. This experiment was a powerful demonstration of the sensitivity of MRFM—with a fairly simple apparatus, and what is by today's standards a relatively low-sensitivity can-

tilever, a sensitivity of 184 electron magnetic moments in a one-hertz measurement bandwidth was achieved.

Besides a lower overall signal strength, another obstacle to the widespread adoption of magnet-on-tip MRFM is that there are a number of interactions which can cause spurious cantilever excitation, obscuring the spin signal. Placing a ferromagnet on its tip couples the cantilever to any applied static and time-dependent fields, which can cause, for instance, shifts in the cantilever resonance frequency with applied field [57], and increased energy dissipation which lowers the effective quality factor of the cantilever and therefore its sensitivity [58]. However, it has been shown that by making the field parallel to the easy magnetization axis of the tip, but perpendicular to the plane of cantilever motion, that these effects can be minimized [48, 59, 60]. The experiments described in Chapter 5 of this thesis were performed in this manner.

Radiofrequency excitation

A number of strategies have been used to produce the rf field required for resonant spin excitation. The first MRFM experiments used a coil similar to that in conventional NMR, with the difference that the coil was smaller and the sample was outside the coil [24, 26]. An open-coil design was introduced in 1996 by Zhang *et al.* [61]. This allows the sample to be placed inside the coil, and a scanned tip to have access to the sample from above. Although the performance of the coil was quite reasonable, $\sim$ 11.5 G at 0.5 W as estimated by the authors, the design has not been adopted by any other groups, possibly due to its relative complexity of fabrication. In ESR and FMR experiments, where frequencies in the few-GHz range are often required, microwave microstripline resonators have also

been used [32, 36, 37, 50, 51]. Still, the original coil design, or variants thereof, has always been the standard. A superconducting Nb coil design has recently been used in cryogenic experiments [39,40,62]. A coil design with printed-circuit-board based tuning circuitry, which was used in cryogenic nuclear MRFM experiments [48], will be discussed in Chapter 5.

In MRFM the interaction between the rf field and the sample is always modulated in some manner. The cyclic saturation [36, 63, 64], cyclic adiabatic rapid passage [26], and OSCAR [38] techniques will be described at some length in Chapters 3, 4, and 5 respectively, and so will not be here. There are, however, some other methods which merit mention.

Steady-state sample magnetization M_z depends on the external field B_0, as well as the amplitude B_1 and frequency ω of the rf field, so any of these quantities may be modulated to create the desired modulation of the magnetization (see section 2.2.5). For samples with short spin-relaxation times steady-state magnetization is reached quickly [65]. IN DPPH, for example, this occurs in tens of ns [35]. This makes it possible to modulate M_z in the kHz range or faster while remaining steady-state, giving rise to a whole class of MRFM modulation schemes. (Nuclei usually have spin-relaxation times too large for these methods to apply. Therefore almost all nuclear MRFM experiments have used cyclic adiabatic rapid passage, a non-equilibrium technique. See Chapters 4 and 5 for explications of the main modulation methods used for nuclei.)

In the first ESR MRFM experiment B_0 was modulated to create a modulation of the sample magnetization at the cantilever mechanical resonance frequency f_0 [24]. But rather than modulating B_0 directly at the cantilever frequency, which could have created spurious excitation of the cantilever, the authors modulated B_0 at

$f_0/2$. Because M_z is a nonlinear function of B_0, a component of modulation at f_0 (and all higher harmonics of $f_0/2$) was produced. This technique was used in ESR MRFM experiments for about two years [24, 25, 28].

A related technique was developed by Sidles and coworkers [29], in which B_0 and B_1 are both modulated. The nonlinear dependence of M_z mixes these to produce, among other contributions, a component at the sum of the modulation frequencies. In this way a modulation of M_z at a frequency which is not a harmonic of the modulation frequencies of either B_0 or B_1 can be produced. For this reason the technique is known as "anharmonic modulation". Anharmonic modulation was used for many years by Sidles's and Hammel's groups [29–31, 33, 49, 50, 61]. In a related approach, Marohn *et al.* showed that it is possible to achieve anharmonic modulation by simultaneously modulating the rf amplitude B_1 and the position of a small ferromagnet [34].

Also used in a few MRFM experiments was FM cyclic saturation, in which the applied rf frequency ω is modulated at the cantilever mechanical resonance frequency f_0 [32, 36]. For spins in a given field, the steady-state magnetization M_z is a peaked function of ω, so when ω is on the steep sides of the peak, a modulation is produced. The modulation has opposite phases on two sides of the peak, producing a so-called "derivative" lineshape when coherent cantilever detection is used.

Imaging

Imaging in MRFM was first accomplished by scanning the sensitive slice throughout the sample, resulting in a force map which is a convolution of the spin density of the sample and the shape of the sensitive slice. A real-space image of the spin

density is then obtained by deconvolving the shape of the sensitive slice from the force map. This was initially demonstrated by the IBM group in two dimensions, with the assumption of a paraboloid sensitive slice [25]. Later, a fourth-order approximation to the tip field profile multiplied by a theoretical magnetic resonance lineshape was used to create a model of the sensitive slice. The parameters were then adjusted to be self-consistent with the observed force maps, and three-dimensional images were recovered. The third spatial dimension was obtained by changing the external field value, which changes the distance between the sensitive slice and the tip. This technique produced a resolution of 3 µm for ^{1}H spin density in ammonium nitrate [27], and 5 µm for electrons in DPPH [32].

Another imaging method has been proposed by Kempf and Marohn, in which local spin density information from within the slice can be obtained without scanning the entire sample [18]. In this scheme, a series of rf pulses is delivered to the sample which reduce the resonance linewidth by cancelling spin evolution due to dipolar interactions and chemical shift [66]. Between the pulses the tip is shifted back and forth laterally, producing field shifts during in-plane spin precession. The shuttling of the tip is timed in such a way that the effects of the field shifts on the spin evolution accumulate rather than cancel. The end result is a distribution of magnetization which depends sinusoidally on displacement in the shuttling direction. The total magnetization of the slice is then measured by MRFM methods. Repeating this experiment a number of times, with different in-plane spin evolution times, produces a data set which can be Fourier transformed to produce a real-space spin-density map of the slice.

Recently, Chao *et al.* demonstrated an alternative deconvolution-based image reconstruction scheme [67]. In their algorithm a convolution of the slice shape

with an ansatz spin density is performed, and the result is used to construct a new ansatz in an iterative process. This procedure produced a reconstructed sample volume with an 80 nm voxel size in DPPH.

Gradientless MRFM

A unique force-detection approach is BOOMERANG, which stands for *better observation of magnetization, enhanced resolution, and no gradient* [19]. Here, the magnetic tip moves on a flexible membrane and is surrounded by an annulus of fixed magnetic material. By the superposition principle, a force can still be exerted on a nearby spin by the field gradient from the tip, even though the magnetic annulus cancels the total gradient at the sample. The advantage is that, without the highly inhomogeneous tip field smearing out the spectrum, high resolution NMR spectroscopy can be performed. This technique has recently been demonstrated with a mm-scale apparatus [20].

1.2.2 Ultrasensitive MRFM and single-electron detection

In section 1.1 it was shown that with an extremely small magnetic tip, a single proton will produce a force on the order of one attonewton on the cantilever. With presently attainable tips ($\sim$ 100 nm) and tip-sample distances (tens of nm), one electron spin creates a force of similar size. The cantilevers available "of the shelf" for AFM and related techniques are not able to detect forces in this range, and so it was always understood that creating custom cantilevers designed for high force sensitivity is of the main experimental objectives MRFM.

As will be seen in section 2.3.2 there are many ways to engineer cantilevers for high sensitivity. For example, one strategy is to increase the resonance frequency of

the cantilever. In the past decade researchers have become steadily more proficient at creating oscillators, usually of the doubly-clamped beam, rather than cantilever, type, which have resonance frequencies in the high-MHz range [68, 69]. Recently an oscillator of this type was created which had a mechanical resonance frequency of 1 GHz [70]. Unfortunately these devices have thus far not had very high force sensitivities because of their low quality factors. Researchers have had some success increasing the quality factor by chemical surface modification [71–73], but so far they have not been sensitive enough for application to MRFM.

Torsional oscillators, which twist instead of bend, can have very large quality factors. In the double-torsional (DT) design, two paddle-like sections, the "head" and "wings", rotate with opposite phase, trapping energy in the head. Figures as high as $Q \sim 10^8$ have been reported at low temperatures in centimeter-scale oscillators [74], and DT oscillators have been pursued for this reason as MRFM sensors [45]. Sub-millimeter-scale torsional oscillators have been used in MRFM experiments [45, 75], but so far seem to be similar in sensitivity to cantilevers, and somewhat harder to use. (In these experiments the spins created a force on a torsional oscillator, which should not be confused with experiments in which magnetic resonance is used to induce a torque in a cantilever [76].)

Another strategy for increasing sensitivity is decreasing the cantilever's spring constant. So far this has been the most successful method of creating high-sensitivity cantilevers for MRFM. It seems clear that for a static force, lower spring constant is better—the cantilever will deflect more for a given force. This is also true it turns out for oscillating forces (see section 2.3.2), and so low-spring-constant cantilevers have become a central tool for MRFM.

An extremely important advance in MRFM technique was the realization of

extremely low-spring-constant, or "ultrasoft" cantilevers. In collaboration with the IBM group, graduate student Timothy Stowe, working with Prof. Tom Kenny of Stanford, introduced this technology in 1997 [77,78]. These cantilevers have spring constants $\sim 10^3$ times smaller than those of commercially available cantilevers. In 2001 one of these cantilevers, cooled to 110 mK with a dilution refrigerator, was used to detect some of the smallest forces ever reported, in the sub-attonewton range [79]. Initially it seems impossible that these cantilevers could be applied to MRFM—they are so soft that if they are brought near the surface of a sample in the usual AFM geometry, as in Figure 1.1, they will be drawn by van der Waals and static electrical forces into contact with the surface, making them useless as force detectors. For this reason they must be used perpendicular to the surface [80]. In this orientation the force from a uniformly magnetized symmetric sample will cancel to zero—every spin on one side of the cantilever will be offset by another spin on the other side. However, for nonuniform spin distributions this is not a problem, and as will be seen below, these are not only common, they are ubiquitous.

With the invention of ultrasoft cantilevers, the last pieces seemed to be falling into place for single-electron MRFM. Initial details such as creation of a transverse rf field in a cryogenic force detection experiment had already been worked out. A sample with controllable electron density, so that a single-spin signal could be unambiguously identified, had already been found in γ-irradiated silica. Various tip fabrication strategies had been tested [58], and it was found that focussed-ion-beam milling (FIB) of a hand-glued, micron-size rare-earth magnet could produce sufficiently high field gradients [38].

Unfortunately a new problem had emerged. As the tip was brought near the sample, the relaxation times of the electrons became shorter [38]. Shorter relax-

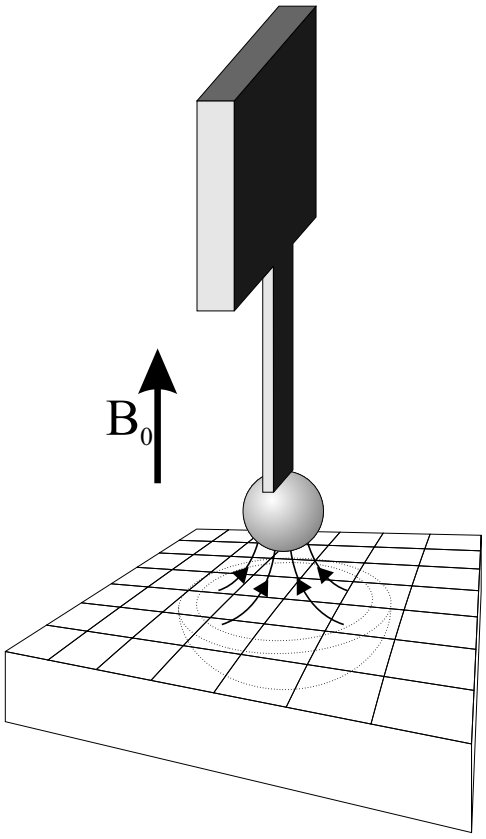

Figure 1.4: Ultrasoft cantilevers must be oriented perpendicular to the sample surface. In this configuration the lateral force from a uniformly magnetized planar sample cancels by symmetry. This can be overcome by exploiting statistical imbalances in the sample magnetization, or by using a force gradient to detect the spins, as described in chapter 5.

ation times mean a larger measurement bandwidth, and therefore a lowered SNR. It was not clear how the tip was relaxing the spins. Thermal magnetic moment fluctuations of the tip magnet seemed an obvious candidate. However, theoretical work had previously indicated that with a magnetic tip made from a high-anisotropy magnetic material, such as PrFeB, this effect would be negligible [81]. Furthermore, fluctuations in the tip magnetic moment can can be measured by the fluctuating forces they induce in the cantilever [58] and were found to be too small to account for the effect [38]. It was later realized that the origin of the spin relaxation was mechanical—high-frequency, upper-harmonic modes of the cantilever were shaking the tip and causing fluctuating fields at microwave frequencies [82]!

This was soon remedied with the introduction of mass-loaded cantilevers, and ESR MRFM with a sensitivity of 6 electron magnetic moments was demonstrated [39]. An ultrasoft cantilever with a thick silicon mass near its end was used. The magnetic tip was made from the hard magnet SmCo, a particle of which was glued to the end of the cantilever and sharpened with FIB to $\sim$ 1 µm in size. The cantilever was perpendicular to the sample surface, so how was a deflection produced? In any ensemble of N spins, although the equilibrium magnetization is constant on average, at any given time there are fluctuations of order $\sqrt{N}$ away from the mean. This will create an imbalance in the magnetization on the two sides of the cantilever, which can produce a deflection. So any sample may be used for perpendicular-cantilever MRFM, provided sufficient sensitivity is available to detect these fluctuations. A problem with this effect is that the sign of the spin imbalance is random, and fluctuates in time, so its average will be zero. To remedy this a positive quantity such as the power spectrum of each data set is taken, and a number n of data sets are averaged. The result is that the signal is always positive,

but the averaged SNR only grows as $n^{1/4}$ [39, 83].

Less than a year later MRFM was used to detect magnetic resonance from a single electron spin [40]. The main differences from the "6-spin" experiment [39] were a smaller tip and the sample—in order to have unambiguous detection of a single spin, it was necessary to create a silica sample with extremely low E′ center density, so that the average number of spins in the sensitive slice was much less than one. Because of the $n^{1/4}$ scaling, in order to achieve a signal of ~ 5 standard deviations above the background noise the authors had to average for 13 h per point! However, the 1/4 power also means that a factor of x increase in single-shot SNR will mean a factor of x^4 lower averaging time—only a factor of 15 increase in SNR is required to reduce the averaging time of this experiment to 1 s.

1.3 Summary and outline

The realization of single-electron MRFM by Rugar *et al.* [40] was a huge accomplishment, and a major milestone for MRFM. It was the culmination of 13 years of work by many researchers, a time during which many technical obstacles were overcome. Some, like the need to develop highly sensitive cantilevers and small, high-gradient magnetic tips were anticipated. Others, such as the relaxation of sample spins by tip motion upper cantilever modes, were not. But the real prize—single-nucleus MRFM—remains unrealized, and the methods used in the single-electron experiment are probably not extendable to single-proton MRFM. Nuclear MRFM presents its own distinct set of challenges, and it will require many years of hard work before single-proton magnetic resonance can be achieved.

This thesis presents a number of MRFM experiments, beginning with the development of the apparatus, and culminating in work which, until very recently,

represented the highest sensitivity ever reported for nuclear MRFM, equivalent to $\sim 6 \times 10^5$ proton magnetic moments in a one-hertz measurement bandwidth. The structure in some ways mirrors the history of MRFM—relatively low-sensitivity sample-on-cantilever experiments with DPPH and ammonium nitrate give way to highly sensitive, magnet-on-cantilever experiments using ultrasoft cantilevers at cryogenic temperatures. The overall form is as follows:

- **Chapter 2** establishes a number of theoretical results used throughout the thesis. First a discussion of magnetic resonance is given, which begins with a derivation of the Curie law and a quantum justification of the classical vector picture of magnetic resonance. This vector description is then used to describe a number of magnetic resonance techniques used in the experiments of the later chapters. The magnetic resonance section closes with a qualitative discussion of relaxation theory. Cantilever dynamics are then considered in terms of a damped harmonic oscillator model. A number of important expressions are obtained, including the noise behavior of a cantilever in thermal equilibrium, which leads to an expression for the minimum detectable force in a thermally limited force measurement. Finally the design of high-sensitivity cantilevers is discussed.

- **Chapter 3** begins with detailed description of the apparatus used in Chapters 3 and 4. ESR MRFM experiments, performed on DPPH at $\sim$ 80 K in the sample-on-cantilever configuration, are described. An estimate of rf field strength in the rotating frame is made from power broadening of the observed ESR spectrum.

- **Chapter 4** gives an account of room-temperature nuclear MRFM studies

on ammonium nitrate. Important modifications to the rf generation apparatus are described. A digitally generated rf scheme is demonstrated to have sufficiently low phase noise for MRFM use, making possible arbitrary pulse sequences and frequency and phase modulations. Pulsed NMR MRFM is used to measure the rf field strength in the rotating frame.

- **Chapter 5** describes a new type of MRFM experiment in which a force gradient created by sample spins shifts the resonance frequency of a magnet-tipped cantilever. An estimate of the expected signal size is made in the context of a single-spin experiment and compared with the OSCAR technique. Then high-sensitivity nuclear MRFM experiments are described in which ^{71}Ga NMR is detected in GaAs at liquid helium temperatures, using a ferromagnet-tipped, custom-fabricated, ultrasoft cantilever. A magnetic moment sensitivity of 7.5×10^{-21} J/T, equivalent to $\sim 5 \times 10^5$ proton magnetic moments, is demonstrated in a one-hertz measurement bandwidth. Finally numerical calculations which elucidate the experimental observations are presented.

CHAPTER 2

THEORETICAL BACKGROUND

2.1 Introduction

This chapter establishes a number of theoretical results used in later chapters. In many cases, the derivations here are intended to provide some missing steps in the somewhat abbreviated treatment found in most texts. Section 2.2 lays out the main concepts of magnetic resonance used in later chapters. In section 2.3 the dynamics of a cantilever, modeled as a damped, driven harmonic oscillator is treated. A number of important results for force detection are obtained, such as an expression for the force noise in a thermally-limited measurement.

2.2 Spin dynamics and magnetic resonance

This section gives a brief discussion of some important topics in magnetic resonance. First, it is shown that a quantum mechanical treatment of a spin interacting with a static field leads to an expression identical to the classical equation of motion for a magnetic dipole. Next the Curie law for thermal polarization in an external field is derived for arbitrary spin quantum number. Then the effect of an alternating field is considered, and the resonance phenomenon appears. As will be seen, the alternating field case also admits a classical vector treatment. After adding empirical relaxation terms to the spin equations of motion (leading to the Bloch equations), a number of magnetic resonance phenomena, important to experiments later in this thesis, are described in terms of the classical expressions. The section ends with a qualitative discussion of magnetic resonance, based on the BPP theory.

2.2.1 Quantum-mechanical spin in a magnetic field

The angular momentum of a quantum-mechanical spin can be described by the vector operator $\mathbf{S}$ with components S_x, S_y, and S_z, obeying the commutation relation

$$[S_x, S_y] = i\hbar^2 S_z, \tag{2.1}$$

and those derived by cyclic permutations of the operators[1]. The squared magnitude of this operator S^2 commutes with any one of its components, say S_z, and so simultaneous eigenstates of both are possible. The eigenstates can be written $|s, m_s\rangle$, s where the spin quantum number, and m_s is the z-component quantum number. The eigenvalues are of the form

$$S^2 |s, m_s\rangle = \hbar s(s+1) |s, m_s\rangle , \tag{2.2}$$

and

$$S_z |s, m_s\rangle = \hbar m_s |s, m_s\rangle , \tag{2.3}$$

where m_s is in the range $-s, -s+1, \ldots, s-1, s$.

The magnetic moment of the spin is related to this angular momentum by a proportionality constant known as the gyromagnetic ratio, defined by

$$\boldsymbol{\mu} \equiv \gamma \mathbf{S}. \tag{2.4}$$

The interaction of a spin with a magnetic field $\mathbf{B}$ is described by the simple Hamiltonian

$$H = -\boldsymbol{\mu} \cdot \mathbf{B}. \tag{2.5}$$

Taking the field to be along z with strength B_0, this reduces to

$$H = -\gamma S_z B_0. \tag{2.6}$$

[1]See, for example, Shankar [84]

The time dependence of the various components of $\mathbf{S}$ can now be determined using the Heisenberg equation, along with equation 2.1. For S_x,

$$\begin{aligned} \frac{dS_x}{dt} &= \frac{i}{\hbar}\left[H, S_x\right] \\ &= -\frac{i\gamma B_0}{\hbar}\left[S_z, S_x\right] \\ &= \gamma B_0 S_y. \end{aligned} \tag{2.7}$$

Similarly for S_y,

$$\frac{dS_y}{dt} = -\gamma B_0 S_x. \tag{2.8}$$

Since S_z commutes with itself it is not time dependent under this interaction. Combining these gives for the time dependence of the magnetic moment,

$$\begin{aligned} \frac{d\boldsymbol{\mu}}{dt} &= \gamma\frac{dS_x}{dt}\hat{\imath} + \gamma\frac{dS_y}{dt}\hat{\jmath} + \gamma\frac{dS_z}{dt}\hat{k} \\ &= \gamma^2 B_0 S_y \hat{\imath} - \gamma^2 B_0 S_x \hat{\jmath}. \end{aligned} \tag{2.9}$$

Since $\mathbf{B} = (0, 0, B_0)$ the above expression can be written in the suggestive form

$$\frac{d\boldsymbol{\mu}}{dt} = \gamma\left(\boldsymbol{\mu} \times \mathbf{B}\right). \tag{2.10}$$

Although calculated here for the simple case of $\mathbf{B}$ pointing along z, this equation holds for general $\mathbf{B}$. For a macroscopic ensemble of spins $\boldsymbol{\mu}$ can be replaced by its ensemble average $\mathbf{M} \equiv \langle\boldsymbol{\mu}\rangle$ to get the macroscopic equation

$$\frac{d\mathbf{M}}{dt} = \gamma\left(\mathbf{M} \times \mathbf{B}\right), \tag{2.11}$$

which gives the behavior of the sample magnetization. It will precess about the external field, exactly as one expects for a classical magnetic moment. This is the justification for using a classical analysis of many magnetic resonance phenomena.

2.2.2 Thermal polarization

Assume that a large number N of spins is in equilibrium with a bath at temperature T. The spins are assumed to be spatially distinct, so Maxwell-Boltzmann statistics are appropriate. In this case, using again the Hamiltonian of equation 2.6, the number of spins in a state with z-component quantum number m_s is

$$n(m_s) = N\frac{e^{\frac{\gamma\hbar m_s B_0}{k_\mathrm{B}T}}}{Z}, \tag{2.12}$$

where k_B is Boltzmann's constant and Z is the partition function, given by

$$Z = \sum_{m_s=-s}^{s} e^{\frac{\gamma\hbar m_s B_0}{k_\mathrm{B}T}}. \tag{2.13}$$

The expectation value of the z magnetization of the entire sample is then

$$\begin{aligned} \langle M_z \rangle &= \sum_{m_s=-s}^{s} n(m_s)\gamma\hbar m_s \\ &= \gamma\hbar N \sum_{m_s=-s}^{s} m_s \frac{e^{\frac{\gamma\hbar m_s B_0}{k_\mathrm{B}T}}}{Z}. \end{aligned} \tag{2.14}$$

In the high-temperature limit (the validity of which will be considered at the end of the section) the exponential can be approximated

$$e^{\frac{\gamma\hbar m_s B_0}{k_\mathrm{B}T}} \approx 1 + \frac{\gamma\hbar m_s B_0}{k_\mathrm{B}T}, \tag{2.15}$$

which gives

$$\begin{aligned} \langle M_z \rangle &\approx \frac{\gamma\hbar N}{Z} \sum_{m_s=-s}^{s} m_s \left(1 + \frac{\gamma\hbar m_s B_0}{k_\mathrm{B}T}\right) \\ &= \frac{\gamma^2\hbar^2 B_0 N}{k_\mathrm{B}TZ} \sum_{m_s=-s}^{s} m_s^2 \\ &= \frac{\gamma^2\hbar^2 B_0 N}{k_\mathrm{B}TZ} \frac{s(s+1)(2s+1)}{3}. \end{aligned} \tag{2.16}$$

The partition function becomes

$$\begin{aligned} Z &= \sum_{m_s=-s}^{s} 1 + \frac{\gamma\hbar m_s B_0}{k_{\mathrm{B}}T} \\ &= \sum_{m_s=-s}^{s} 1 = 2s+1, \end{aligned} \tag{2.17}$$

which, divided into equation 2.16 gives

$$\langle M_z \rangle = \frac{N\gamma^2\hbar^2 s(s+1)}{3k_{\mathrm{B}}T} B_0. \tag{2.18}$$

This formula is known as Curie's law, and gives the familiar linear dependence on the magnetic field strength.

For consistency it should be verified that the approximation made in equation 2.15 is a reasonable one, which relies on the second term in equation 2.15 being small. For a proton (^{1}H nucleus) in an 8 T field at 4 K, a reasonable set of assumptions, we have $\gamma = 2.68 \times 10^8$ m/As, $s = 1/2$, so

$$\frac{\gamma\hbar m_s B_0}{k_{\mathrm{B}}T} \approx 2 \times 10^{-3}, \tag{2.19}$$

so using the high-temperature approximation is valid in this case.

2.2.3 Alternating transverse fields and the rotating wave approximation

In magnetic resonance experiments the sample magnetization is manipulated using alternating transverse magnetic fields. As will be seen in what follows, by making an appropriate transformation the dynamics can be described by a classical vector equation similar to equation 2.10. The alternating field adds a term to the Hamiltonian of the form

$$H_{\mathrm{alt}} = -\gamma S_x B_x \cos\omega t, \tag{2.20}$$

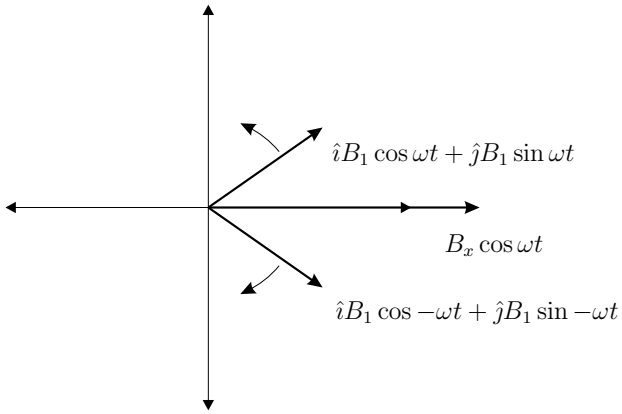

Figure 2.1: Decomposition of an oscillating field into two rotating fields. The magnitude of the rotating field is half that of the alternating field, i.e. $B_1 = B_x/2$.

if the alternating field is assumed to lie along x. To ease calculations, one can decompose the alternating field B_x into two *rotating* fields with amplitude $B_1 = B_x/2$, as in Figure 2.1. The Hamiltonian for the counterclockwise rotating field can be written in the form

$$\begin{aligned} H_{\text{rot}} &= -\gamma \left(S_x B_1 \cos\omega t + S_y B_1 \sin\omega t \right) \\ &= -\gamma \left(e^{-\frac{i}{\hbar}\omega t S_z} S_x B_1 e^{\frac{i}{\hbar}\omega t S_z} \right). \end{aligned} \tag{2.21}$$

(The second equality will not be proved here, see [85] for a derivation.)

At this point an approximation is made, known as the *rotating-wave approximation*, that the other (clockwise) rotating field component can be neglected. (The validity of this assumption will be considered later.) In this case the following replacement can be made:

$$S_x B_x \cos\omega t \rightarrow B_1 e^{-\frac{i}{\hbar}\omega t S_z} S_x e^{\frac{i}{\hbar}\omega t S_z}, \tag{2.22}$$

in H_{alt}, resulting in the total Hamiltonian, including the static field contribution

as in equation 2.6,

$$H(t) = -\gamma \left(S_z B_0 + B_1 e^{-\frac{i}{\hbar}\omega t S_z} S_x e^{\frac{i}{\hbar}\omega t S_z} \right). \tag{2.23}$$

The time dependence can be removed from this equation by entering an interaction picture, in which the states of the system evolve according to

$$\begin{aligned} \psi_r &= e^{\frac{i}{\hbar}\omega t S_z}\psi, \\ \psi &= e^{-\frac{i}{\hbar}\omega t S_z}\psi_r. \end{aligned} \tag{2.24}$$

This is equivalent to entering a frame of reference which rotates about the z axis at a frequency ω, known as the *rotating frame*. The Schrödinger equation is then

$$\begin{aligned} i\hbar\frac{\partial\psi}{\partial t} &= -\gamma \left(S_z B_0 + B_1 e^{-\frac{i}{\hbar}\omega t S_z} S_x e^{\frac{i}{\hbar}\omega t S_z} \right) \psi \\ \omega S_z e^{-\frac{i}{\hbar}\omega t S_z}\psi_r + i\hbar e^{-\frac{i}{\hbar}\omega t S_z}\frac{\partial\psi_r}{\partial t} &= -\gamma S_z B_0 e^{-\frac{i}{\hbar}\omega t S_z}\psi_r - \gamma B_1 e^{-\frac{i}{\hbar}\omega t S_z} S_x \psi_r \\ \omega S_z\psi_r + i\hbar\frac{\partial\psi_r}{\partial t} &= -\gamma S_z B_0 \psi_r - \gamma B_1 S_x \psi_r. \end{aligned} \tag{2.25}$$

The second expression is obtained by substituting equations 2.24, the third by multiplying through by $\exp(-i\hbar\omega t S_z/\hbar)$, which commutes with S_z. Rearranging the above gives the final form for the interaction-picture Schrödinger equation,

$$i\hbar\frac{\partial\psi_r}{\partial t} = -\gamma \left(B_0 + \frac{\omega}{\gamma} \right) S_z\psi_r - \gamma B_1 S_x \psi_r. \tag{2.26}$$

This time-independent equation causes the transformed ψ_r to evolve under an effective field given by

$$\mathbf{B}_{\text{eff}} = B_1\hat{\imath} + \left(B_0 + \frac{\omega}{\gamma} \right)\hat{k}. \tag{2.27}$$

Figure 2.2 is a diagram of this effective field in the rotating frame. As ω goes to $-\gamma B_0$ the transverse field dominates the Hamiltonian. This is the resonance phenomenon, and the frequency $\omega_0 \equiv -\gamma B_0$ is known as the *Larmor frequency*.

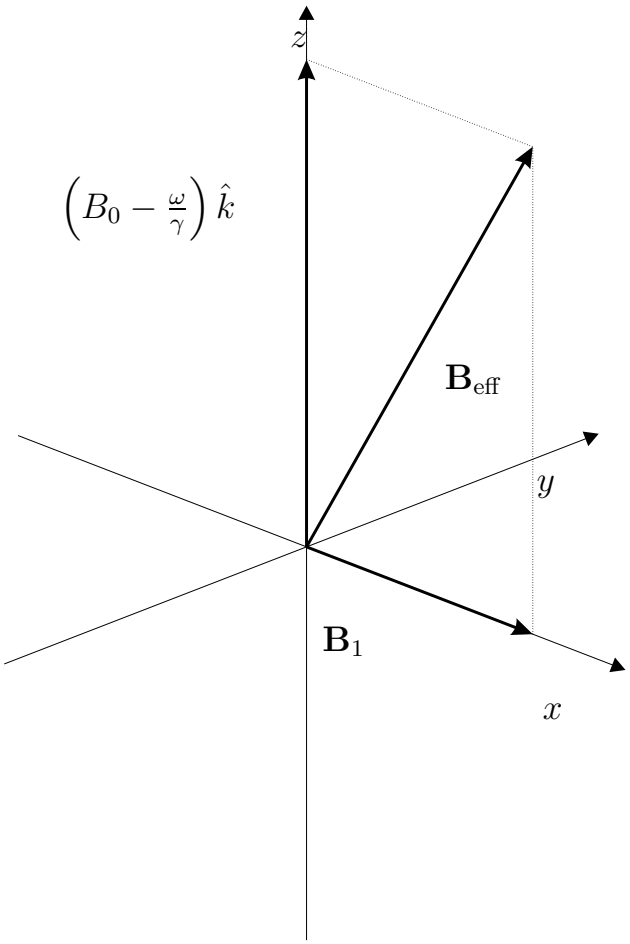

Figure 2.2: The effective field in the rotating frame. The effective field $\mathbf{B}_{\text{eff}}$ is the vector sum of the transverse field $\mathbf{B}_1$ and the transformed external field $(B_0 + \omega/\gamma)\,\hat{k}$, where ω is the frequency of the rotating field.

Note that when ω is far from ω_0, then $\mathbf{B}_{\text{eff}} \approx \mathbf{B}_0$, justifying the earlier assumption that the other rotating field component can be ignored. In general the minus sign in dropped from the expression for the Larmor frequency in experimental settings, and will be in this thesis.

The dynamics in the rotating frame are entirely determined by the static, transformed field $\mathbf{B}_{\text{eff}}$. Therefore, the rotating-frame Hamiltonian can be written,

$$\frac{d\boldsymbol{\mu}}{dt} = \gamma\left(\boldsymbol{\mu} \times \mathbf{B}_{\text{eff}}\right), \tag{2.28}$$

or, for an ensemble,

$$\frac{d\mathbf{M}}{dt} = \gamma \left(\mathbf{M} \times \mathbf{B}_{\text{eff}} \right), \tag{2.29}$$

So the entire quantum dynamics, including the alternating transverse field, can be reduced to a classical vector equation by entering a rotating frame. This important result will allow an intuitive classical description to be used in the discussion of magnetic resonance phenomena which follows.

2.2.4 Bloch equations

The above analysis indicates that a spin will simply precess around the effective field for all time. In actual experiments, however, there are dissipative interactions with the environment which introduce relaxation. Although there is a large body of theory on the exact description of these interactions, in general they are too complicated, and varied from system to system, to make a first-principles derivation worthwhile. In practice empirical relaxation rates are added to the description of the system, based on observations of the behavior of the spins.

A spin system in an arbitrary magnetization state, but in contact with a thermal reservoir, is observed to relax exponentially to the thermal polarization given in section 2.2.2, in a time known as the *spin-lattice relaxation time*, or T_1. The name comes from the fact that the spins are exchanging energy with their surroundings, the "lattice". This behavior is described, in the absence of external fields, by a term which causes the magnetization to decay to the thermal equilibrium value M_0:

$$\frac{dM_z}{dt} = \frac{M_0 - M_z}{T_1}. \tag{2.30}$$

Similarly it is observed that the x and y components of the magnetization tend to decay to zero with a different characteristic time, called the *spin-spin relaxation*

time, or T_2. This is due to energy-conserving spin flips, so no energy is exchanged with the lattice. This is expressed (again without external fields) by terms of the form

$$\begin{aligned} \frac{dM_x}{dt} &= -\frac{M_x}{T_2}, \\ \frac{dM_y}{dt} &= -\frac{M_y}{T_2}. \end{aligned} \tag{2.31}$$

Combining these terms with those given by equation 2.29, assuming that the transverse field is along x, gives

$$\frac{dM_z}{dt} = -\gamma M_y B_1 + \frac{M_0 - M_z}{T_1} \tag{2.32}$$

$$\frac{dM_x}{dt} = \gamma M_y \left(B_0 + \frac{\omega}{\gamma} \right) - \frac{M_x}{T_2} \tag{2.33}$$

$$\frac{dM_y}{dt} = \gamma M_z B_1 - \gamma M_x \left(B_0 + \frac{\omega}{\gamma} \right) - \frac{M_y}{T_2}, \tag{2.34}$$

known as the Bloch equations. These equations give a sufficient description of the behavior of most systems of interest in magnetic resonance.

2.2.5 Steady-state response

Setting the derivatives to zero in the Bloch equations and solving gives the steady-state solution. The solution for the z component of the magnetization is [86]

$$M_z = M_0 \frac{1 + (\omega - \omega_0)^2 T_2^2}{1 + \gamma^2 B_1^2 T_1 T_2 + (\omega - \omega_0)^2 T_2^2}. \tag{2.35}$$

Recall that M_0 is the thermal magnetization. In Chapter 3 this formula will be used to describe an electron spin system in which the approximation $T_1 \approx T_2$ is valid (see section 3.3.2). In this case the expression reduces to

$$M_z = M_0 \frac{1 + (\omega - \omega_0)^2 T_1^2}{1 + (\gamma^2 B_1^2 + (\omega - \omega_0)^2) T_1^2}. \tag{2.36}$$

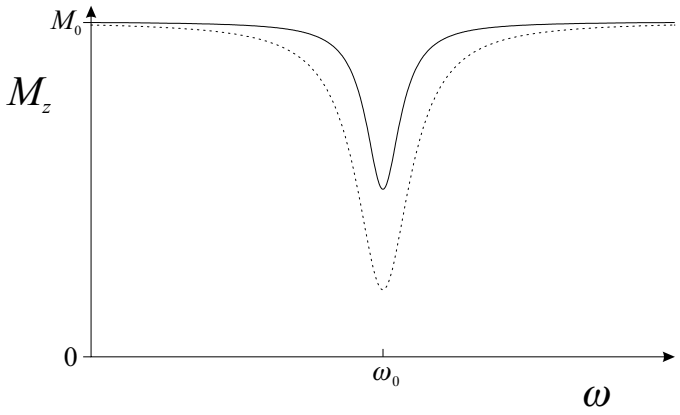

Figure 2.3: A plot of steady-state z magnetization given by equation 2.36 for two values of B_1. The dotted curve represents a B_1 twice as large as that of the solid curve. With a larger B_1, both a stronger reduction of magnetization and a broader response are observed.

Figure 2.3 shows the steady-state z magnetization given by equation 2.36 as a function of frequency. The dashed curve represents a B_1 twice as large as in the solid curve. At the larger B_1 value a "deeper" response, i.e. a larger reduction of M_z is observed. This resonant reduction of the steady-state z magnetization is known as *saturation*. Also, with a larger B_1 the response is wider, a phenomenon is known as *power broadening*.

2.2.6 Pulsed NMR

In pulsed NMR, the rf field is applied for a time much shorter than both T_1 and T_2. Relaxation effects can then be ignored, so this situation corresponds to setting $\mathbf{B}_{\text{eff}} = \mathbf{B}_1$ in equation 2.29. If the system starts in thermal equilibrium, i.e. $M_z = M_0$, $M_x = M_y = 0$, then the magnetization will precess about $\mathbf{B}_1$ in the rotating frame for as long as the rf field is on. This rotation is called *nutation*. The frequency of this precession is given by $\omega_{\text{R}} = \gamma B_1$, and is known as the *Rabi*

frequency.

Following the pulse, the transverse components of the magnetization will no longer be zero, and will precess in the external field B_0. In conventional NMR spectroscopy this is used to create an induction current in the rf coil, which is coupled back out of the system and Fourier transformed to provide information about the sample [85, 86].

Pulses are named by the tip angle they induce in the magnetization vector with the z axis. So for instance a pulse which tips the magnetization vector into the plane is called a "$\pi/2$ pulse".

In practice there are other terms in the Hamiltonian besides the external field terms (equation 2.29). For instance the spin might have magnetic dipolar interactions with other spins nearby. For this reason, in order for the simple reasoning of the preceding paragraph to hold, the rf field must be strong enough that the effective field term dominates the Hamiltonian. In solids this means giving very strong rf pulses, with B_1 of order tens of G.

2.2.7 Spin locking and adiabatic rapid passage

Imagine than the magnetization vector lies along x, and that the rf field is exactly on resonance. In this case equation 2.27 reduces to

$$\mathbf{B}_{\text{eff}} = \mathbf{B}_1 = B_1\hat{\imath}, \tag{2.37}$$

and the magnetization vector and the effective field are parallel. Therefore there will be no precession of $\mathbf{M}$ in the rotating frame, it will simply remain lying along $\mathbf{B}_1$. In this case it is said that the magnetization is "locked" to $\mathbf{M}$, and the experimental practice is called *spin-locking*.

Note that the equilibrium magnetization in this situation is not equal to the thermal polarization along the static field, M_0. In general it is much smaller, due to the fact that $B_1 \ll B_0$ in most cases. Therefore replacing B_0 with B_1 in equation 2.18 gives a much smaller equilibrium magnetization. The magnetization is observed to equilibrate to its rotating-frame equilibrium value in a time called $T_{1\rho}$, the *spin-lattice relaxation time in the rotating frame*.

Now consider the following experiment. Starting with $\omega \ll \omega_0$, sweep the rf frequency slowly through resonance until $\omega \gg \omega_0$. In the rotating frame the effective field $\mathbf{B}_{\text{eff}}$ will begin almost parallel to B_0, and tilt slowly away from vertical. As the sweep continues $\mathbf{B}_{\text{eff}}$ will end up pointing almost opposite B_0. If the sweep is slow enough that the system remains in equilibrium at all times, or *adiabatic*, then the magnetization will follow along with the effective field and end up pointing down with its original magnitude, i.e. it will go to $-M_0$. This practice is called *adiabatic rapid passage* (ARP), and is one of the oldest techniques in NMR[2]. It can be shown that the condition for the magnetization to adiabatically follow the field is given by [65]

$$\left|\frac{d\mathbf{B}_{\text{eff}}}{dt}\right| \ll \gamma B_1^2. \tag{2.38}$$

This requirement, known as the *adiabatic condition*, is the most stringent when $\mathbf{B}_{\text{eff}}$ lies in the plane, i.e. when $\omega = \omega_0$.

2.2.8 Relaxation

This section gives a the main ideas of a theory of relaxation due to Bloembergen, Purcell, and Pound, the so-called BPP theory [87]. Although improvements have

[2]In fact, in early NMR experiments it is the field, not the rf frequency, which is adiabatically changed, but the effect is the same [65].

since been made to the understanding of specific relaxation mechanisms in various systems, the BPP theory captures the essential features of relaxation behavior.

The approach to thermal equilibrium needs only random spin flips to proceed—detailed balance takes care of the rest. The subject of relaxation theory, then, is the origin of these flips. Focusing for the moment on spin-lattice (T_1) relaxation, the BPP theory assumes (1) Spin flips occur due to fluctuations in the field at the location of each nucleus, called the *local field*, at the Larmor frequency. (2) These fluctuations arise from the thermal motion of magnetic dipoles in the sample. (3) Thermal motions of neighboring nuclei are random, and characterized by a correlation time τ_c.

Quantum or semiclassical methods can be used to quantify assumptions (1) and (2) with the following result [88]: the relaxation time inversely proportional to the spectral density of fluctuations in the local field $J(\omega)$ at the Larmor frequency. That is,

$$T_1 \propto 1/J(\omega_0). \tag{2.39}$$

Assumption (3) is based on a model in which neighboring dipoles, such as other magnetic nuclei, undergo random thermal motion. The result is a picture in which the local field has a fluctuation spectral density $J(\omega)$ which is peaked at zero, extending out to a frequency of order $1/\tau_c$ (see Figure 2.4). The correlation time τ_c expresses how fast the dipoles in the sample move, and is a function of temperature, as well as viscosity, chain length in a polymer system, etc. As τ_c decreases, with, say, increasing temperature, the spectral density $J(\omega)$ spreads out to higher frequencies, while the area under $J(\omega)$ remains constant [88].

The qualitative prediction this makes for T_1 can be seen by examining the spectral density curves in Figure 2.4 at the Larmor frequency indicated, and considering

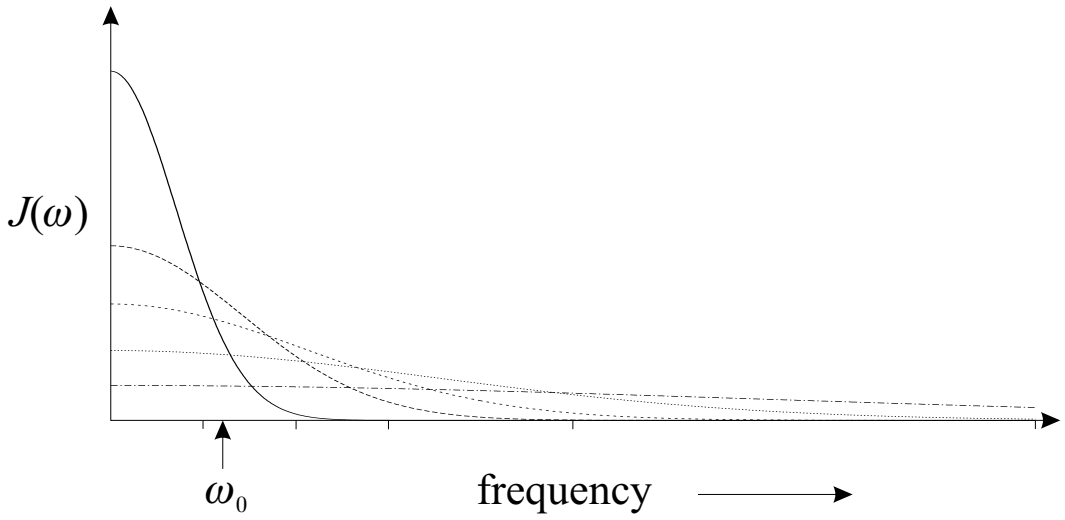

Figure 2.4: The spectral density of the local field should fall off with frequency, with width the reciprocal of the characteristic correlation time $1/\tau_c$. The correlation time for the solid curve is defined $\tau_c \equiv \tau_0$. The correlation times for the other curves are $\tau_0/2$, $\tau_0/3$, $\tau_0/5$, and $\tau_0/10$, for the long dashed, short dashed, dotted, and dot-dashed curves, respectively.

equation 2.39. Define the the largest correlation time (slowest thermal motion), indicated by the solid curve, as $\tau_c \equiv \tau_0$. As the correlation time decreases to $\tau_0/2$ (long dashed curve), the spectral density at the Larmor frequency $J(\omega_0)$ increases. This will cause T_1 to decrease. However, $J(\omega_0)$ decreases as the correlation time changes to $\tau_0/3$ (short dashed curve), and continues to decrease from there. So for large values of τ_c, T_1 is expected to decrease with decreasing τ_c, but for smaller τ_c values T_1 will increase with decreasing τ_c.

The prediction of the BPP theory is shown in Figure 2.5. As τ_c decreases at high values T_1 also decreases. The behavior reverses when $1/\tau_c \approx \omega_0$, after which T_1 increases with decreasing τ_c. The correlation time, as mentioned previously, can be associated with many physical quantities, but the present interest is temperature. The temperature will be proportional to $1/\tau_c$ [87,88], so the bottom axis in Figure 2.5 can be read as the logarithm of temperature, increasing to the right.

The predictions of the BPP theory for $T_{1\rho}$ and T_2 are similar to equation 2.39 with $J(\omega)$ evaluated at different frequencies [86,87]:

$$T_{1\rho} \propto 1/J(\omega_R), \tag{2.40}$$

$$T_2 \propto 1/J(0). \tag{2.41}$$

So, as indicated in Figure 2.5, the behavior for $T_{1\rho}$ will be the same as for T_1 but with the turnover at the Rabi frequency ω_R. At large $1/\tau_c$, i.e. high temperatures, the spectral density curve flattens out (dot-dashed curve in Figure 2.4), so one expects $J(\omega_R) \approx J(\omega_0)$, and therefore $T_{1\rho} \approx T_1$. The same can be said of T_2 at large values of $1/\tau_c$. But since $J(0)$ always decreases with increasing $1/\tau_c$ there is no turnover for T_2.

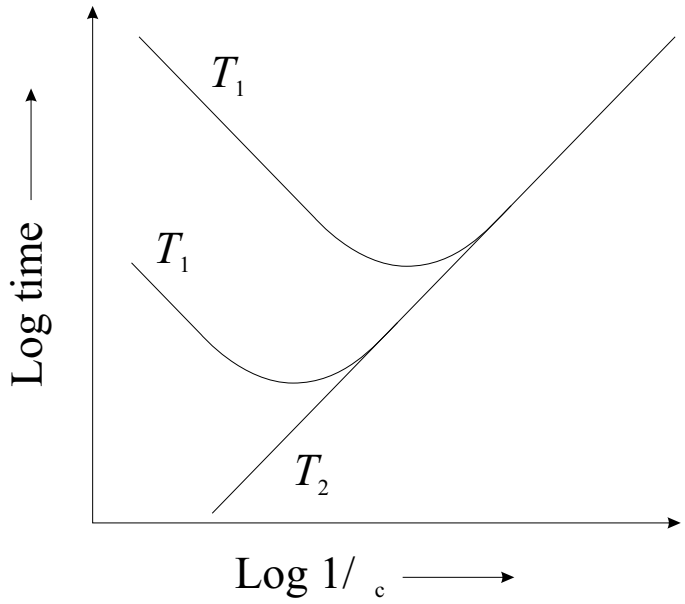

Figure 2.5: The BPP theory predicts that T_1 decreases with $1/\tau_c$ for large correlation times, and increases with $1/\tau_c$ for small correlation times, with the turnover point when $1/\tau_c \approx \omega_0$. It makes a similar prediction for $T_{1\rho}$, but with the turnover at $1/\tau_c \approx \omega_R$. The theory predicts that T_2 increases with $1/\tau_c$ for all correlation times.

2.3 Cantilever dynamics

For sufficiently small motions about its equilibrium position a cantilever is modeled extremely well as a damped harmonic oscillator. The cantilever motions considered in this thesis will always meet this criterion. In section 2.3.1 the basic features of the response of a cantilever (modeled as a damped harmonic oscillator) will be given, leading to an expression for the response of the cantilever as a function of frequency. This result will be used in section 2.3.2, where the behavior of a cantilever in thermal equilibrium is considered, resulting in the formula for the thermal excitation spectrum of the cantilever, and to an expression for the minimum detectable force for a thermal-motion limited measurement. Procedures for spring constant calibration in terms of the cantilever's thermal excitation behavior will be discussed in section 2.3.2. Finally, cantilever design will be briefly considered in section 2.3.3.

2.3.1 The damped harmonic oscillator

Newton's law for a damped harmonic oscillator of effective mass m and spring constant k is

$$m\ddot{x} + \Gamma\dot{x} + kx = F(t). \tag{2.42}$$

The coefficient Γ has units of force per velocity, and represents any frictional forces acting on the cantilever. (The effective mass m depends on details of the cantilever's shape and mass loading, so in practice it is defined dynamically, as in the expression given just after equation 2.43 below.)

Transient response

First setting $F(t) = 0$, the general solutions are found by inserting a trial solution of the form $x = \exp rt$, which gives

$$x = e^{-\frac{\omega_0}{2Q}t}\left[A_1 \exp\left(\sqrt{\left(\frac{\omega_0}{2Q}\right)^2 - \omega_0^2}\ t\right) + A_2 \exp\left(-\sqrt{\left(\frac{\omega_0}{2Q}\right)^2 - \omega_0^2}\ t\right)\right], \tag{2.43}$$

where $\omega_0 \equiv \sqrt{k/m}$ and $Q \equiv m\omega_0/\Gamma$. Cantilevers employed in experiments described in this thesis have small damping, i.e. $Q \gg 1$. In this case the quantity under the square root is negative and the solutions are of the form

$$x = e^{-\frac{\omega_0}{2Q}t}\left(A_1 e^{i\omega_1 t} + A_2 e^{-i\omega_1 t}\right), \tag{2.44}$$

where $\omega_1 \equiv w_0\sqrt{1-(1/2Q)^2}$, which is real and very close to ω_0. The difference between ω_1 and ω_0 will usually be neglected.

The initial conditions must be real, which implies $A_1 = A_2^*$. So the expression in equation 2.43 reduces to a sinusoid with a decaying envelope:

$$x(t) = e^{-\frac{\omega_0}{2Q}t} A\cos(\omega_1 t - \delta), \tag{2.45}$$

which can equivalently be written in the form

$$x(t) = e^{-\frac{\omega_0}{2Q}t}\left(X\cos\omega_1 t + Y\sin\omega_1 t\right), \tag{2.46}$$

where

$$A = \sqrt{X^2+Y^2} \tag{2.47}$$

$$\delta = \arctan\frac{Y}{X}. \tag{2.48}$$

The coefficients X and Y are known as the *quadrature amplitudes* of the oscillator. To the experimentalist these are better known as the two outputs of the lock-in amplifier. They can be written explicitly in terms of the initial position and momentum of the oscillator, $X = x(0)$ and $Y = p(0)/\omega_o m$.

Steady-state (driven) response

For the case of a nonzero driving force $F(t)$ it is useful to consider a Fourier decomposition of the cantilever displacement $x(t)$,

$$x(t) = \frac{1}{\sqrt{2\pi}} \int_{-\infty}^{\infty} \hat{x}(\omega) e^{-\omega t}\, d\omega, \tag{2.49}$$

$$\hat{x}(\omega) = \frac{1}{\sqrt{2\pi}} \int_{-\infty}^{\infty} x(t) e^{\omega t}\, dt. \tag{2.50}$$

Under this sign convention, the complex coefficient $\hat{x}(\omega)$ has a simple physical interpretation. Consider a single-frequency excitation, so that $\hat{x}(\omega') = \hat{x}_0 \delta(\omega - \omega')$. Then $x(t) = \hat{x}_0 e^{-\omega' t}$, and the in-phase and quadrature components of the motion are

$$X = \mathrm{Re}(\hat{x}_0), \tag{2.51}$$

$$Y = \mathrm{Im}(\hat{x}_0). \tag{2.52}$$

Now, let $\hat{F}(\omega)$ be the Fourier transform of $F(t)$. Fourier transforming equation 2.42 gives

$$-m\omega^2 \hat{x} - i\Gamma\omega\hat{x} + k\hat{x} = \hat{F}. \tag{2.53}$$

Solving this equation gives the mechanical transfer function

$$G(\omega) = \frac{\omega_0^2/k}{\omega_0^2 - \omega^2 - i\omega\omega_0/Q}, \tag{2.54}$$

defined by

$$\hat{x}(\omega) = G(\omega)\hat{F}(\omega). \tag{2.55}$$

With this expression the steady-state response to an arbitrary driving force can be found from a Fourier decomposition of that force.

The full solution for the oscillator's motion is obtained by adding the steady-state response, given by equation 2.54 to the solution of equation 2.45 with the appropriate initial conditions. Note that the undriven solution decays in a time $\tau \equiv 2Q/\omega_0$. For this reason it is called the *transient* response of the oscillator. If the driving force changes, a new steady-state solution must be found, and the motion under the old driving force gives initial conditions for the new transient solution. In other words, whenever the driving force on the oscillator changes, it takes a time τ for the oscillator to reach its new steady state. The time τ is known as the *characteristic time* of the oscillator.

2.3.2 Harmonic oscillator in thermal equilibrium

A harmonic oscillator is characterized by its quadratic potential energy function, $U = (1/2)kx^2$. The equipartition theorem states that this degree of freedom, when the oscillator in equilibrium at temperature T, should have average energy $k_{\mathrm{B}}T/2$. For an oscillator in motion the average potential energy can be set equal to this quantity, giving

$$\frac{1}{2}k\left\langle x^2\right\rangle = \frac{1}{2}k_{\mathrm{B}}T. \tag{2.56}$$

This result has important implications for the use of a cantilever as a measuring device in the laboratory. If the spring constant of an oscillator is known, the mean-squared displacement noise of the oscillator due to its finite temperature can be predicted. Conversely, if the temperature and mean-squared displacement can be measured, this provides a way to measure the spring constant of the oscillator.

Figure 2.6 shows the mean-squared displacement of a custom-fabricated cantilever, measured at a number of temperatures. The data have a linear dependence on temperature, in agreement with the equipartition theorem. A least-squares fit

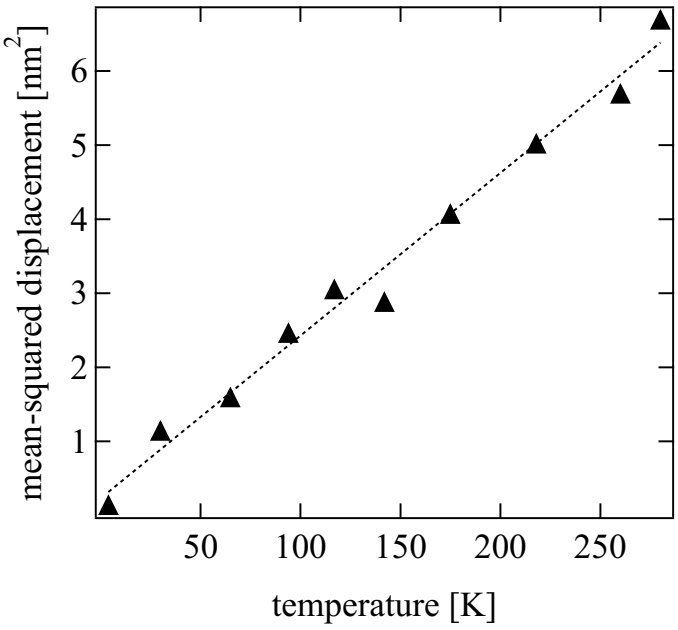

Figure 2.6: The mean-squared displacement of a custom fabricated microcantilever as a function of temperature. As predicted by equipartition theorem, a linear dependence on temperature is observed. A least-squares fit of equation 2.56 to the data (dashed line) gives a spring constant of 6.3×10^{-4} N/m.

of equation 2.56 to the data, shown in a dashed line, indicates a spring constant of 6.3×10^{-4} N/m. The line fit does not appear to pass through zero. This indicates a source of background noise which is not temperature dependent, such as voltage noise in the measurement circuitry or ambient vibrations.

Thermal spectrum

Thermal excitation is equivalent to a stochastic force driving the cantilever, the magnitude of which can be calculated using the results of section 2.3.1. Assuming that the thermal motion is due to a white driving force[3] of spectral density[4] S_F, the spectral density of the oscillator's response $S_x(\omega)$ can be written using the cantilever's transfer function (equation 2.54),

$$S_x(\omega) = |G(\omega)|^2 S_F = \frac{S_F}{k^2} \frac{\omega_0^4}{\left(\omega^2 - \omega_0^2\right)^2 + \omega^2 \omega_0^2 / Q^2}. \tag{2.57}$$

Using Parseval's Theorem (see Appendix A), the magnitude S_F may be related to the mean-squared displacement of the oscillator:

$$\left\langle x^2 \right\rangle = \frac{S_F}{k^2} \int_0^\infty \frac{\omega_0^4}{\left(\omega^2 - \omega_0^2\right)^2 + \omega^2 \omega_0^2 / Q^2} \, d\omega. \tag{2.58}$$

Performing the integral gives [89]

$$\left\langle x^2 \right\rangle = \frac{S_F}{4k^2} Q \omega_0, \tag{2.59}$$

which, through equation 2.56, gives

$$S_F = \frac{4\, k\, k_{\mathrm{B}} T}{\omega_0 Q}. \tag{2.60}$$

[3]It is assumed that the thermal driving force is zero above some very large frequency frequency $\omega_{\mathrm{cutoff}} \gg \omega_0$ so that the driving force has finite energy.

[4]In this thesis "spectral density" will always mean the single-sided power spectral density, see Appendix A.

Note that equation 2.60 can be rewritten

$$S_F = 4\,k_{\mathrm{B}}T\,\Gamma, \tag{2.61}$$

which looks very similar to the the expression for Johnson noise in a resistor, $S_V = 4\,k_{\mathrm{B}}T\,R$. The thermal noise in an oscillator is the mechanical analog of Johnson noise.

Two important results follow from the preceding discussion. The first is that a complete prediction of the power spectrum of the motion of an oscillator in equilibrium at temperature T can be written:

$$S_x(\omega) = \frac{4\,k_{\mathrm{B}}T}{k\omega_0 Q}\frac{\omega_0^4}{\left(\omega^2-\omega_0^2\right)^2+\omega^2\omega_0^2/Q^2}. \tag{2.62}$$

Secondly, if the thermal noise is the dominant source of noise in an experiment, equation 2.60 gives a quantitative prediction for the *minimum detectable force* F_{min}, defined as the rms of a force detectable with a signal-to-noise ratio (SNR) of one. If the measurement bandwidth is Δf, so the mean-squared force noise in the measurement will be given by $S_F\,\Delta f$. Therefore the definition is made $F_{\mathrm{min}} \equiv (S_F\,\Delta f)^{1/2}$, which, according to equation 2.60 is

$$F_{\mathrm{min}} = \sqrt{\frac{4\,k\,k_{\mathrm{B}}T\,\Delta f}{\omega_0\,Q}}. \tag{2.63}$$

Note that this result is not frequency dependent. The only assumption was that the measurement band is small, no statement was made about its center frequency. On resonance both the "signal" excitation and the thermal noise will be large. Off resonance they will both be smaller, but their ratio is the same at all frequencies. So why, then, are most measurements performed on resonance? Because the absolute magnitude of the response is higher there, and therefore larger in relation other sources of noise, such as amplifier noise, that do not depend on the oscillator parameters.

Equation 2.63 also suggests strategies for minimizing the minimum detectable force. The cantilever should be as cold as possible. It should also have a high quality factor, and have a low spring constant and a high resonant frequency.

Spring constant calibration

One method of spring constant calibration has already been given in Figure 2.6. However, this method is inconvenient in many experimental settings as it requires temperature-dependent measurements. When these are not available, one could simply measure $\langle x^2 \rangle$ for one temperature, and put the result into equation 2.56. However, if other sources of noise are present in the measurement apparatus they will add to the apparent mean-squared displacement, causing an underestimate of k by an unknown amount. Equation 2.62 provides an alternative method of measuring k. Evaluating at $\omega = 0$ and solving for k gives

$$k = \frac{4k_B T}{S_x(0)\omega_0 Q}. \tag{2.64}$$

In what follows it will be shown that the quantities on the right can be measured, and provide a very reliable measurement of k.

For experiments described in this thesis, the dominant source of noise after thermal cantilever vibrations is voltage noise, which is well approximated by a linear spectrum (white noise plus an approximation to a $1/f$ component) of the form $\alpha\omega + \beta$. The spectral density of the measured voltage $S_V(\omega)$ is then of the form

$$S_V(\omega) = \eta S_x(\omega) + \alpha\omega + \beta, \tag{2.65}$$

where $S_x(\omega)$ is the spectral density of the cantilever's thermal motion, and η is a distance-to-voltage conversion factor. By fitting $S_V(\omega)$ to this function using the

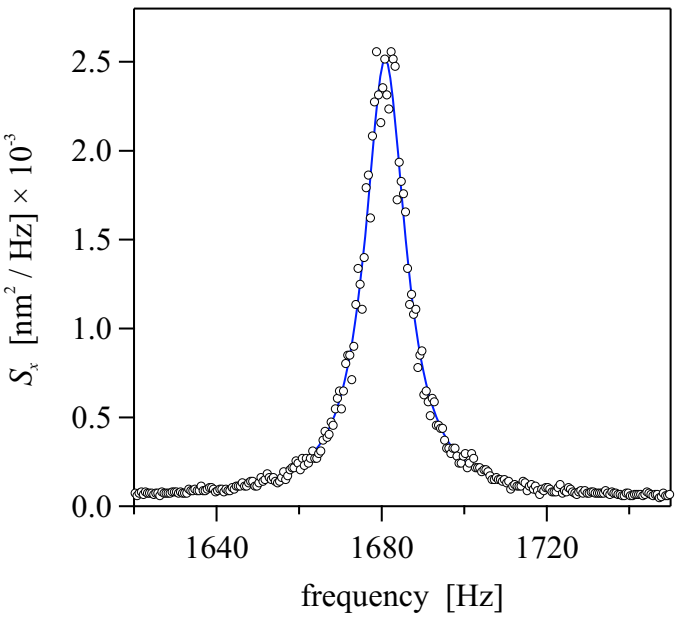

Figure 2.7: Measured thermal cantilever excitation (circles), with fit to equation 2.62 (line).

known form of $S_x(\omega)$, the background noise can be subtracted, $S_x(0)$ extracted, and k can be quite precisely determined from equation 2.64.

Figure 2.7 shows such a fit. The data (shown in circles) are obtained by sampling the output voltage of the cantilever measurement apparatus (see section 3.2.1), then using the Fourier transform to get $S_V(\omega)$. The data shown are for a commercial contact-mode AFM cantilever[5]. A fit to the data (line) provides $\omega_0 = 2\pi \times 1681$ rad/s, $Q = 141$, and $S_x(0) = 1.2 \times 10^{-25}$ m^2/Hz. Putting these values, along with a temperature of $T = 72$ K measured near the cantilever's base, gives $k = 2.1 \times 10^{-2}$ N/m. The nominal spring constant of this cantilever is 1×10^{-2} N/m, but a factor of two variation in spring constant is considered well within manufacturing tolerances [90].

[5]Veeco model # MSCT-NO, cantilever C.

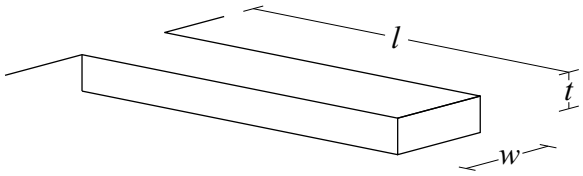

Figure 2.8: A cantilever beam showing the definitions of the length l, thickness t and width w. The cantilever is assumed to bend in the thickness dimension.

2.3.3 Cantilever design

For a rectangular beam cantilever beam of thickness t, width w and length l (see Figure 2.8),

$$k = \frac{Ewt^3}{4l^3}, \tag{2.66}$$

and

$$\omega_0 = 3.52\frac{t}{l^2}\left(\frac{E}{12\rho}\right)^{1/2}, \tag{2.67}$$

where E is the Young's modulus and ρ is the mass density of the cantilever's material [91]. Putting equations 2.66 and 2.67 into equation 2.60 gives

$$F_{\min} \propto \frac{1}{Q^{1/2}}\sqrt{\frac{w}{l}}\,t. \tag{2.68}$$

This indicates that a good strategy to lower $F_{\min}$ is to make t and w small, and l large, spending the most effort on t. In other words to fabricate cantilevers which are long, narrow and very thin, producing extremely low spring constants, but only moderately low frequencies.

As discussed in section 1.2.2, this technique has produced some of the most sensitive cantilevers ever reported [77–79, 92].

CHAPTER 3

FORCE-DETECTED ELECTRON SPIN RESONANCE

3.1 Introduction

In this chapter experiments are described in which MRFM is used to detect ESR.The apparatus developed for this purpose is described in section 3.2. (The same apparatus is used in NMR experiments described in Chapter 4.) In section 3.3 the experiments and results are discussed. A clear resonance feature is observed, and a gyromagnetic ratio estimate consistent with electrons is made. The dependence of the observed resonance on input rf power is used in section 3.3.2 to obtain an estimate of the rf field at the sample.

3.2 Apparatus

First a word on nomenclature. The part of the apparatus which consists of the vacuum system and everything inside it will be referred to as the "probe", in keeping with standard magnetic resonance terminology. The main part of the probe, which comprises all of the essential elements, such as the cantilever and rf coil, as well as the metal parts which hold these together, will be referred to as the "probe head".

The probe is designed to be used at temperatures from 4 K to 300 K, and, for rapid testing, to be narrow enough to fit into a transfer dewar[1]. Because the quality factor of the cantilever is severely reduced at atmospheric pressure, even room temperature experiments must be performed in vacuum. The overall structure is a narrow vacuum chamber, containing various components borrowed

[1]Cornell "wide" transfer dewars have ~ 1.9" clearance.

from solid state NMR and force microscopy at its bottom end, and feedthroughs for wires etc. at its top end. The design is intended for sample-on-cantilever operation, but also to admit a magnet-on-cantilever configuration if desired by switching out components.

This section will proceed in small-to-large fashion, beginning with the sensing of the cantilever's motion in section 3.2.1, working outward from there to a detailed description of the probe head in section 3.2.2, and finishing with an overview of the entire probe's structure in section 3.2.5.

3.2.1 Fiber-optic interferometer

Cantilever motion is detected using a *fiber-optic interferometer* [93,94], a method which provides quantitative and extremely sensitive displacement detection. The interferometer cavity is formed by placing the cleaved end of an optical fiber parallel to the face of the cantilever, a few tens of microns away. Cleaving the fiber, which means breaking in a way which produces a smooth face normal to the light propagation direction, can be achieved with an ultrasonic cleaving tool[2]. However, good results can also be obtained by taping the fiber to a flexible ruler in two places, nicking the fiber with an X-acto knife between the strips of tape, and bending the ruler (wetting the nick prior to bending can help with this method). Light from a 1310 nm communications diode laser is introduced into the fiber using a fiber coupler (Figure 3.1(a)). The coupler is produced (commercially) by laying two lengths of fiber parallel to each other and melting them together until their cores touch. By controlling the timing of this process various coupling ratios can be achieved. Some of the light reaching the cleaved fiber end is reflected back

[2]PK Technologies FK II.

into the fiber by the cleaved face. Most of the light exits the fiber, and some is reflected off of the cantilever face and reenters the fiber core, interfering with the light reflected from the cleave (Figure 3.1(b)). As this light propagates back up the fiber, the coupler allows it to be directed to a photodiode, the output of which is amplified. Initially a photodiode was used which was packaged for soldering into a circuit board—it had a built-in (transresistance) preamplifier, the output of which was sent to a standard op-amp amplifier circuit low passed at 200 kHz [95], and an input lens which was epoxied to a standard fiber connector jack (FC-APC) by hand. Recently this has been replaced with a commercially produced unit which has an FC-APC fiber input and BNC voltage output, and knobs which control and filtering frequencies—one of the advantages of working with communications lasers.

As shown in Figure 3.1(c), the output of a fiber-optic interferometer has a sinusoidal dependence on the distance d between the fiber face and cantilever, with wavelength $\lambda/2$, where λ is the laser wavelength. The factor of two comes from the fact that the light traverses the interferometer cavity twice, so a change in distance δd produces a change in round-trip path length of $2\delta d$. The interferometer voltage output is well described by

$$V = V_0 + \frac{V_{\text{pp}}}{2} \cos\left(\frac{4\pi d}{\lambda}\right), \tag{3.1}$$

where V_{pp} is the peak-to-peak voltage amplitude of the interferometer fringes, also called the *fringe depth*.

The interferometer uses a "90/10 coupler", meaning 10% of the light is coupled from one fiber to the other (from the top fiber to the bottom, or vice-versa, in Figure 3.1(a)). This means that 90% of the laser light is being thrown away, however this is not important—the laser can output milliwatts of power, and only

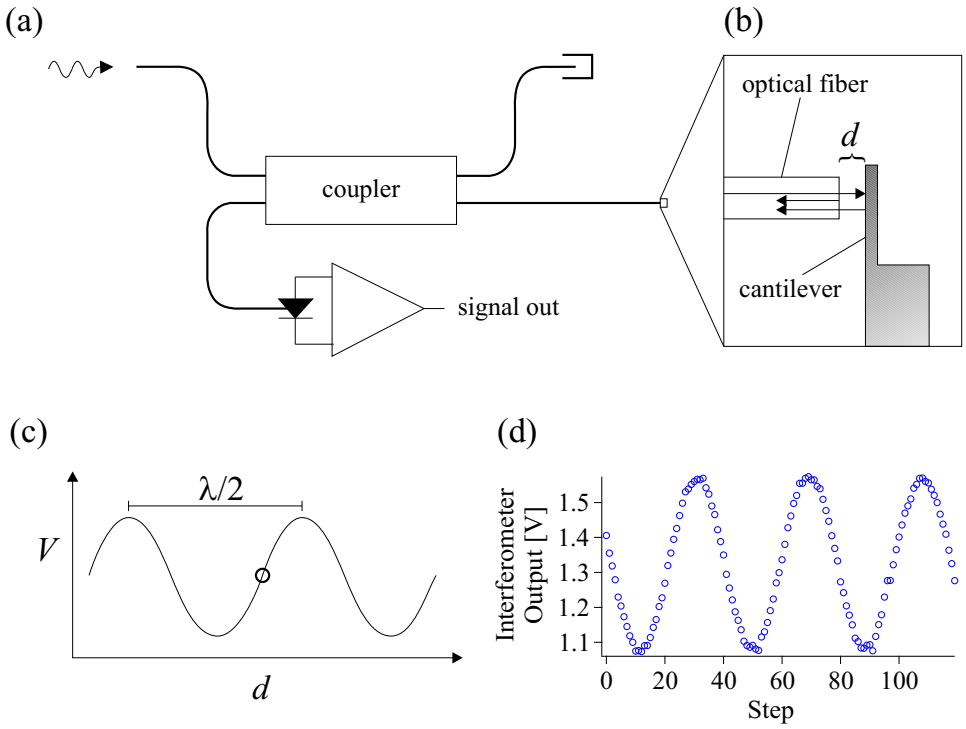

Figure 3.1: (a) Schematic of the fiber optic interferometer. Thick lines represent optical fiber. Light from a laser diode is sent to a fiber coupler. Some of the light is thrown away, and the rest is sent to the cleaved end of an optical fiber which forms an interferometer cavity with the cantilever face. The interfering light propagates back up the fiber and is collected at a photodiode on the same side of the coupler and amplified as a voltage signal. (b) The interferometer cavity formed by the cleaved end of the fiber and the cantilever face. Light reflected of the inner face of the fiber cleave interferes with light reflected from the cantilever, producing interference. (c) The output is sinusoidal in the distance between the fiber cleave and the cantilever. Sensitive displacement measurements are made in the approximately linear part of the curve indicated with a circle. (d) Output of the fiber-optic interferometer as a function of a stepped displacement.

microwatts are needed at the cantilever. More importantly 90% of the valuable reflected light, which carries the signal, is retained. Furthermore, the coupling of reflected light back into the laser, which can cause instabilities in the laser frequency, is minimized. For sensitive measurements of displacements much smaller than $\lambda/4$, the interferometer is tuned to the steep, approximately linear region of the curve indicated by a circle in Figure 3.1(c). Here, the distance dependence of the interferometer output, equation 3.1, for a small change in voltage δV, can be well approximated by

$$\delta d \cong \frac{\lambda}{2\pi V_{\mathrm{pp}}} \delta V. \tag{3.2}$$

This provides a method of calibrating the interferometer during an experiment by measuring V_{pp}, which can be accomplished by exciting the cantilever with a piezoelectric actuator mounted near its base, by manually striking the probe, or by some other method, so that its motion is large enough to span at least one interferometer fringe. This also allows a quantitative analysis of the smallest displacements which can be measured, by comparing the voltage a given displacement would produce to the voltage noise at the output. For cantilever motions in the kHz range the interferometer gives a displacement sensitivity of ~ 1 pm$/\sqrt{\mathrm{Hz}}$.

Tuning of the interferometer is achieved by adjusting the temperature, and thereby the output wavelength, of the laser diode with a thermoelectric cooler [96]. (This is evidently a popular strategy in communications technology as well, because the laser and thermoelectric cooler come packaged as one unit.) If there are of order 100 wavelengths in the interferometer cavity (round-trip), only about a 1% wavelength change is required to tune over more than one fringe, and so this difference did not need to be taken into account when calibrating the interferometer. The TEC only provides about a 1% wavelength change, so the tuning range

must be tested when aligning the fiber—if the temperature scan range is less than one fringe the fiber-cantilever distance is increased. When setting up cryogenic experiments, a range of about two fringes should be observed at room temperature since the fiber-cantilever distance can shrink considerably when cooling. The DC output of the interferometer is sometimes measured continuously during experiments and servoed with a low-frequency PI controller implemented in LabVIEW, to combat drift due presumably to thermally induced changes in the cavity length. Often, however, it is found that the interferometer cavity is stable enough that the laser temperature can be set once at the beginning of the experiment, then checked every hour or so.

The interferometer can be used for DC displacement measurements, but is less sensitive for this purpose due to $1/f$ noise in the interferometer amplifier. Figure 3.1(d) shows a number of interferometer readings taken as the cavity length was stepped. Here the cavity was not formed with a cantilever but with a reflector mounted on a coarse approach mechanism, described in section 5.3. The interferometer allowed the average step size to be measured at 8 nm, within about 10%.

3.2.2 Probe head

The probe is designed for sample-on-cantilever experiments (see section 1.2.1). The probe head essentially consists of the optical fiber, cantilever, rf coil, and a number of brass pieces designed to hold them in this configuration. However, with slight modifications to the cantilever holder and magnetic particle mount, described below, magnet-on-cantilever experiments could be performed with this apparatus as well.

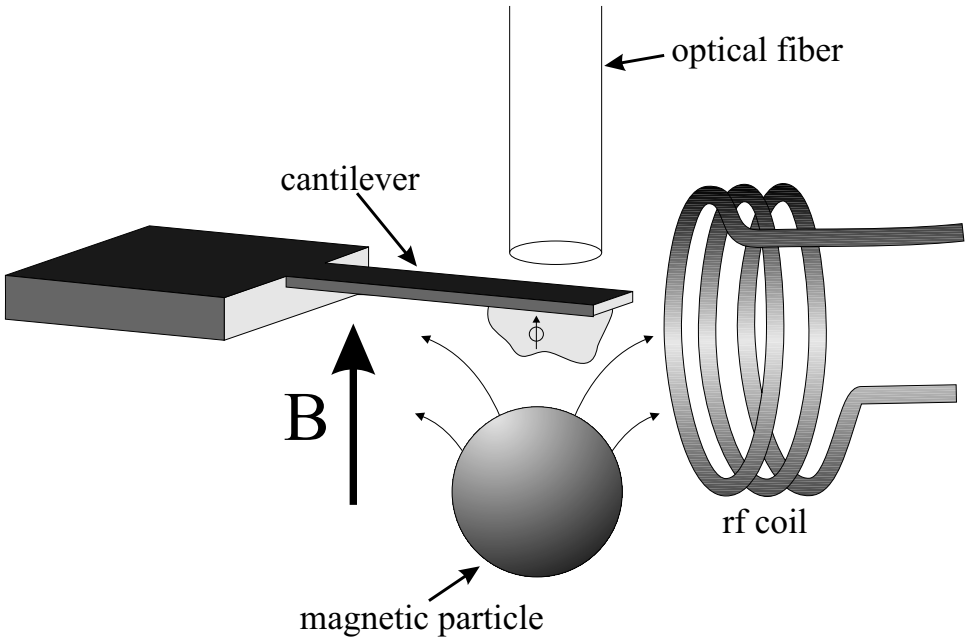

Figure 3.2: Schematic of the main experimental components. In the "sample-on-cantilever" configuration, the sample is glued to the end of the cantilever. A force is produced between spins in the sample and a magnetic particle fixed nearby.

The optical fiber is epoxied into a stainless steel tube of outer diameter 1/16", and inner diameter 0.020", and about 1.5 cm in length[3]. Epoxy is only used at the front end of the tube (the one nearest the cleaved end of the fiber) so that differential contraction does not strain the fiber when cooling to cryogenic temperatures. A tight polymer coating placed on the fiber by the manufacturer is retained to within approximately 1 cm of the cleave, to prevent nicking of the fiber by the stainless steel tube as it exits at the non-epoxied end[4]. The stainless steel tube is placed into a hole in a brass holder, shown in Figure 3.3, and held in place with a set screw. This piece also carries the cantilever, and will be referred to as the "cantilever holder".

The cantilevers used with this probe are commercially produced Si_3N_4 contact-mode AFM cantilevers [5], which protrude from a glass die about 1 mm × 2 mm × 0.5 mm in size. The cantilevers are parallel with the longest dimension of the die and bend in the direction of its shortest dimension. The fiber and cantilever are manually aligned as follows. With the cantilever holder held in a vice, a cantilever die is placed on a drop of 5-minute epoxy and the cantilever's end is aligned with the optical fiber before the epoxy sets. Alignment is judged visually by observation with a long-focal-length stereo microscope while the cantilever die's position is adjusted manually, with a toothpick or other small implement. Incoherent white light can be shone through the fiber to facilitate location of its core. The distance between the fiber and cantilever is adjusted by loosening the set screw and sliding the stainless tube in its hole. This is done beforehand using a dummy cantilever

[3]These are cut from 1-foot lengths available from Small Parts.

[4]This coating prevents the fiber from coming into contact with moisture in the air. Moisture helps cracks propagate in glass, and will make the fiber extremely brittle within a few days.

[5]Veeco model # MSCT-NO, cantilever C.

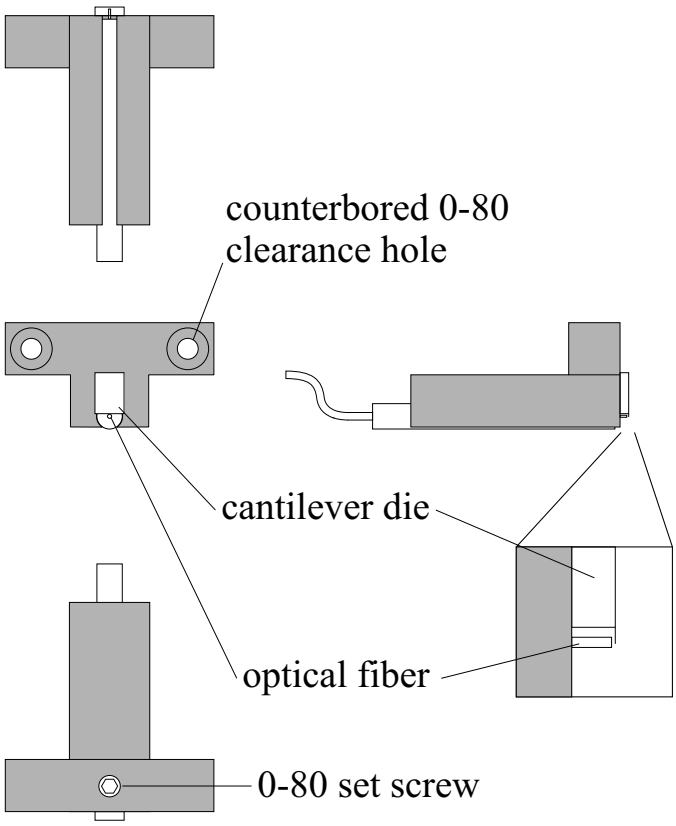

Figure 3.3: Mount which holds optical fiber aligned with cantilever, called the "cantilever holder" in the text. The optical fiber is epoxied into a stainless-steel tube, which is held into the brass cantilever holder with an 0-80 set screw. The cantilever die is epoxied to the holder. The inset shows, approximately to scale (the optical fiber is 125 µm in diameter), the completed arrangement of the cantilever and fiber.

(i.e. one which might be broken in the process without undue emotional strain on the experimenter). The inset at the right of Figure 3.3 shows a fiber aligned to a cantilever protruding from a die, drawn roughly to scale. The 125 micron cantilever can be used as a scale bar.

Once the cantilever and fiber are epoxied and set screwed, respectively, in this way, the set-up is extremely robust. If carefully aligned, the fiber will almost certainly stay aligned down to 4 K, and the epoxy rarely releases upon thermal cycling.

The position of the cantilever/fiber unit with respect to the rf coil is adjusted by means of the assembly shown in figure 3.4. The three plates shown in Figure 3.4(a) provide two orthogonal directions of motion. Plate A has three holes near its circumference through which three 1/16" brass rods pass, providing a third dimension of motion. The cantilever holder bolts to plate B (Figure 3.4(a)) via two 0-80 screws. Plate B is then clamped between plates A and C. Plate B is slightly thicker than plate C so that when the plates are assembled (Figure 3.4(b)) plates A and C do not touch. Plate A has a ledge against which the flat at the top of plate C rests, and which acts as a guide when sliding plate C. The bolts which hold the plates together pass through slots in plate C, allowing adjustment in this direction. Plate B is held down by plate C via its thin edges. Its thicker center section fits in the wide slot in the center of plate C. When the bolts are loose plate B can slide in the vertical direction in Figure 3.4. Figure 3.4(b) shows the assembled positioner. The coaxial cable which carries the rf coil is represented by the black circle.

A diagram and photograph of the probe head is shown in Figure 3.5. The positioning assembly discussed in the previous three paragraphs is labelled (ii).

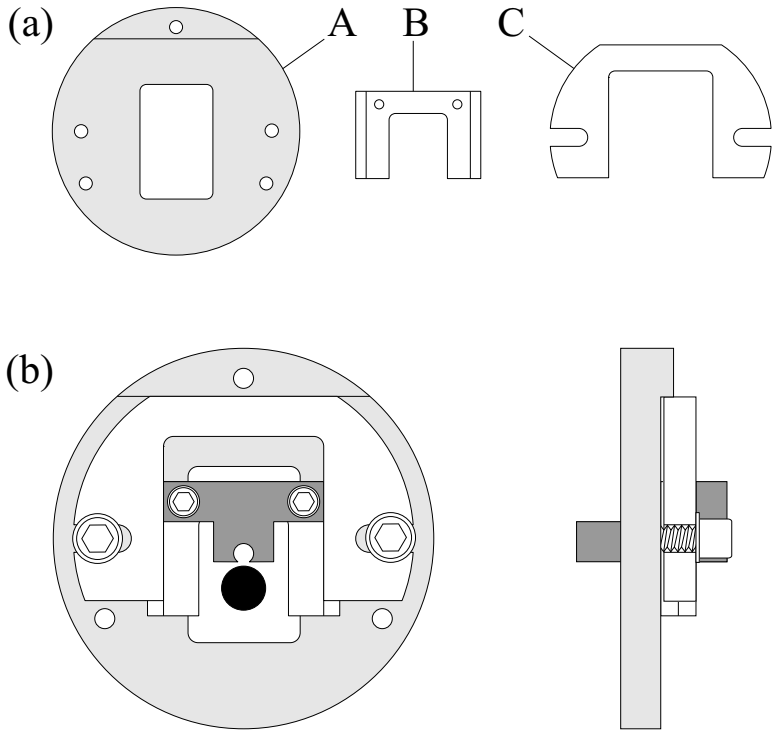

Figure 3.4: Position adjustment mechanism for the cantilever and optical fiber. (a) The three plates which make up the positioner. The cantilever holder (Figure 3.3) is bolted to plate B. Plate C is bolted to plate A with plate B sandwiched between. (b) The assembled positioner. The position of the rf coaxial cable is indicated by a black circle.

Two of the three rods which hold the assembly together are clearly visible in Figure 3.5(b). (The rods are omitted from Figure 3.5(a) for clarity.) The rf coaxial cable is clamped against two Macor rods in (i) by a nylon set screw. The nylon set screw may contract significantly upon cooling to cryogenic temperatures, but the Macor will not. As long as the contraction of the nylon screw is not so much that it loses tension, the coaxial cable will be held in position by the Macor rods. Thus this method provides a method of holding the coax which is adjustable, electrically insulating, and robust to thermal deformation. Assembly (ii) allows the cantilever/fiber combination to be located with respect to the coil, as discussed in the previous paragraph.

The annular plate (iii) bolts to the three brass rods and anchors the magnetic particle positioner assembly, which comprises also plates (iv) and (v), also annular, which are not attached to the three rods. Plate (v) is bolted to plate (iii) through wide clearance holes in plate (iv). Tightening the screws compresses springs between plates (iv) and (v), holding the magnetic particle mount between plates (iii) and (iv). The magnetic particle mount is a cylinder which passes through plates (iii), (iv), and (v), and possesses a circular flange of larger diameter which is clamped between plates (iii) and (iv). Passing through the center of the magnetic particle mount is a 2-56 screw, the head of which is visible at the lower right of Figure 3.5(b). Into the tip of this screw is drilled a small hole into which a glass capillary of O.D. approximately 0.5 mm is epoxied. The magnetic particle is epoxied into the end of this capillary. The capillary and particle are drawn in black in Figure 3.5(a).

The inset at the lower right of Figure 3.5(b) shows a closeup of the main experimental components. The cantilever die, labelled “a”, is clearly visible but

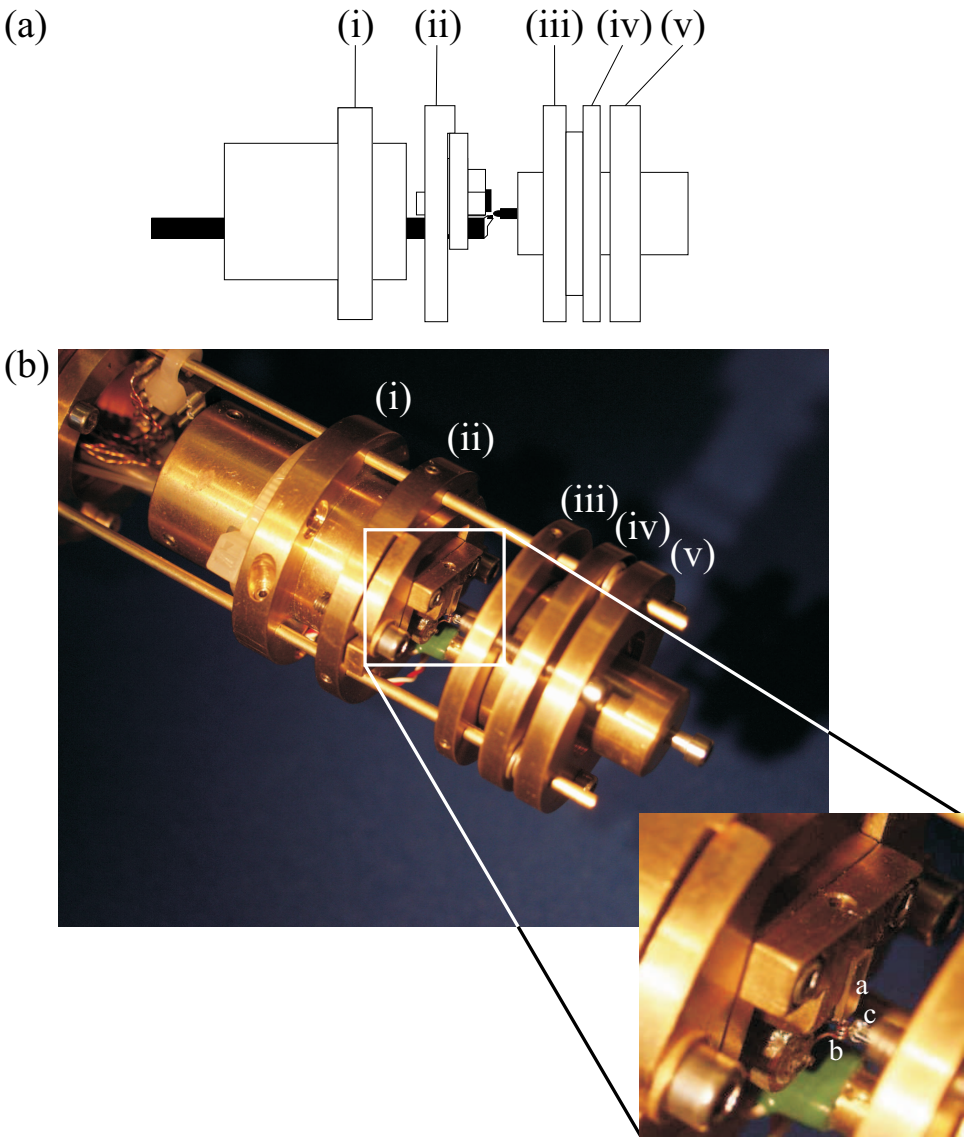

Figure 3.5: (a) Diagram and (b) photograph of probe head. The overall structure is circular plates which are clamped to three rods, not shown in (a) but clearly visible in (b). In the higher magnification inset, lower right, the cantilever die, rf coil, and the glass capillary which carries the magnetic particle are visible, labelled a, b and c, respectively.

the cantilever itself is not. The cantilever lies at the lower end of the die near the rf coil, labelled "b". The glass capillary which carries the magnetic particle is labelled "c".

3.2.3 Radiofrequency coil and matching network

The rf coil is approximately 0.8 mm in diameter, and is wound manually using one lead of a standard 1/4-W resistor as a form. The tip of the resistor lead is filed round to facilitate removal of the coil after winding. The two leads of the coil are then trimmed and tinned for soldering. The coil provides an inductance which is placed in parallel with a capacitor, called the tuning capacitor C_T, creating a resonant LC circuit. This is put in series with another capacitor, the matching capacitor C_M, in order to transform the impedance of the parallel LC to 50 Ω on resonance. This tuned and matched unit is called the *tank circuit*. The situation here is much as in conventional NMR, except the coil inductance is much smaller.

There are two reasons why a small coil is desired. First, the field inside the coil for a given current increases as the coil is made smaller. On the axis of a circular loop of wire the field is given by [15]

$$B = \frac{\mu_0 I}{2} \frac{r^2}{(r^2 + x^2)^{3/2}}, \tag{3.3}$$

where r is the radius of the loop, I is the current, and x is the distance from the plane of the loop. Note that this expression scales approximately as $r^{1/2}$. By making the coil small, then, a given field can be obtained with a relatively low current. This has two advantages. First, the power dissipated in the coil goes as I^2, so the heat deposited in the coil is reduced. In MRFM thermal stability is important in keeping the small distances between the experimental components

constant, especially in cryogenic experiments. Secondly, a low current means low voltage developed in the coil, which is important because stray electric fields can excite the cantilever.

The solenoidal formula for the field is not used because, since the sample lies outside the coil, and is often placed a distance from the coil similar to the interturn spacing, the first turn of the coil produces the majority of the field at the sample. The other turns of the coil mostly exist to create a sufficient inductance so that a resonant circuit can be practically formed. Using equation 3.3 allows an estimate of the field to be made which takes into account the coil-sample distance. And because the other turns are not considered in the estimate the experimenter is less likely to overestimate the field.

Of course, the above assumes that the current in the coil is known, which is not always the case, especially when using such a small coil—stray inductances and capacitances can become important, and the coil resistance is not necessarily the largest one in the circuit. For this reason estimates of the rf field should be made conservatively.

For a resonant LRC circuit on resonance the resistance can be written in terms of the quality factor [95],

$$R_{\text{coil}} = \frac{L\omega_{\text{coil}}}{Q}, \tag{3.4}$$

where ω_{coil} is the resonance frequency of the coil. The coil inductance may be estimated by using the solenoid formula, $L = \mu_0 N^2 A/l$, where N is the number of turns, A is the cross-sectional area of the coil, and l is the length of the coil.

The rf coil consists of 2.5 turns of 36-gauge bare Cu wire. Assuming a radius of 0.4 mm and a length of 0.8 mm, this gives an inductance of $L \approx 5$ nH. Using a Q of 175 for the tank circuit (as estimated by a reflected-power spectrum) and a

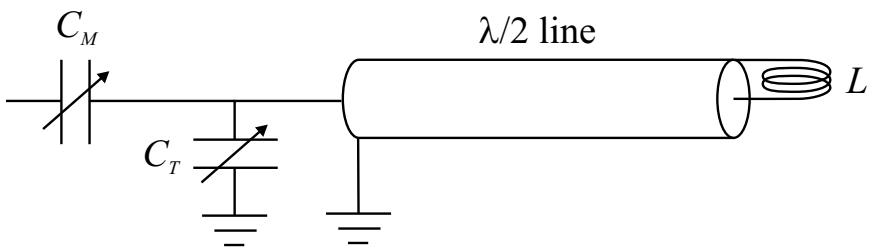

Figure 3.6: Schematic of half-wave-line radiofrequency tank circuit.

resonant frequency of $\omega_{\text{coil}} = 2\pi \times 350$ MHz, equations 3.3 and 3.4 give an estimated transverse field of 55 G at 1 W in the laboratory frame, i.e. 27.5 G at 1 W in the rotating frame at a location 0.4 mm away from the coil. (This, as will be seen in section 3.3.2, turns out to be an overestimate.)

The properties of the coil and the capacitors change with temperature. For this reason tunable C_T and C_M are used so that the tank circuit can be reliably tuned and matched at various temperatures. This presents a design problem: tunable rf capacitors are generally quite large, and placing them near the coil would make it extremely difficult to place other necessary items, such as the magnetic particle positioner, near the sample. The solution devised for this probe is to separate the coil and capacitors by a half-wave line, as in figure 3.6. A half-wave, or $\lambda/2$, line is a transmission line which is one half wavelength long for the frequency being transmitted (the wavelength calculation should take into account the reduced propagation speed of electromagnetic waves in the line). A half-wave line is in principle indistinguishable from a transmission line of zero length, so with the coil soldered at one end of the line (across the center pin and outer conductor) and the capacitors at the other, the tank circuit behaves as if the coil were directly connected to the capacitors, allowing the inconveniently large, tunable rf capacitors can be located outside of the main probe head region. The half-wave line is made

of Cu to carry heat away from the coil.

The reader may wonder, at which frequency is the line length exactly $\lambda/2$, since the resonant frequency of the tank circuit is tunable? The answer is that frequencies were chosen such that the half-wave line is slightly too short, with the effect that the impedance of the coil was rotated slightly counterclockwise. This was found to have a beneficial effect on the performance of the circuit. The inductance of the coil is so small that only the very upper end of the tuning capacitor's range could be used. With the slightly detuned half-wave line, the coil's relatively large resistance is transformed partially into an inductance, allowing more of the tuning capacitor's range to be used.

3.2.4 Vacuum system

The vacuum system for this probe is designed for pressures in the 10^{-6} Torr range, more than sufficient for preventing reduction of the cantilever quality factor, which stops improving with decreasing pressure at about 10^{-3} Torr, and sufficient for working at cryogenic temperatures.

The vacuum system is based on a 1.5" O.D. stainless steel tube about 1.5 m long. The bottom end of this tube is silver soldered to Cu ring which forms one side of a conical grease seal [97], also known as a "1-degree seal", since the conical faces of the seal are machined to an angle of approximately 1 degree. The probe head is also bolted to this ring, providing thermal contact to the outside world. There are tapped holes in the ring to which Cu braid can be bolted if more cooling is required at a specific point in the probe. To the other side of the 1-degree seal attaches a Cu cylinder, 1.5" O.D., 6" long, and capped at the bottom. The 1-degree seal closes the lower end of the vacuum system and allows quick access

to the probe head, but with much less width than would be required for a flange. It can be easily removed by hand when the system is at room pressure, and seals extremely well when the system is under vacuum (no measurable leak rate with helium leak detector).

Welded to the top of the stainless tube is a NW-40 flange which is attached to an NW-40 6-way cross. The remaining five ports of the cross hold feedthroughs for standard electrical wires, rf, optical fiber, mechanical feedthroughs to control the rf capacitors, and a valve for evacuation.

Wires are fed into the vacuum space using a hermetically sealed 19-pin military connector. A commercial o-ring based BNC feedthrough is used for rf signals. The optical fiber feedthrough is based on a Swagelok connector with its o-ring assembly replaced with a custom Teflon ferrule [98]. Rods which control the rf capacitors are passed through Swagelok o-ring seals.

3.2.5 Probe overview

Figure 3.7 shows a schematic overview of the probe. The rods which control the rf capacitors pass through an NW-40 flange at the top of the probe. Into the inside of this same flange are welded three 1/4" stainless steel rods, not shown in Figure 3.7, which forms the "backbone" of the probe structure. Radiation baffles are soldered to the rods at about 10" spacing. A stainless tube soldered into the baffles passes the wires and optical fiber down the length of the probe (there are actually two of these tubes, one for the wires and one for the fiber, but they are drawn as one in Figure 3.7 for clarity). Stainless steel, semirigid, coaxial rf cable is passed through another set of aligned holes in the baffles, and electrically isolated from them by Teflon sleeves. The rf capacitors are mounted to a plate (not shown

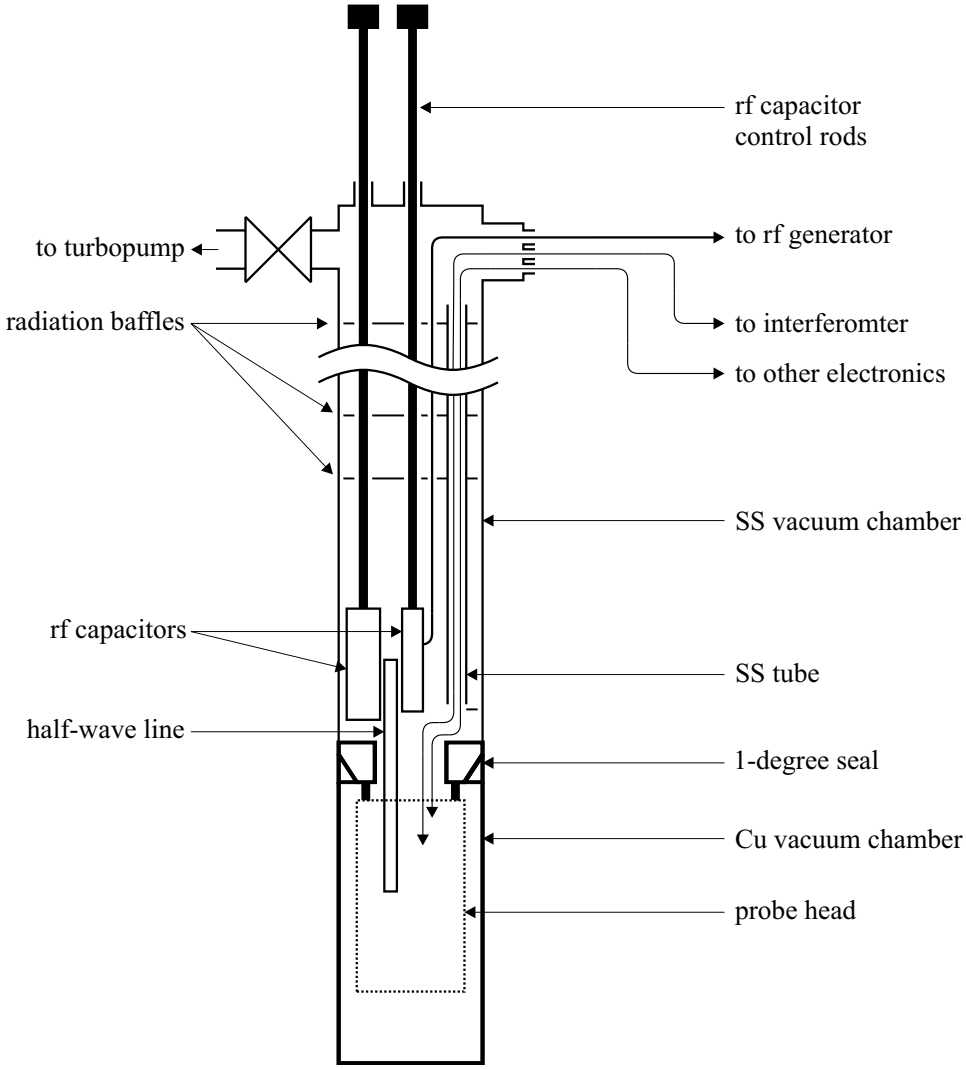

Figure 3.7: Overview of the probe in its experimental configuration.

in Figure 3.7 for clarity) which attaches to the three stainless rods via holes and set screws. The stainless rods end near the upper part of the 1-degree seal. Wires, optical fiber, and the half-wave line pass through the 1-degree seal to the probe head suspended below.

3.3 Experiment

Electron spin resonance experiments were performed using the probe described in section 3.2.

The sample was a flake of crystalline diphenyl-picrylhydrazyl (DPPH). DPPH is an organic molecule with one unpaired electron which makes ESR possible (see figure 3.8) [35]. It is widely used in the ESR community as a "tune-up" sample. It readily forms a solid, producing a much higher unpaired electron density than one usually encounters in solids. All of these qualities make it attractive as a first sample for any MRFM apparatus.

A flake of DPPH approximately 100 µm × 50 µm ×10 µm was affixed to the end of a silicon nitride (Si_3N_4) contact-mode AFM cantilever[6]. with nominal spring constant $\sim 10^{-2}$ N/m, specified by the manufacturer. The magnetic particle was a shard of AlNiCo aproximately 0.6 mm long by 0.4 mm wide. Using, as a rough estimate, a spherical shape with a diameter of 0.5 mm, a tip-sample distance of 0.3 mm, and a remanance field of 1 T, equation 1.4 gives a field gradient of $\sim 300 T/m$. Assuming a resonance linewidth of $\sim$ 20 G (see, e.g. Figure 3.11), this gives a sensitive slice width of $\sim$ 7 µm, similar to the width of the sample.

An external magnetic field was provided by a resistive electromagnet, formed by winding two layers of 16-gauge Cu magnet wire around a Cu spool on a lathe.

[6]Veeco model # MSCT-NO, cantilever C.

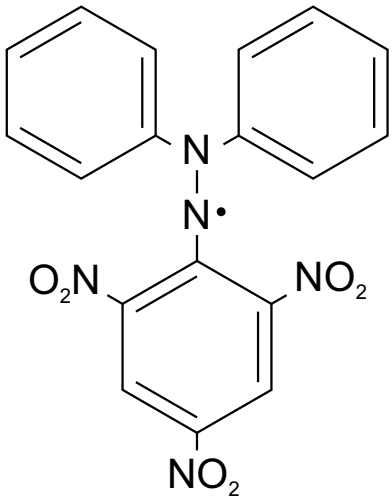

Figure 3.8: Molecular structure of DPPH. The dot indicates an unpaired electron, associated with one of the middle nitrogens, which makes the molecule paramagnetic.

The spool was machined to fit closely around the probe. The coil consisted of two layers of windings, at a turn density of 714 ± 20 turns/m, giving a coil constant of 17.9 ± 0.5 G/A.

After an initial evacuation to $\sim 10^{-6}$ Torr, the probe was backfilled with ~ 100 cc of He gas to exchange heat between the probe and the walls. The end of the probe, with the magnet mounted on it, was then submerged in liquid nitrogen (LN_2). After the probe cooled to $\sim$ 80 K, the He gas was pumped back out. Thermal contact between the probe and Cu vacuum can was somewhat weak, through the 1/16" brass rods. The probe equilibrated during experiments at $\sim$ 85 K. Since temperature was not critical in these experiments this was deemed sufficient, and Cu braid was not used.

Working in LN_2 reduced the thermal cantilever vibration noise, as well as providing a convenient way to carry heat away from the magnet. However, at magnet currents above 8 A the vibrations due to boiling of LN_2 excited the cantilever at

an unacceptable level. At the maximum practical current of 8 A, the coil was estimated to produce 143 ± 4 G in its center.

Modulation of the sample magnetization was achieved by the cyclic saturation method [24, 36] (see Figure 3.9). The rf field was turned on and off at a frequency f_{mod}. When the rf was on the sample magnetization was partially saturated, as described in section 2.2.5, reducing the magnetization to some value M_{sat}. When the rf was turned off, the thermal polarization recovered in a time T_1, which is tens of ns for electrons in DPPH [35]. As long as $T_1 < 1/f_{\mathrm{mod}}$ there should be some modulation of the sample magnetization. Here f_{mod} was set to the cantilever resonance frequency f_c, a few kHz, so $T_1 \ll 1/f_{\mathrm{mod}}$, and the modulation of the sample magnetization was nearly square.

The rf was generated by an HP signal generator, the output of which was fed to a TTL-controlled rf switch (see Figure 3.10). The switch was controlled by the TTL output generated by the reference of the lock-in amplifier (Stanford SR830). The lock-in was set to internal reference mode, and the reference frequency was set to f_c, measured just before the experiment. When the rf frequency coincided with the Larmor frequency of the electrons in part of the sample, the intermittent rf signal modulated the sample magnetization, producing an oscillating force between the sample and the magnetic particle. This oscillating force caused a resonant excitation of the cantilever, which was measured with the fiber-optic interferometer and demodulated with the lock-in.

For a reference frequency which is exactly equal to f_c, the response of the cantilever should be $\pi/2$ out of phase with the drive signal. Therefore the signal should be concentrated entirely in the quadrature ("Y") channel of the lock-in output, with none in the in-phase ("X") channel.

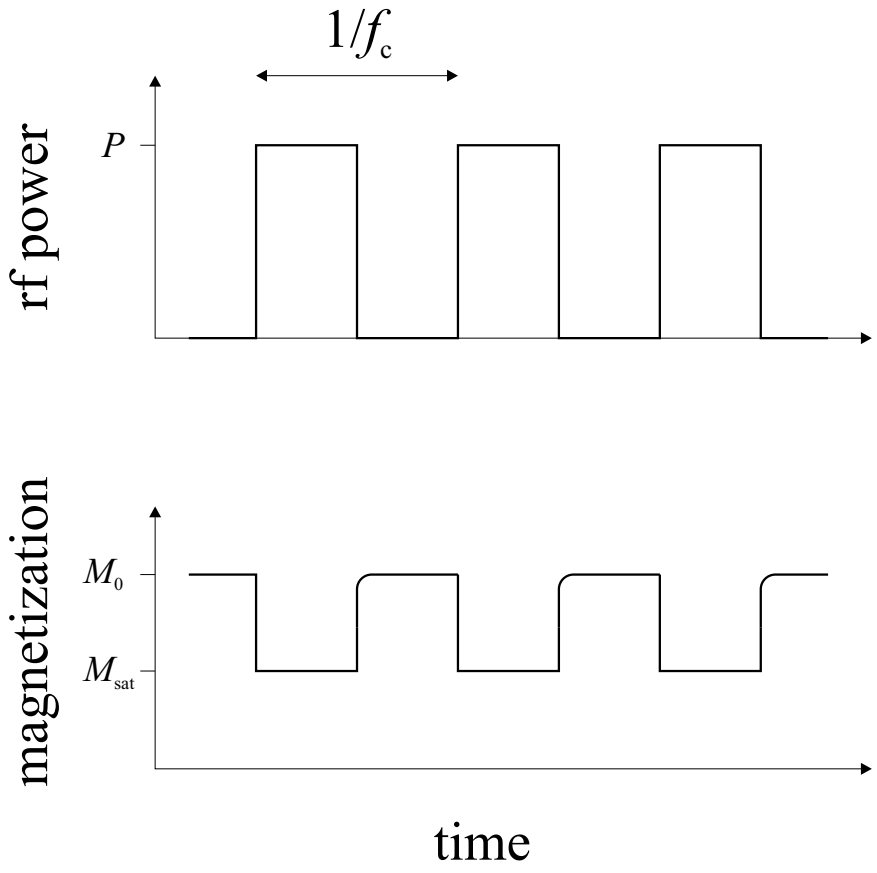

Figure 3.9: Cyclic saturation modulation scheme. (a) The rf field is turned on and off at a the cantilever resonance frequency. (b) When the rf is on, the magnetization becomes saturated, and is reduced to M_{sat}. When the rf is turned off, the thermal magnetization M_0 is recovered in a time T_1, a process indicated by the curved edges of the recovering magnetization. The time this takes is greatly exaggerated in the figure.

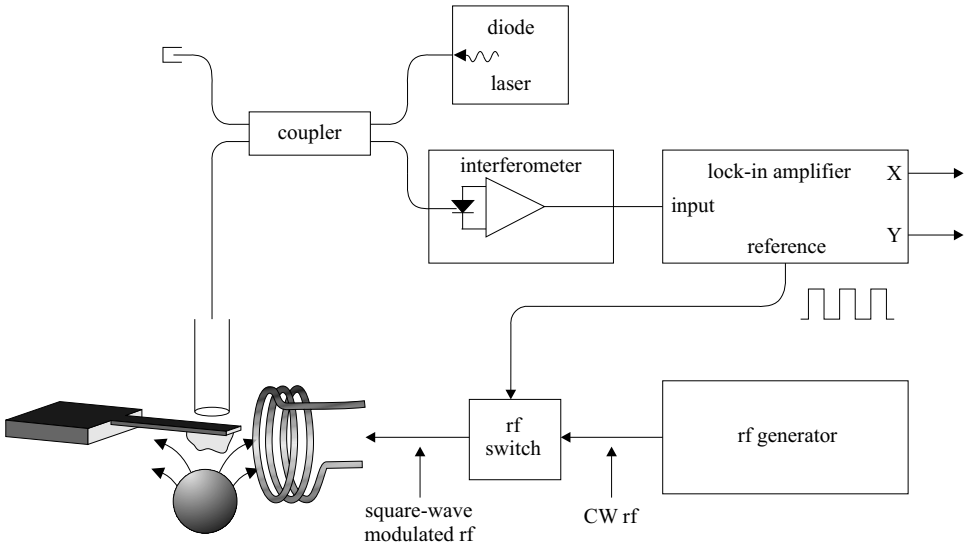

Figure 3.10: Block diagram of ESR experiment.

3.3.1 Results

Figure 3.11 shows the lock-in output as a function of external magnetic field. The interferometer output voltage is converted to a displacement using equation 3.2. Indeed the signal is mostly present in the quadrature phase (circles) of the cantilever response. The in-phase response (line) shows a slight resonant response, due to the imperfect match between the lock-in reference frequency and f_c, leading to a cantilever response not exactly $\pi/2$ out of phase with the drive. This is unavoidable due to the finite precision of the lock-in internal reference frequency.

Notice that both channels show a (negative) background response away from resonance. This is probably due to periodic heating of the cantilever or its support structure, and is a major drawback of the cyclic saturation technique. The fact that the response is so similar in the two channels has no significance—the phase of the background signal was unpredictable, and different on different days. This background could be avoided by modulating at half the cantilever frequency [24]

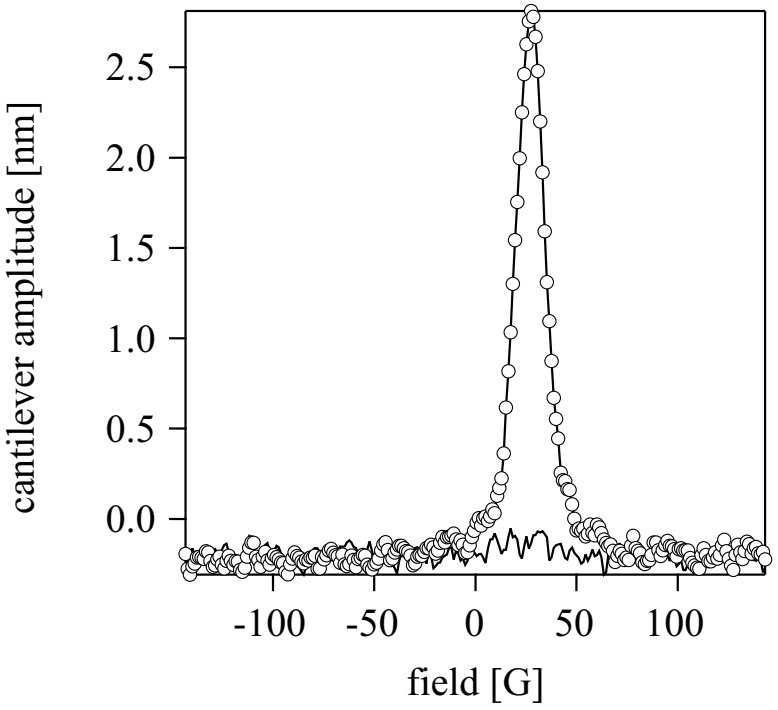

Figure 3.11: The in-phase (line) and quadrature (circles) response of the cantilever as a function of external magnetic field strength for sample-on-cantilever ESR of DPPH. The signal is mostly present in the quadrature phase.

or employing anharmonic modulation [29], as described in section 1.2.1. However, for the purposes of these experiments this was not deemed necessary.

Figure 3.12 shows another ESR experiment with similar experimental parameters. Here the distance between the magnetic particle and the sample was increased compared to the previously discussed experiment, so the resonant field had to be mostly provided by the electromagnet (notice that the positive-field peak shows up at a much higher applied field than in Figure 3.11). The field provided by the magnetic particle was low enough that it could be overcome in the negative field direction, and a second peak appeared. Notice also how much smaller the signal is than in Figure 3.11, because with the magnetic particle farther away the field gradient at the sample is much smaller. Whether a given peak points up or down depends on whether the interferometer is tuned to a positive or negative slope (see section 3.2.1). But the two peaks must have opposite sign—one is an interrupted upward force, the other an interrupted downward force, because the applied field will determine the direction of the sample magnetization, but is not large enough to change the direction of the tip magnetization—and therefore opposite phase with respect to the lock-in reference.

Measuring both peaks allows the tip and applied fields to be disentangled. Let B_{pos} be the applied field at which the positive-field peak appears, and B_{neg} be that of the negative-field peak. Then

$$B_{\mathrm{pos}} = B_0 - B_{\mathrm{tip}}, \tag{3.5}$$

and

$$B_{\mathrm{neg}} = -(B_0 + B_{\mathrm{tip}}). \tag{3.6}$$

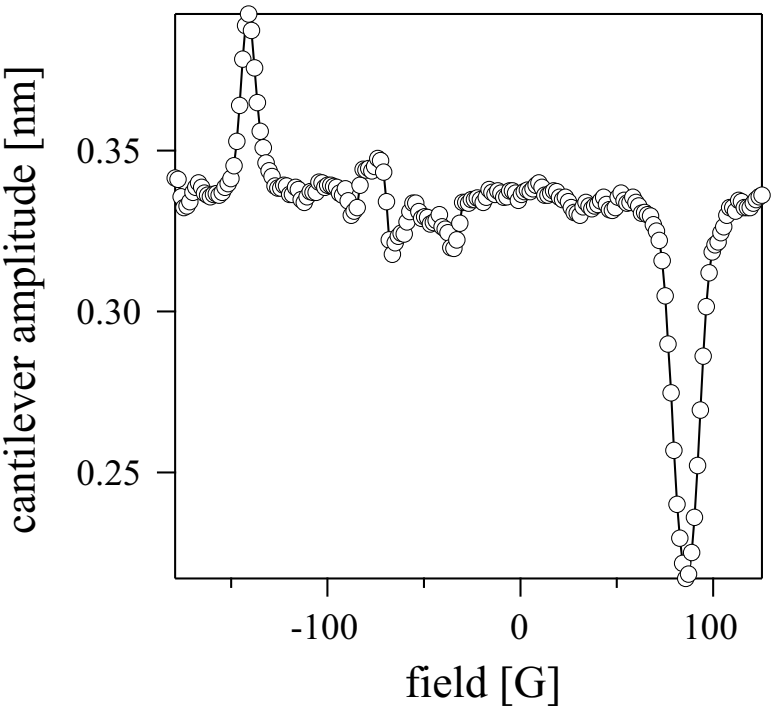

Figure 3.12: ESR experiment showing resonance peaks at positive and negative field.

Subtracting these equations and rearranging gives

$$B_0 = \frac{B_{\rm pos} - B_{\rm neg}}{2}. \tag{3.7}$$

For the data in Figure 3.12, $B_{\rm pos} = 90$ G and $B_{\rm neg} = -140$ G, giving $B_0 = 115$ G. Dividing the rf frequency $\omega_0/2\pi = 350$ MHz by this quantity gives a measured gyromagnetic ratio of $\gamma_{\rm m} \cong 3.0 \times 10^{10}$ Hz/T, which compares fairly well with the electron gyromagnetic ratio $\gamma_e = 2.80 \times 10^{10}$ Hz/T [21]. The largest source of error is the estimation of the coil constant—indeed, if the coil constant were an important parameter in these experiments, this measurement could be used to calibrate it to higher accuracy.

3.3.2 Power broadening

As discussed in section 2.2.5, the saturation signal should get larger and wider in frequency as the input power is increased. Power broadening can be used as a method of measuring B_1, which is an important figure of merit for one's rf circuitry, and especially important here because of the unconventional pairing of a half-wave line with such a small inductance. Here experiments are described in which the strength of B_1 is extracted from a power broadening measurement.

In DPPH, $T_1 \approx T_2$, [35] so equation 2.36 is appropriate. Recasting 2.36 in field units by dividing by $\gamma_e^2 T_1^2$ gives

$$M_z(B) = M_0 \frac{1/\gamma_e^2 T_1^2 + (B - B_0)^2}{1/\gamma_e^2 T_1^2 + B_1^2 + (B - B_0)^2}. \tag{3.8}$$

In DPPH at 77K, $1/\gamma_e^2 T_1^2 \approx (1.3\,\mathrm{G})^2$ [99]. Figure 3.13 shows a number of curves collected at various rf powers, along with fits of the data to equation 3.8 with $1/\gamma_e^2 T_1^2 = (1.3\,\mathrm{G})^2$. As expected, as the input power is increased the curve becomes

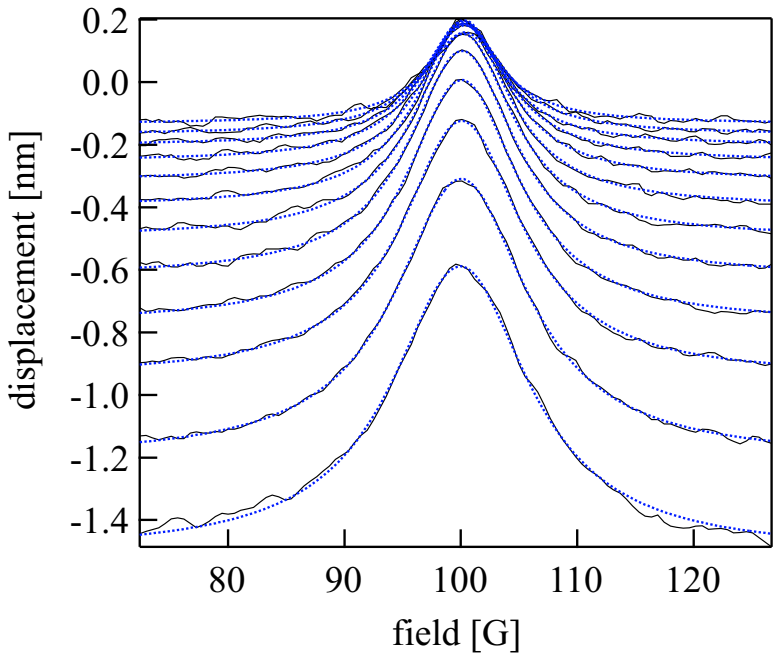

Figure 3.13: ESR resonance spectra at various rf powers (solid lines) with fits to equation 3.8. From the top, the powers are 126 mW, 158 mW, 200 mW, 251 mW, 316 mW, 398 mW, 501 mW, 631 mW, 794 mW, 1000 mW, 1259 mW and 1585 mW.

"deeper" and wider. Also, the background driving of the cantilever increases with the input power.

But is the value of B_1 given by fitting equation 3.8 to these data accurate? The above analysis fails to take into account the fact that signal is collected from electrons throughout the sensitive slice, which experience a range of fields, and that the sample has finite thickness. The simplest way to account for this is to add a constant to the denominator of equation 3.8—this will have the effect of broadening the steady-state magnetization curve by an amount which does not depend on the input power. Because B_1 is proportional to the current in the coil, and the power P dissipated in the coil is proportional to the current squared, one

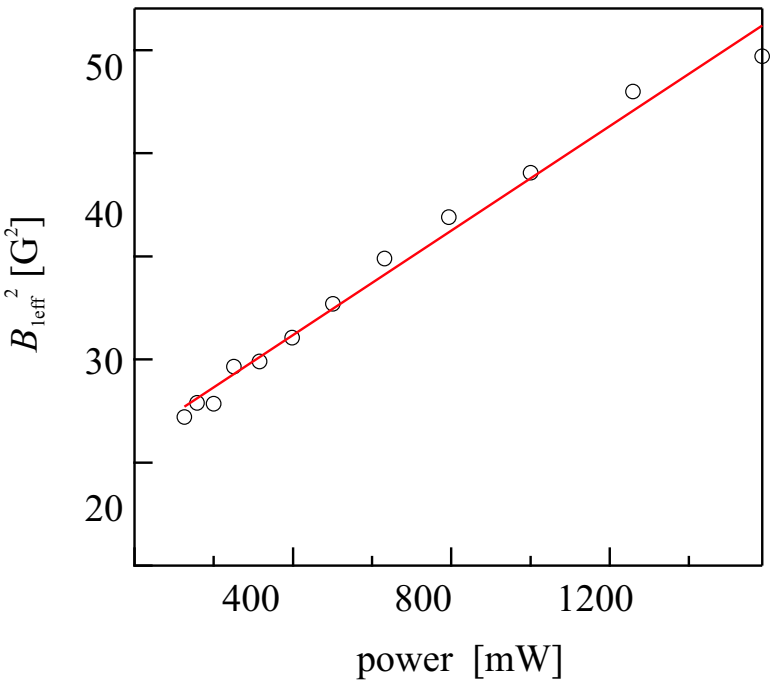

Figure 3.14: Power dependence of width of ESR resonance curves.

expects that $B_1^2 \propto P$. So in this simple model of the tip-broadened saturation spectrum, define the effective transverse field as

$$B_{1\text{eff}}(P) \equiv B_1^2(P) + \beta = \alpha P + \beta. \tag{3.9}$$

Figure 3.14 shows the values of $B_{1\text{eff}}^2$ obtained from the fits in Figure 3.13, plotted as a function of rf input power. A line fit to the data indicates that the coil is producing 5 G/$\sqrt{\text{W}}$ in the rotating frame. This result is somewhat disappointing—a transverse field of greater than 20 G is required for most pulsed solid-state NMR experiments, which would require 16 W rf pulses. This would likely place an unacceptable heat load 4 K MRFM experiments. Had the circuit performed as estimated in section 3.2.3 it would only have required 1 W.

A likely cause is the presence of the half-wave line, which places a resistance in series with the coil. Also, there could be stray capacitances and inductances in

the relatively large circuit elements at the tuning-capacitor end of the tank circuit which are not accounted for in a lumped-element analysis. These could alter the coupling to the half-wave line, making the current at the coil unpredictable. It should be said that the model used here in the power broadening measurement is somewhat crude—however this measurement was confirmed by a much more reliable method, described in Chapter 4.

3.4 Conclusions

In summary, a sample-on-cantilever MRFM apparatus was described which centered on a half-wave-line-based rf tank circuit. The probe is designed for variable-temperature, sample-on-cantilever MRFM experiments and for testing in a transfer dewar. Cantilever motion is detected with a fiber-optic interferometer, and a transverse rf field is provided by a half-wave-line-based tank circuit with a ~ 0.8 mm diameter coil. MRFM experiments were performed detecting ESR in DPPH in the sample-on-cantilever configuration. A gyromagnetic ratio measurement provided strong evidence that electrons were responsible for the observed signal. Power broadening experiments were performed, indicating a B_1 field of 5 G/$\sqrt{\text{W}}$ in the rotating frame, far short of the estimated value of 27.5 G/$\sqrt{\text{W}}$. This unexpectedly low figure is confirmed by nuclear nutation measurements in Chapter 4, and is attributable to the added resistance of the half-wave line or possibly unknown phase shifts in the tank circuit.

CHAPTER 4

FORCE-DETECTION OF NUCLEAR MAGNETIC RESONANCE IN AMMONIUM NITRATE

4.1 Introduction

This chapter describes room-temperature MRFM experiments in which ^{1}H NMR is detected in ammonium nitrate. Experiments are performed in high vacuum with a commercial, contact-mode AFM cantilever, just as in Chapter 3, which gives a force sensitivity of 5 fN/$\sqrt{\text{Hz}}$. This sensitivity is relatively low by modern MRFM standards, but that does not reduce the significance of these measurements—the manipulation of nuclear spins provides vital information on the quality of the B_1 field.

The experiments described in this chapter use the cyclic ARP modulation technique, in which the spins must stay locked to the rf field during the entire signal collection period. Because MRFM uses much longer spin-lock times than in conventional NMR (often > 1 s), this makes exceptional demands on the quality of the rf. Yannoni has performed experiments spin-locking nuclei with long $T_{1\rho}$ values using a variety of rf sources, and found that the lock times depend strongly on the phase noise of the source [100]. Shorter lock times mean a larger measurement bandwidth, and therefore reduced SNR. For this reason it is extremely important to have low-phase-noise rf in nuclear MRFM experiments, and to test whether digitally synthesized rf waveforms—desirable for the complicated pulse sequences necessary for the Fourier-encoded imaging protocol of Kempf and Marohn [18], or for advanced ARP modulation schemes [20]—could achieve this high standard.

In section 4.2 the rf generation apparatus used to create the signals for ARP-

based MRFM is described. Section 4.3 presents the results of initial ^{1}H NMR MRFM experiments in ammonium nitrate. In section 4.4 experiments will be described in which fully digitally-synthesized, pulsed MRFM is demonstrated, providing a pulsed-NMR measurement of B_1.

4.2 Experiment

Experiments were performed in the sample-on-cantilever configuration[1]. The sample was ammonium nitrate, chosen for its relaxation properties, i.e. $T_1 \approx T_{1\rho} \approx 1$ s at room temperature [26]. For this reason it makes a very attractive MRFM sample for room-temperature experiments. However, care must be taken that too much time is not left between evacuating the probe and performing measurements—ammonium nitrate sublimes in vacuum! A flake of ammonium nitrate, approximately 100 µm × 50 µm × 10 µm, was glued to the end of a cantilever with 5-minute epoxy, as in the previous chapter.

The external polarizing field $B_0 \approx 8$ T was provided by a liquid-He cooled superconducting magnet. The dewar was equipped with a vacuum-insulated insert[2] which provided a space of 3" diameter in the magnet center and isolated from the liquid He, and which admitted He gas from a heated nozzle through a capillary from the liquid He reservoir. During experiments He gas heated to approximately 300-325 K was flowing through this sample space. At these gas temperatures the probe was found to equilibrate at a temperature of ~ 290 K.

The sample magnetization was modulated at the cantilever mechanical resonance frequency by the cyclic ARP technique [26], in which repeated ARP sweeps

[1]The apparatus used here may be assumed to be the same as that described in detail in chapter 3 except where differences are mentioned.

[2]Custom Janis SuperVariTemp system.

(see section 2.2.7) adiabatically tip the magnetization from up to down and back again. A Schematic of the modulation scheme is shown in figure 4.1. A triangular frequency modulation was employed. (Sinusoidal [26] and tangential [20] modulation have been demonstrated by other researchers.) The adiabatic condition (equation 2.38) puts a limit on the modulation width Ω because a full sweep must be completed during half a cantilever cycle. Recasting equation 2.38 in these terms gives

$$\Omega \ll \frac{\gamma^2 B_1^2}{4 f_0}, \tag{4.1}$$

where f_0 is the cantilever frequency.

The rf was generated in one of two ways, to be referred to here as "analog" and "digital". In the analog method, shown in Figure 4.2(a), a computer and a digital-to-analog converter (DAC) were used to produce synchronized control voltages. A voltage proportional to the desired modulation waveform, consisting of an initial large sweep, then many triangular cycles at the cantilever frequency, a few kHz, and finally another large sweep away from resonance, as in Figure 4.1(a), was sent to the FM input of the rf generator. The rf generator's center frequency was set to the tank circuit resonance, ~ 350 MHz. A TTL pulse train at the cantilever frequency was sent to the lock-in amplifier's (Stanford SR830) reference input. This signal was synchronized with the lock-in reference signal so that phase-coherent lock-in detection could be used. The TTL signal began before the FM voltage by an amount of time sufficient for the lock-in to lock to the signal, ~ 75 ms. A TTL pulse was used to turn on and off the rf amplifier, as in 4.1(b)[3]. In this method the DAC need only create signals in the audio frequency range.

[3]This pulse was actually supplied by one of the DC voltage outputs of the lock-in amplifier, but is drawn as the same DAC in 4.2(a) for simplicity.

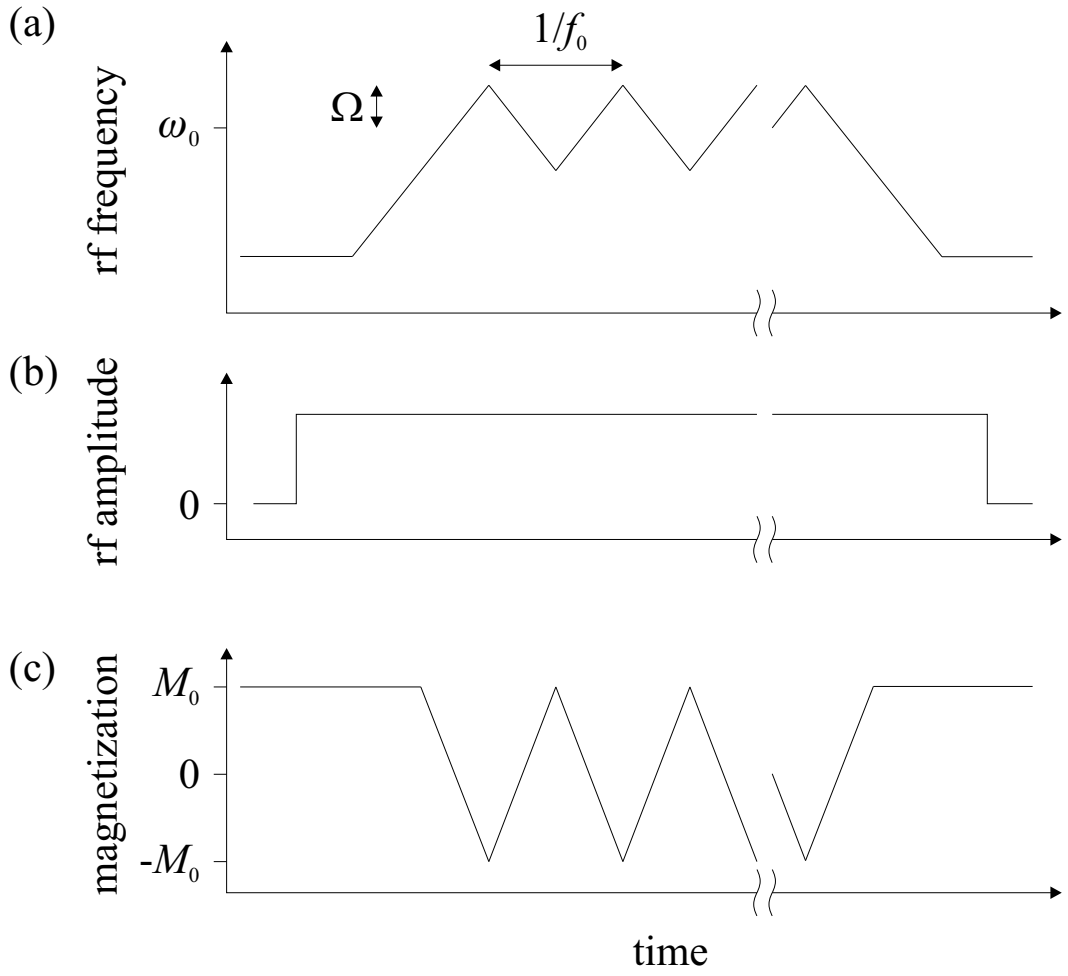

Figure 4.1: A plot of the (a) rf frequency, (b) rf amplitude, and (c) sample magnetization in the cyclic ARP modulation scheme. Initially the rf frequency is far from resonance, and at this time, when the spins are least affected by its presence, the amplifier is turned on. The rf is then swept through the spins' resonance frequency ω_0 repeatedly, with a modulation amplitude Ω, and at a frequency which coincides with the cantilever mechanical resonance frequency. The magnetization remains locked to the effective field, and is repeatedly inverted in synchrony with the rf frequency modulation. The rf frequency is brought far off resonance again before the rf amplifier is turned off.

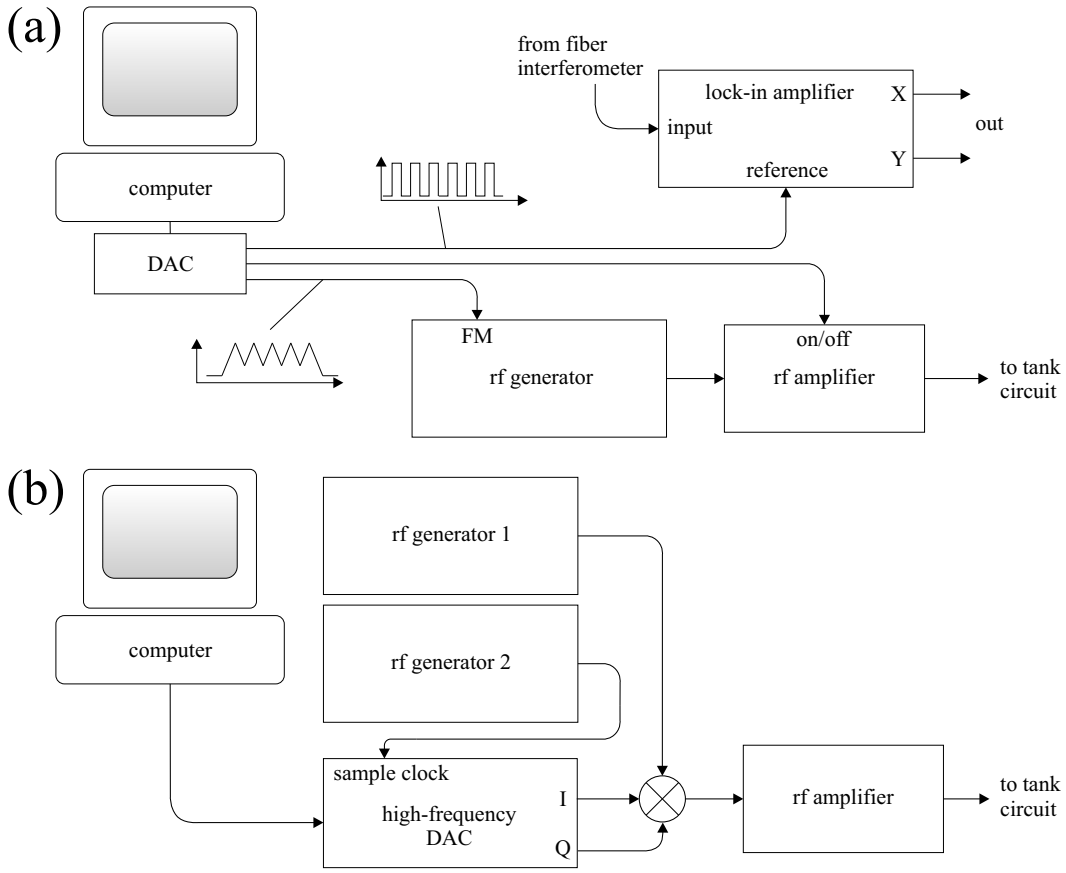

Figure 4.2: Block diagram of the frequency modulated rf generation apparatus.

Also, since the rf is generated directly by a high-quality rf source the phase noise of the resulting signal is known. Sources used were the HP (now Agilent) 8657A, nominal single-side-band phase noise -120 dBc/Hz at 20 kHz off of carrier, and the HP 8642A, with nominal single-side-band phase noise -137 dBc/Hz at 20 kHz off of carrier. These values were previously shown by Yannoni to be sufficient for > 1 s spin-lock times [100].

In the "digital" method, Figure 4.2(b), in-phase and quadrature rf signals, with frequency profile as in 4.1(a), were synthesized using a high-frequency DAC at ~ 4 MHz (the *intermediate frequency*, or IF), then shifted up to the tank circuit

resonance frequency, $\sim$ 350 MHz, using single-sideband mixing [95]. Because the phase noise of the internal clock in the DAC was not specified by the manufacturer[4], an external sampling clock is supplied by one of the HP sources named in the previous paragraph at $\sim$ 100 MHz. The use of an external sampling clock means that the entire internal timing circuitry of the DAC, which would normally create the signal at the specified sampling frequency, is bypassed. Instead samples are released at the zero crossings of the external signal.

In the "digital" method the rf amplifier was left on at all times. The DAC, in its resting state, i.e. when not producing rf, produced DC signals on both channels, which led to some degree of carrier bleed-through at the mixer. This was not problematic as the carrier was displaced from the Larmor frequency by the IF, $\sim$ 4 MHz, and so did not perturb the sample spins. The effect of this unwanted rf was further reduced by crossed diodes at the amplifier output. Also, because the high-frequency DAC had only two outputs, no reference signal for the lock-in could be provided with this hardware. Thus the lock-in amplifier could not be used in a phase-coherent manner, and only provided amplitude information.

The cantilever resonance frequency and quality factor were determined by Fourier transforming either the thermal noise signal (as in Figure 2.7), or a decaying excitation produced by striking the probe manually.

4.3 Results I: ^{1}H NMR

Figure 4.3 shows the output of the lock-in amplifier at two different external field strengths. Here the "analog" rf generation scheme as in Figure 4.2(a) was

[4]And therefore almost certainly too high for our purposes, considering the expense and care required to achieve low values.

used, at 28 dBm (= 631 mW), with an ARP center frequency equal to the center of the tank circuit resonance at 352.3 MHz and an ARP width of $\Omega = 100$ kHz. The cantilever had resonance frequency $f_0 = 1180$ Hz, quality factor $Q = 897$, and the probe temperature was measured to be ~ 300 K. These parameters, along with the manufacturer-quoted spring constant of 10^{-2} N/m give a minimum detectable force of $F_{\min} = 5$ fN/$\sqrt{\text{Hz}}$. The rf excitation began at time 1.8 s and lasted until time 3.8 s. At 8.240 T, shown as a dashed line, there is no discernible excitation associated with the rf excitation. The equipartition theorem prediction (equation 2.56) for the rms thermal cantilever noise is ~ 6.4 Å, which compares well to the observed background noise. At 8.254 T, shown as triangles connected by a solid line, a cantilever excitation is observed. The fact that it is coherent with the frequency modulation signal, yet field dependent, already provides strong evidence that the signal is due to NMR.

After the rf is turned on, the oscillation strength increases according to the characteristic time of the cantilever. This same effect is observed in the decay of the excitation after the rf is turned off. The decay in between is consistent with a magnetization decay. Here the decay time of the signal is on the order of 1 s, and so the origin of this decay is presumed to be primarily due to rotating-frame spin-lattice ($T_{1\rho}$) relaxation.

Figure 4.4 shows a curve formed by taking the lock-in output at time $t = 2.5$ s, where the maximum cantilever excitation occurs, from a number of data sets like the one in Figure 4.3. This gives a result more like a traditional magnetic resonance spectrum. The peak signal of 53 fN occurs at 8.254 T. The peak is considerably wider than a conventional NMR resonance peak, due to the field inhomogeneity due to the tip, the width of the ARP modulation, and the thickness of the sample.

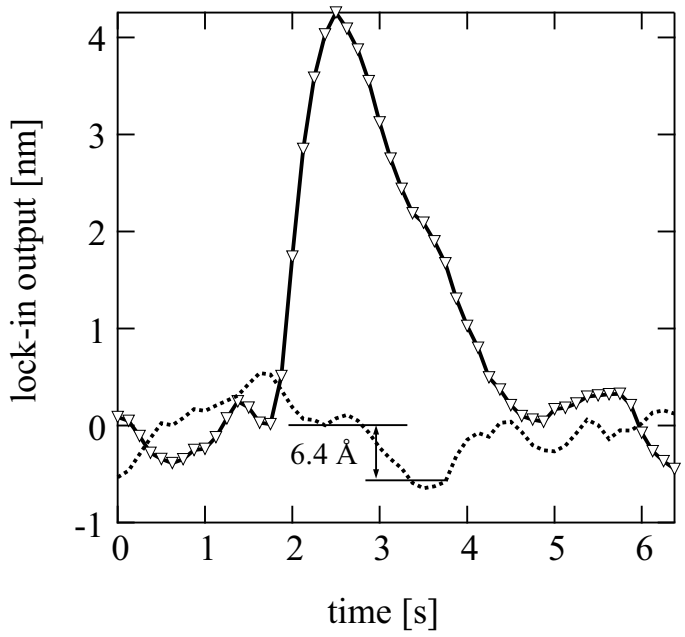

Figure 4.3: Lock-in output during cyclic ARP of ammonium nitrate sample, at two external field values. The cyclic ARP excitation begins at time 1.8 s and lasts until time 3.8 s. At 8.240 T (dashed line), a non-resonant field, there is no discernible excitation associated with the rf excitation. The equipartition theorem prediction for the thermal noise is $\sim$ 6.4 Å. At 8.254 T (triangles and solid line), a cantilever excitation is observed, coherent with the frequency modulation signal.

The SNR is about 10, in agreement with the predicted minimum detectable force of 5 fN.

In fact, the spectrum in Figure 4.4 can be viewed as a one-dimensional image of the sample—as the external field is changed, the sensitive slice moves through the sample, giving a signal proportional to the total magnetization in the slice at each field. The sample was observed with an optical microscope to be flat on the side glued to the cantilever, and somewhat convex on the other, as in figure 1.1. Because of the arrangement of the tip, field and sample, which are just as in figure 1.1, the flat side of the sample is farthest from the tip, and therefore comes into resonance at the highest external field. This is reflected in Figure 4.4—the high-field side of the peak is much steeper than the low-field side. Using an estimate for the field gradient based on a spherical particle 0.5 mm in diameter, a 1 T saturation field for the AlNiCo, and a tip-sample distance of 0.2 mm gives a field gradient of about 800 T/m. With the peak-to-peak ARP width of 200 kHz used here, the sensitive slice was approximately 6 μm thick.

In order to further confirm that the signal was due to NMR, the tank circuit was tuned 300 kHz lower in frequency, to 352.0 MHz, and a curve similar to the one in Figure 4.4 was taken. The result is shown in Figure 4.5. The dashed curve is the same data as in Figure 4.4. The solid curve shows the response at the new ARP center frequency of 352.0 MHz. The response has shifted down field, as expected. To the resolution of the measurement, the shift is from 8.254 T to 8.247 T, a shift of 70 G. Dividing by the shift in field, 300 kHz, gives an estimated gyromagnetic ratio of $\gamma \cong 43$ MHz/T, consistent with the proton gyromagnetic ratio of $\gamma_p = 42.6$ MHz/T [21]. This gives a strong indication that the signal is due to ^{1}H NMR.

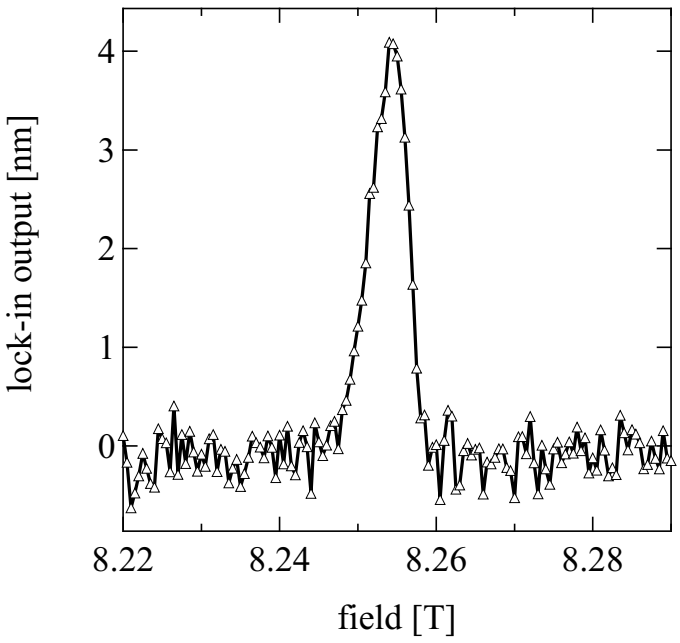

Figure 4.4: Force-detected NMR spectrum from ammonium nitrate, obtained by plotting the lock-in output at $t = 2.5$ s from a number of data sets like that in Figure 4.3.

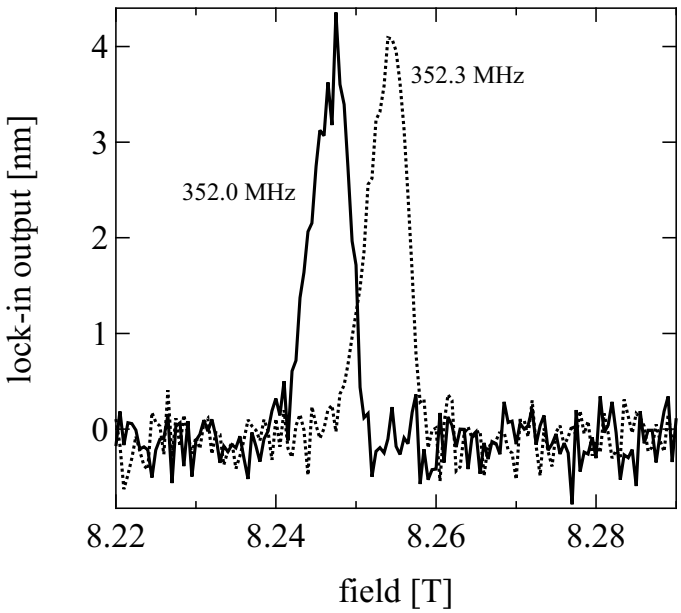

Figure 4.5: Two spectra collected with different ARP center frequencies. The peak shifts by about 70 G for a frequency shift of 300 kHz, consistent with the proton gyromagnetic ratio.

4.4 Results II: pulsed NMR

In this section MRFM nutation experiments are described. As discussed in section 2.2.6, when an on-resonance transverse (B_1) field is applied to a thermally polarized spin ensemble, the magnetization will precess around the effective field in the rotating frame, a process called nutation. Nutation can be used as a sensitive measure of B_1 strength, because the nutation frequency, also called the Rabi frequency, is given by $\omega_{\mathrm{R}} = \gamma B_1$. Nutation was first demonstrated with MRFM in fluorine nuclei in CaF_2 [44], and later in electrons [37].

Nutation experiments were performed in the following manner. First the field value of maximal signal was located using the methods described in the previous section. The field was set to this value, and the rf generation apparatus was set up

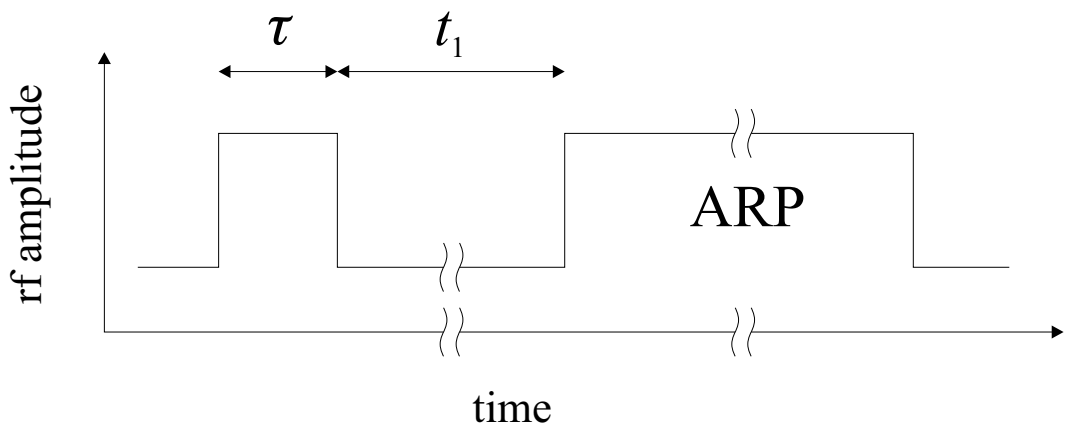

Figure 4.6: The rf sequence used in nutation measurements. A pulse of duration τ is applied to tip the magnetization away from vertical, after which the rf is left off for a time t_1 in which the in-plane component of the magnetization decays away. The resulting magnetization projection on z is then read out with an ARP sequence.

as in Figure 4.2(b). Then an rf sequence as shown in Figure 4.6 was applied. First a pulse of duration τ was applied at the ARP center frequency. Then the rf was turned off for a duration t_1. The time t_1 should be $> T_2$ so that any transverse magnetization decays away. The resulting magnetization M_p lies along the z axis, with length equal to the projection of M_0 along z after the tipping pulse. Then an ARP sequence exactly as in the previous section, but generated in the method of Figure 4.2(b), was applied to measure M_p. The cantilever excitation was not measured coherently, so the two components of the lock-in signal were Fourier transformed and integrated, to obtain a signal proportional to the mean squared cantilever amplitude (through Parseval's theorem) and therefore proportional to M_p^2. After waiting a time $\gg T_1$, so that the magnetization fully recovered its thermal polarization, the sequence was repeated with a different pulse duration τ.

The expected behavior of the magnetization projection onto z, M_p, as a func-

tion of pulse time τ is shown in Figure 4.7(a). At zero pulse time the magnetization will be equal to the thermal equilibrium value M_0. As the magnetization precesses, its projection onto z will have a cosinusoidal behavior, with an exponentially decreasing envelope with some decay time τ_m. The squared cantilever amplitude after a pulse of duration τ should be proportional to M_{p}^2, so will trace out a decaying squared cosinusoid as τ is stepped, as in Figure 4.7(b).

Figure 4.8 shows the results of the measurement (circles), along with a fit to a decaying squared consinusoid, plus a constant to account for background cantilever excitation (blue line). The data show the expected behavior, and the fit provides a Rabi frequency of $\omega_{\mathrm{R}} = 1.25 \times 10^5$ rad/s, which gives $B_1 = \omega_{\mathrm{R}}/\gamma_{\mathrm{p}} = 4.6$ G, in agreement with the measurement of $B_1 = 5$ G from power broadening in chapter 3.

The fit indicates a decay time of 0.125 µs. This decay is likely due partially to spin-spin relaxation (T_2 processes), which sets the decay time in inductively detected nutation experiments. Here, though, dephasing due to the inhomogeneous field from the tip probably also plays a significant role. Spins for which the pulse is nonresonant precess around an effective field which is not perpendicular to z, resulting in increased dephasing of the spins in different parts of the slice.

4.5 Conclusions

In this chapter experiments were described in which MRFM was used to detect ^{1}H NMR in ammonium nitrate. Force measurements were performed with a commercially produced AFM cantilever at room temperature in high vacuum, and were thermally limited with a minimum detectable force of $F_{\mathrm{min}} = 5$ fN/$\sqrt{\mathrm{Hz}}$. A peak force of 53 fN was detected from a flake of ammonium nitrate with dimensions

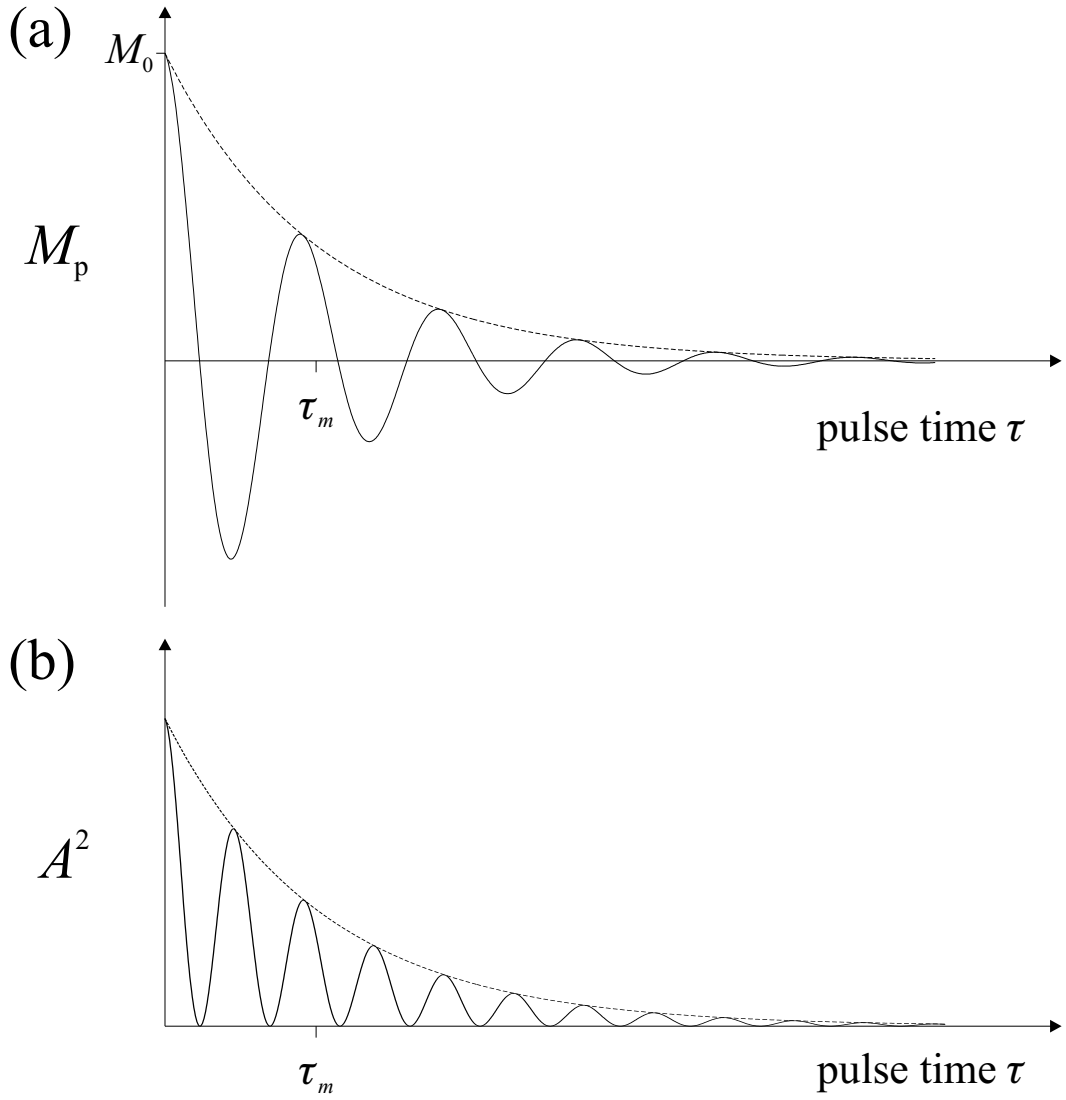

Figure 4.7: Expected behavior under nutation. (a) The z projection of the magnetization as a function of pulse time τ. The magnetization is initially at its thermal equilibrium value M_0, and makes a cosinusoidal projection on z as it precesses. (b) The squared cantilever excitation as a function of pulse time τ will therefore take the form of a squared cosinusoid.

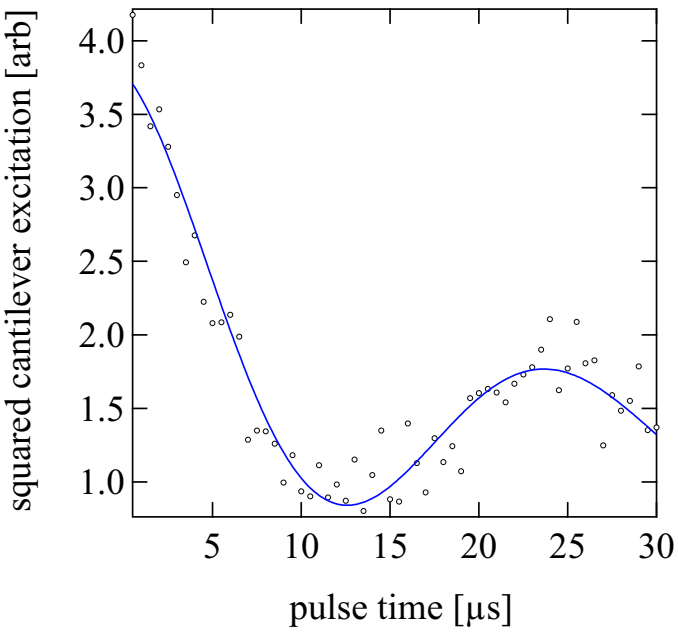

Figure 4.8: Observed nutation signal (circles) fit to a decaying squared cosinusoid (blue line.)

on the tens-of-microns scale. Observation of a shift in peak location upon changing the rf modulation center frequency was consistent with the proton gyromagnetic ratio, which strongly indicates that the signal was due to ^{1}H NMR. Pulsed NMR MRFM was demonstrated with a digital rf generation scheme. The Rabi frequency for was measured to be $\omega_{\mathrm{R}} = 1.25 \times 10^5$ rad/s, which gives $B_1 = \omega_{\mathrm{R}}/\gamma_{\mathrm{p}} = 4.6$ G at 1 W of rf power, in agreement with the power-broadening estimate of B_1 given in Chapter 3.

These measurements, by showing that nuclear spins could be spin-locked for times on the order of 1 s, demonstrate that the rf generation schemes described here have sufficiently low phase noise for use in nuclear MRFM experiments. The fact that this is true even for digitally synthesized rf is significant because it allows more general rf pulse and modulation schemes to be implemented. This is particularly important for the complicated pulse sequences which must be synchronized

with cantilever motions in order to achieve FT-MRFM imaging [18], or for more advanced frequency modulation schemes such as phase-cycled, tangent-modulated ARP [20]. However, these experiments also confirm the diagnosis of anemic B_1 made in Chapter 3. This and other considerations caused the half-wave line tank circuit to be abandoned for the high-sensitivity, 4 K experiments described in Chapter 5.

CHAPTER 5

FORCE-GRADIENT DETECTION OF NUCLEAR MAGNETIC RESONANCE IN GALLIUM ARSENIDE

5.1 Introduction

In this chapter a unique type of MRFM is described, in which a force gradient, rather than a force, perturbs a cantilever's motion. A force gradient has units of N/m, the same as a spring constant. This suggestive fact leads to a method—the force gradient acts as an additional (positive or negative) restoring force on the cantilever, registered as a shift in the cantilever's resonance frequency. This property is widely used in AFM experiments [101], but before the experiments described here had never been applied to MRFM. (This should not be confused with the OSCAR method, which produces a cantilever frequency shift, but relies on forces, not force gradients, to do so. This distinction will be made more clear in section 5.2.2.)

In 2002, when the technique was conceived, MRFM was facing two problems. The first, as discussed in section 1.2.2, is that ultrasoft cantilevers must be used perpendicular to the sample surface, but at this time the sensitivity to detect statistical polarization in nuclear MRFM had not yet been reached. As will be seen in section 5.2, force-gradient MRFM does not require statistical imbalances in the spin polarization. Second, all previous nuclear MRFM experiments (and those at the highest sensitivities achieved with electrons) had required that the sample magnetization remain spin-locked [85] to an applied radio-frequency field during the entire signal acquisition period, with the result that signal could only be collected for a time $t \sim T_{1\rho}$, the spin lattice relaxation time in the rotating frame.

This was the situation, for example, in the experiments described in Chapter 4. With force-gradient MRFM, signal can be collected for a time approaching T_1, the spin-lattice relaxation time in the laboratory frame. Since often $T_1 \gg T_{1\rho}$ at cryogenic temperatures, a much wider range of samples should be accessible to MRFM using the approach introduced here. Also, for samples with $T_1 \geq 10$ ms, the method opens up the exciting possibility of following magnetization recovery in real time in a single-shot experiment. For this reason the technique will be referred to as CERMIT, or *cantilever enabled readout of magnetic inversion transients*.

In section 5.2, the CERMIT method will be described in detail and compared to the other perpendicular MRFM method, OSCAR. An estimate of the signal size is made for both techniques, and these are put into perspective by comparing to that given for parallel-cantilever force detection in Chapter 1. In section 5.3 the apparatus built to demonstrate the technique is described. Results from MRFM magnet-on-cantilever experiments, using an ultrasoft cantilever, at 4.4 K and 7 T, are given in section 5.5. Finally, numerical calculations are presented and compared with observation in section 5.6.

Due to the use of a low-spring-constant cantilever at a relatively low temperature, the measurements described in this chapter achieved world-record nuclear MRFM sensitivity at the time of their publication [48], representing an improvement of more than 500 times the previous best [44] [1].

[1] A somewhat higher sensitivity for nuclei was recently reported at the time of this writing [102]. Also, the recent detection of a single electron by MRFM had a magnetic moment sensitivity about 50 times higher [40].

5.2 Theoretical background

5.2.1 Force-gradient MRFM

As discussed in section 1.2.2, a uniformly magnetized planar sample will produce no force on a perpendicular cantilever. Figure 5.1(a) shows a perpendicular cantilever's tip near a planar sample. The external magnetic field here is assumed to be along z, and the cantilever is vibrating in the x direction. The force from spins on one side of the cantilever will be offset by other spins on the opposite side, and will sum to zero. This is the basic problem which inspired the invention of the CERMIT protocol.

Now consider the force gradient on the tip. Magnetic moments μ (assumed, for now, to all be pointing in the $+z$ direction) in the sample interact with the tip magnet to produce a net force gradient given by

$$\frac{\partial F_x}{\partial x} = \sum_j \mu(\mathbf{r}_j) \frac{\partial^2 B_z(\mathbf{r}_j)}{\partial x^2}, \tag{5.1}$$

where B_z is the z component of the field due to the tip, $\mathbf{r}_j$ is a vector pointing to the spin, x is the direction of cantilever deflection, and the sum is over all spins in the sample. This spin force gradient is also zero for a homogeneously magnetized planar sample [103]. In the CERMIT method, a detectable change in force gradient is produced by inverting spins in a region under the tip using ARP [Figure 5.1(b)]. Although this inverted region of spins, because of its symmetry, will produce no net force on the cantilever (in its bending direction), the force gradient it produces is measurable. The region of inverted spins lies between two constant-B_z contours determined by the initial and final frequencies of the ARP sweep.

After the sweep the resulting shift in the force gradient, and therefore in the spring constant, will be equal to the difference between the force gradient before

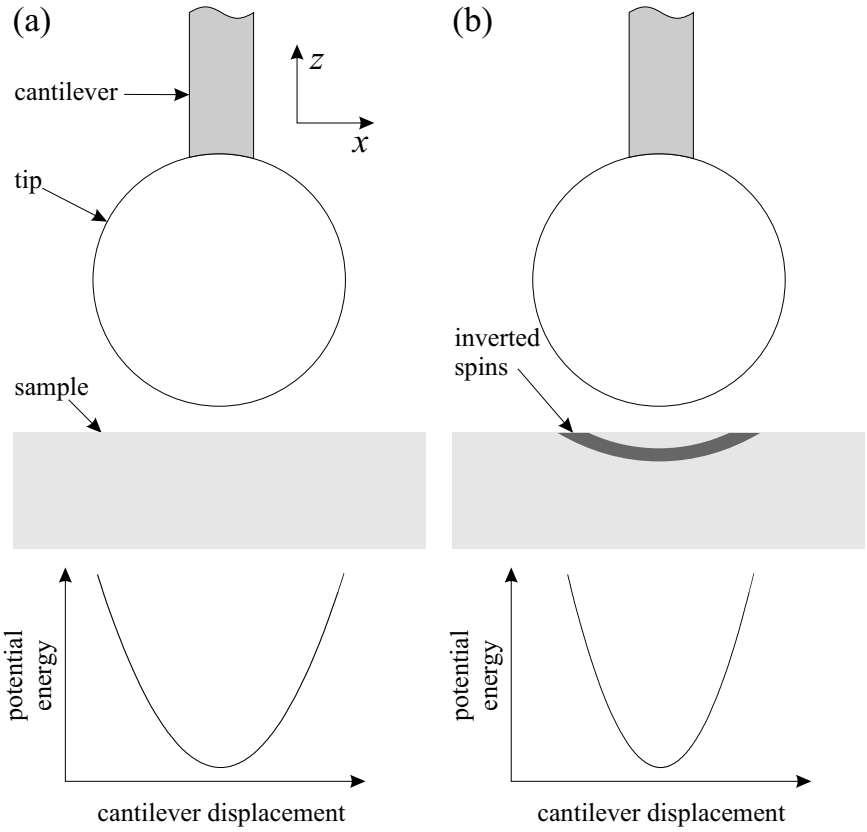

Figure 5.1: The CERMIT experiment. (a) A magnet-tipped cantilever is placed perpendicular to the sample surface. The forces from spins on the two sides of the tip cancel to zero by symmetry. The cantilever vibrates according to its harmonic potential energy function. (b) After an ARP sweep, there is a slice of inverted spins near the tip. The inverted spins attract the tip, so there is an energy cost associated with displacing the tip to either side. The result is that the potential energy function steepens, which raises the effective spring constant of the cantilever. This change is registered as a shift in the cantilever's resonance frequency.

and after the sweep:

$$\Delta k \equiv \left.\frac{\partial F_x}{\partial x}\right|_{\text{after}} - \left.\frac{\partial F_x}{\partial x}\right|_{\text{before}} = -2 \sum_{j \in \text{slice}} \mu(\mathbf{r}_j) \frac{\partial^2 B_z(\mathbf{r}_j)}{\partial x^2}, \tag{5.2}$$

where now the sum is over spins in the slice only. Spins inside the slice contribute with the same sign in both terms, leading to the factor of two in front of the sum, whereas spins outside the slice cancel in the difference.

This change in the spring constant shifts the cantilever's resonance frequency by an amount Δf. Since $f = (1/2\pi)(k/m)^{1/2}$, for small spring constant shifts this is given by

$$\Delta f \approx \frac{f_0}{2k} \Delta k \tag{5.3}$$

This is the quantity which is measured in the experiment.

At each end of the sweep, where the rf is turned on or off, the spins will not be able to adiabatically follow the effective field, and a "dead" region of decreased magnetization will be produced. The dead regions will be slices of thickness $\sim G\delta$, where G is the field gradient at the location of the slice and δ is the linewidth of the NMR resonance of the nucleus under study. These dead regions are expected to be of negligible width in the experiments described in this chapter. It should also be mentioned that because the tip is vibrated, the total field at the location of spins in the sample will be changing during the sweep Tip's motion must be kept sufficiently small that the adiabatic condition (equation 2.38) is met during the sweep.

5.2.2 Estimate of signal size and comparison with OSCAR

This section gives an estimate of the CERMIT signal size, and a comparison with that of the OSCAR technique employed by researchers at IBM in high-

sensitivity MRFM experiments [38–40]. These will be compared with the expected force from the parallel-cantilever experiment described in Chapter 1. In order to effectively compare these techniques, which all measure different quantities, the estimates will be cast it terms of SNR for a thermally-limited experiment. Single-spin detection will be considered in all cases—the different magnetization modulation schemes involved produce different volumes of active spins, and by considering a single spin this complication can be removed. The experimenter can always multiply by the number of spins for the expected sensitive slice to get a practical estimate (for a good estimate the fact that the gradients won't be the same over the whole slice should be taken into account).

The assumption will be made throughout of a spherical magnet of radius a and magnetization M, with magnetic moment lying along z (see Figure 5.2). In what follows, the objective is to calculate the interaction of such a magnet with a single spin magnetic moment, also polarized along z.

Standard force detection

The "parallel-geometry" experiment, with a spin directly below the tip was considered in section 1.1.1, with the force given by equation 1.5. The SNR for this experiment is found by simply dividing by the minimum detectable force (equation 2.63), which gives

$$\mathrm{SNR}_{\mathrm{Force}} \approx 0.633 \frac{\mu \mu_0 M}{a F_{\mathrm{min}}}. \tag{5.4}$$

This expression provides a convenient reference for the more modern experiments considered below.

CERMIT

For the CERMIT experiment a similar procedure is followed: consider a single spin directly below the tip and calculate the signal, then maximize with a fixed d. Here the signal is given by $\Delta k_x = \mu \partial^2 B_z / \partial z^2$ where the field gradient is evaluated at the location of the spin. This gives[2]

$$\Delta k_x = \frac{4\mu\mu_0 M}{a^2}\left(\frac{a}{a+d}\right)^5, \tag{5.5}$$

which for a fixed d has a maximum at $a = 3d/2$. Putting this into the above gives

$$\Delta k_x \approx 0.311 \frac{\mu\mu_0 M}{a^2}. \tag{5.6}$$

To achieve an expression similar to equation 5.4 the above should be divided by the *minimum detectable spring constant shift*, defined as the spring constant change which can be detected with a SNR of one. This is given, for a cantilever oscillating with amplitude x_{rms}, by [104, 105]

$$\Delta k_{\mathrm{min}} = \frac{F_{\mathrm{min}}}{x_{\mathrm{rms}}}, \tag{5.7}$$

which has units of $\mathrm{N}/(\mathrm{m}\sqrt{\mathrm{Hz}})$, as expected[3]. So the SNR for the single-spin CERMIT experiment is given by:

$$\mathrm{SNR}_{\mathrm{CERMIT}} = 0.311 \frac{\mu\mu_0 M x_{\mathrm{rms}}}{a^2 F_{\mathrm{min}}}. \tag{5.8}$$

[2]A minus sign has been omitted for simplicity.

[3]This expression can be understood as follows. A cantilever oscillating with a rms amplitude x_{rms} in the presence of a force gradient $\partial F/\partial x$ experiences a span of forces throughout its motion of approximately $(\partial F/\partial x) x_{\mathrm{rms}}$. For the cantilever to "notice" this difference, this quantity needs to be $\geq F_{\mathrm{min}}$. Therefore $\Delta k_{\mathrm{min}} \equiv (\partial F/\partial x)_{\mathrm{min}} = F_{\mathrm{min}}/x_{\mathrm{rms}}$.

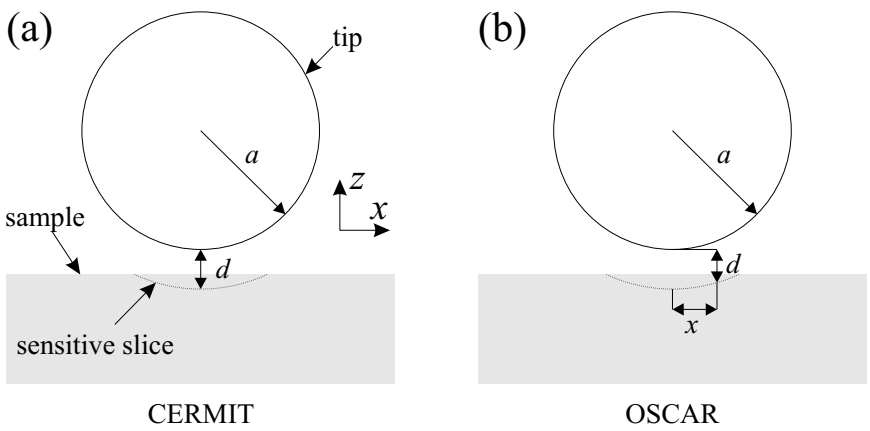

Figure 5.2: The distances used in the text to describe the CERMIT and OSCAR experiments. (a) In the CERMIT experiment the tip interacts with a spin directly below the tip, a distance d from the tip's surface. (b) In the OSCAR experiment the situation is the same, except the spin is also displaced laterally by a distance x.

OSCAR

The OSCAR (*oscillating cantilever-driven adiabatic reversals*) protocol [38–40] works, briefly, as follows. The cantilever is oscillated, producing a changing magnetic field at the location of the spin. The spin will therefore have a Larmor frequency which depends on the cantilever position. For clarity in what follows, define the Larmor frequency for the spin ω_0 as its resonance frequency when the cantilever is at its equilibrium position. At one of the extremes of the cantilever's motion an rf field is turned on, at ω_0. Because the cantilever is displaced, shifting the field, this is not experienced by the spin as a resonant field, and if the tip field gradient ($\partial B_z/\partial x$ in the coordinates of Figure 5.2) times the cantilever displacement is large compared to the resonance linewidth, ω_0 can be said to be far off resonance at this time. As the cantilever sweeps through its equilibrium position,

the field sweeps through resonance, causing an ARP of the spin (assuming the adiabatic condition is met). Although the roles of the field and rf frequency are switched here, it operates exactly as ARP as discussed in section 2.2.7 (and indeed sweeping the field, not the frequency, was the method used in early NMR [65]). As the cantilever oscillates, the spin is repeatedly inverted in phase with the cantilever's motion. This produces a time-dependent force on the cantilever which, because it is exactly in phase (or exactly π out of phase) with the cantilever is indistinguishable from a static force which varies as the *position* of the cantilever, i.e. a force gradient, and a shift in the cantilever frequency is observed.

Note that in the OSCAR protocol if the cantilever is perpendicular to the surface a single spin must be displaced to either side to produce a signal. For this reason another variable is introduced to the analysis below, namely the transverse displacement of the spin x, as shown in Figure 5.2(b).

In [39] an estimate of the OSCAR signal size is given which translates to, in the present notation,

$$\Delta f = \pm \frac{2\mu f_0}{\pi k x_{\mathrm{pk}}} \frac{\partial B_x}{\partial z}, \tag{5.9}$$

where x_{pk} is peak-to-peak driven motion of the cantilever. The sign is given by the phase of the spin flips with respect to the cantilever motion. This can be written in terms of a spring constant shift via equation 5.3. Choosing the positive sign, this gives

$$\Delta k = \frac{4\mu}{\pi x_{\mathrm{pk}}} \frac{\partial B_z}{\partial x}. \tag{5.10}$$

To maximize this expression the tip field gradient is considered as a function of tip size a, distance from the surface to the magnet center z, and a lateral

displacement x. From equation (1.2),

$$B_z = \frac{\mu_0 M a^3}{r^3}\left(\frac{3z^2}{r^2} - 1\right) = \mu_0 M a^3 \left(\frac{3z^2}{(x^2+z^2)^{\frac{5}{2}}} - \frac{1}{(x^2+z^2)^{\frac{3}{2}}}\right). \tag{5.11}$$

Taking the derivative of the tip field is in the x direction,

$$\frac{\partial B_z}{\partial x} = \mu_0 M a^3 \left(\frac{3x}{(x^2+z^2)^{\frac{5}{2}}} - \frac{15z^2 x}{(x^2+z^2)^{\frac{7}{2}}}\right). \tag{5.12}$$

With d fixed (recall $z = a + d$), a numerical maximization gives $x/d \approx 2.320$, $a/d \approx 3.000$, at a value of

$$\frac{\partial B_z}{\partial x} \approx -0.096 \mu_0 M \left(\frac{1}{a}\right), \tag{5.13}$$

so

$$\Delta k \approx 0.384 \frac{\mu \mu_0 M}{\pi a x_{\mathrm{pk}}}, \tag{5.14}$$

and

$$\mathrm{SNR}_{\mathrm{OSCAR}} \approx 0.043 \frac{\mu \mu_0 M}{a F_{\mathrm{min}}}. \tag{5.15}$$

Notice the lack of dependence on oscillation amplitude—the x_{pk} from equation 5.10 has cancelled with the x_{rms} from equation 5.7 to produce a factor of $2^{-3/2}$.

The results of these scaling calculations are summarized in Table 5.1. The scaling of the SNR for the OSCAR protocol is quite similar to the parallel-geometry force method, but with a value less than a tenth as large. The situation is similar for CERMIT if one assumes that the rms cantilever excitation should be no larger than about one tenth of the magnet diameter, i.e. $(x_{\mathrm{rms}}/a) \sim 1/5$. If, on the other hand, larger vibration amplitudes are usable, then CERMIT appears to have an advantage over OSCAR. The interplay between distance and magnet size, hidden from view in the form given in table 5.1, must also be taken into account. If all techniques have the same tip-sample distance d, the CERMIT signal is optimized

Table 5.1: Summary of scaling results for various MRFM protocols.

protocol	signal estimate	$\mathrm{SNR}/\mathrm{SNR}_{\mathrm{Force}}$	a/d
Force	$F_z \approx 0.633\frac{\mu\mu_0 M}{a}$	1	3
CERMIT	$\Delta k_x \approx 0.311\frac{\mu\mu_0 M}{a^2}$	$0.491\frac{x_{\mathrm{rms}}}{a}$	3/2
OSCAR	$\Delta k \approx 0.384\frac{\mu\mu_0 M}{\pi a x_{\mathrm{pk}}}$	0.068	3

with a tip of half the diameter of that in the other two methods, giving a SNR gain of a factor of two. In summary, OSCAR is about a factor of ten worse than parallel-geometry force detection, and CERMIT is about a factor of five worse than parallel-geometry force detection on the assumption $(x_{\mathrm{rms}}/a) \sim 1/5$.

This is the irony of ultrasoft cantilevers—they appear, by virtue of their low F_{min} values, to give a sensitivity increase over earlier generations of cantilevers by a few orders of magnitude. However, the cantilevers are so soft that they must be used in the perpendicular geometry, so one must give back an order of magnitude in tip-sample coupling to be able to use them!

5.3 Apparatus

5.3.1 Probe head

One of the difficulties of performing magnet-on-cantilever experiments, as discussed in section 1.2.1, is the interaction of the magnetic tip with the external field. If the magnet has a preferred magnetization direction, sometimes called an *easy axis*, large torques can be placed on the cantilever due to the tendency to align this axis with the external field. If bending the cantilever changes the angle of the easy axis with the field, the restoring torque can change the effective spring

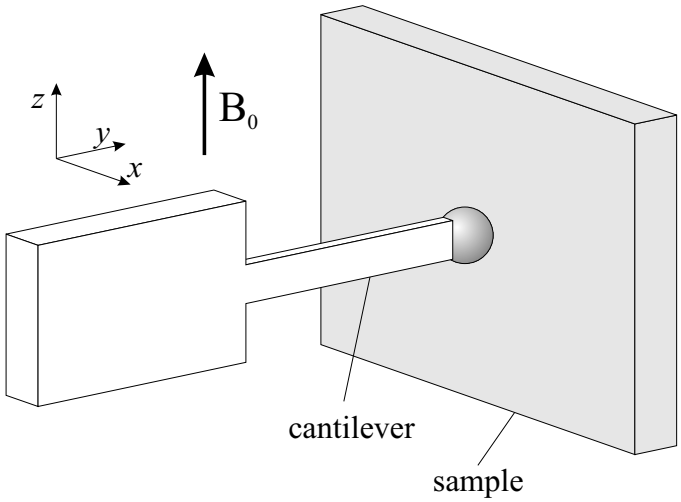

Figure 5.3: In the cantilever-width-parallel-to-field configuration, the field is perpendicular the the cantilever's plane of motion. Therefore the orientation of the tip with respect to the field does not change when the cantilever bends (in x), problematic interactions between the tip and field are minimized. The tip should be oriented so that its direction of preferred magnetization is also parallel with the field direction.

constant of the cantilever. This can result in unwanted cantilever frequency shifts and a reduction in the effective cantilever quality factor, resulting in a lowered sensitivity [16,59]. These effects can be minimized by operating the cantilever in a configuration in which the width of the cantilever and the easy axis of the magnet are aligned with the field [59,60], as shown in Figure 5.3. In this arrangement the orientation of the magnet does not change when the cantilever bends. The spin interaction is slightly different than that described in section section 5.2 because of the different orientation of the magnetization of the tip and the spins, but the idea is the same.

In order to achieve this configuration an entirely new probe was created for CERMIT experiments—the probe head simply would not fit fit in the vacuum

system used in Chapters 3 and 4. Also, because of the disappointing performance of the half-wave line tank circuit design, new rf circuitry was desired.

The probe head consists of a 2.188" Cu plate and a number of brass components which bolt to this plate. Figure 5.4 shows the arrangement of these components, oriented so that the z axis as defined in Figure 5.3, parallel to B_0, points into the page.

The fiber positioner, used to align the fiber-optic interferometer to the cantilever, is based on a kinematic mount design, as used in standard mirror positioners. The mount consists of a bottom plate which bolts rigidly to the Cu plate, and an upper plate with three 1/4-100 tapped through holes. Through these holes pass three ball-bearing tipped stainless adjuster screws which contact the lower plate at a conical hole, a groove, and a flat, respectively. The conical hole is placed beneath the "home" adjuster screw, the one closest to the cantilever. In this arrangement, the position of the optical fiber, which is fixed to the upper plate, can be moved in three dimensions—moving all three screws simultaneously provides z adjustment, and extending either of the two non-home screws rocks the plate in two approximately orthogonal arcs, which, for small motions about the level position, approximate x and y motion. The fiber adjuster has a groove on its top surface into which the optical fiber is held with a small Be-Cu clip.

The brass cantilever mount is adjacent to the fiber positioner and is fixed to the Cu plate by two 4-40 screws. The cantilever die is affixed with Apiezon N grease to the surface of the brass cantilever mount. There is a ledge on the mount, which the side of the die closest to the Cu plate rests against, ensuring that the cantilever is orthogonal to the external field B_0. The cantilever is electrically connected to a wire through the silicon layer on the die (which is part of the same single crystal

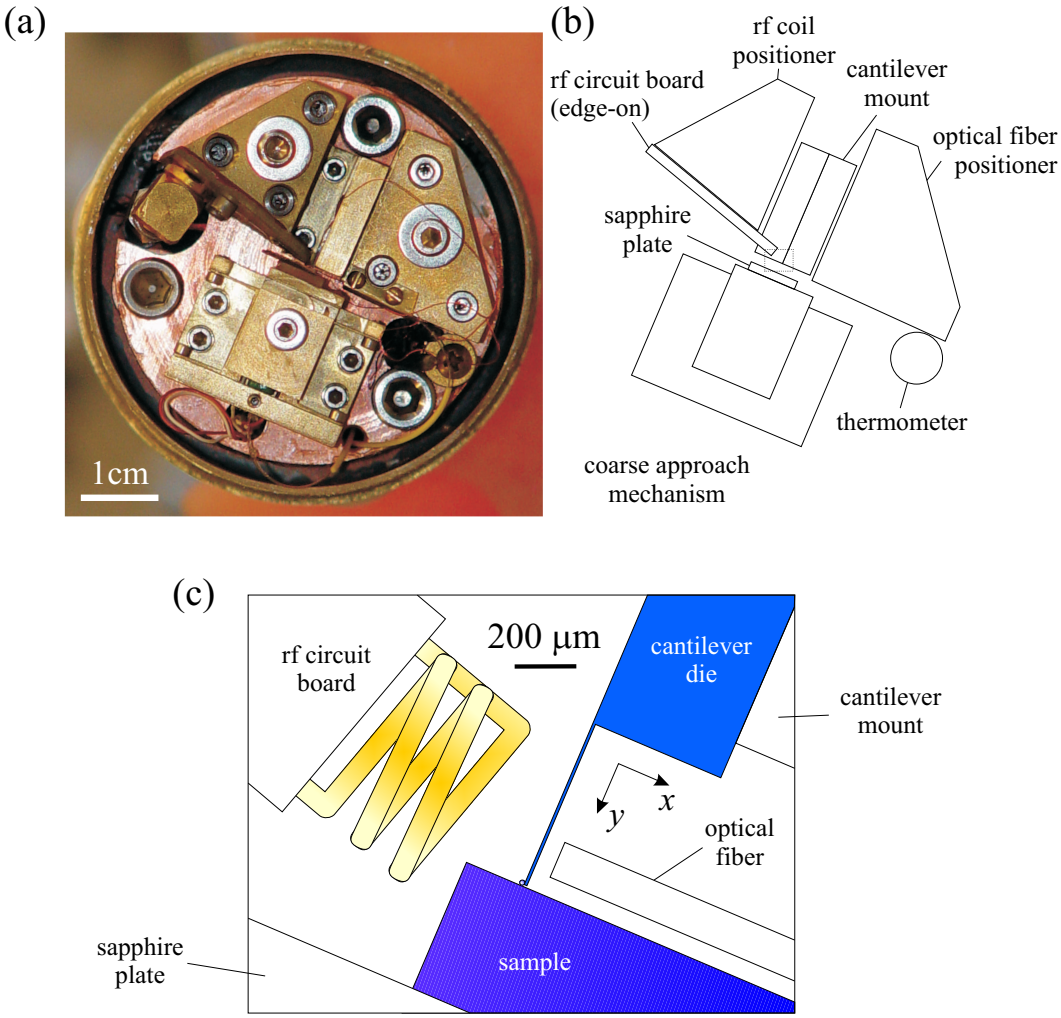

Figure 5.4: (a) Photograph of probe head, oriented so that the external magnetic field B_0 points into the page. (b) Diagram at same size scale as photograph showing main components. (c) Closeup of the region surrounded by a dashed box in (b), with orientation preserved, showing the arrangement, approximately to scale, of the main experimental components.

as the cantilever) with a dab of silver paint.

The rf circuit is a printed circuit board (PCB) design borrowed from the micro-coil liquid NMR community [106]. Figure 5.5 shows a diagram of the main parts of the PCB and a photograph of an assembled circuit. (The coil in Figure 5.5(a) is enlarged for clarity.) Not visible in Figure 5.5 is a ground plane on the back side of the PCB. At the left of 5.5(a) is a hole which accepts the center pin of an SMA connector, visible in 5.5(b). Four holes are drilled through the board which admit the four ground posts of the connector, which are soldered to the ground plane on the back side. A stripline, designed to have characteristic impedance of 50 Ω in parallel with the ground plane at 350 MHz, carries signals to the coil, the legs of which are soldered across the board, i.e. one to the stripline and one to the ground plane. Tuning of the tank circuit is achieved using ceramic cell phone capacitors. The matching capacitor is soldered across a break in the stripline. The tuning capacitor connects the stripline to the ground plane by means of a a hole through the board which is coated on its inner surface with metal during manufacture. The circuit is tuned and matched at low temperature by trial and error. A set of capacitors is soldered in, the circuit is cooled to 77 K and tested with an rf sweeper [4]. This process is iterated until the circuit is tuned to an acceptable value, and slightly unmatched in a way which a trained eye can tell will produce a good match at 4 K. For details on the circuit design and the esoteric tuning process, see [107].

The coarse approach mechanism is a modified slip-stick type with sapphire spheres riding in machined brass grooves. It is based on the Silveira design [108], but modified to support the sample surface in a vertical plane, and approach hor-

[4]Morris Industries, model 505NV+.

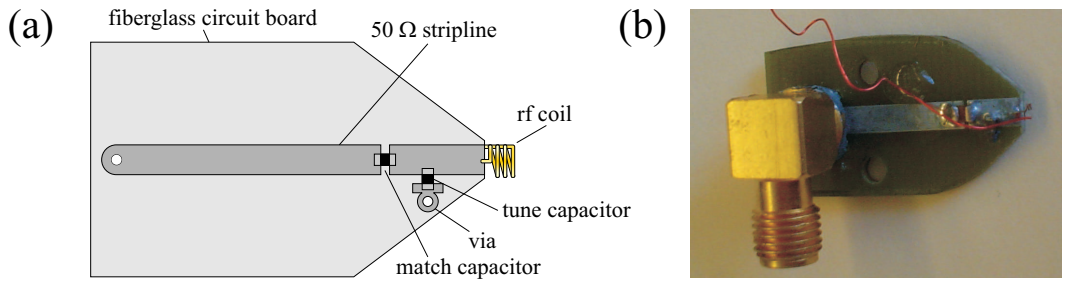

Figure 5.5: (a) Diagram and (b) photograph of printed rf circuit. The wire stuck to the circuit board is not part of the rf circuit. It is used to provide capacitive coupling to the cantilever. The size of the coil is exaggerated for clarity in (a).

izontally. The sample is mounted on a sapphire plate with Apiezon N grease. The sapphire plate is glued to a moving element of the coarse approach mechanism with a Cu foil sandwiched between the two. The Cu foil is clamped under the coarse approach mechanism to the Cu plate, providing a flexible thermal conduit. For details of the design, fabrication, and operation of the coarse approach mechanism, see [107]. Coarse-approach displacement is monitored by a second fiber-optic interferometer.

The Cu plate bolts to the probe via three 1/4-28 bolts, which are surrounded by cylindrical Cu sleeves, 3/8" O.D., 1/4-28 clearance I.D., 5/8" in length, which provide thermal contact. All bolts in the probe head which enter blind holes, including the 1/4-28 bolts which attach the probe head to the probe superstructure, are vented. A Lakeshore Cernox thermometer is bolted to the Cu plate at the location shown in Figure 5.4(b), with a dab of Apiezon N grease between the two.

5.3.2 Vacuum system and overall structure

The vacuum system is a two-chamber design, in which a lower cylindrical chamber, which contains the main experimental components, is connected by four stainless steel pump lines to a top chamber, which has flanges for feedthroughs, and allows relatively easy access to the insides of the feedthroughs through a larger top flange. The pump lines support blackbody radiation baffles and double as conduits for wires, stainless steel semirigid rf coaxial cable, and optical fiber. The lower chamber consists of a brass cylindrical can which attaches to a Cu cylinder via a 1-degree seal. Both halves of the 1-degree seal are brass, and the top side is silver soldered to the Cu cylinder, the bottom side silver soldered to a 2.75" I.D., 1/16" wall brass tube. The bottom chamber is completed by a brass end-cap silver soldered to the brass tube. The Cu cylinder is drilled with four holes into which the stainless steel pump lines are silver soldered. The pump lines consist of three 1/4" O.D., 0.035" wall tubes, which are arranged in an equilateral triangle and provide the main structural support, and one 5/8", 0.020" wall tube which provides additional pumping area. A small brass rod with brass blackbody radiation baffles silver soldered to it fits into the 5/8" tube. The baffles have flats and slots to allow the passage of wires and rf coaxial cable, respectively, down the tube. The 1/4" tubes are stuffed with brass wool at the cold end to block blackbody radiation. On the bottom face of the Cu cylinder are three blind, 1/4-28 tapped holes to accept the probe head.

At the top chamber, all feedthroughs are based on modified NW-40 flanges. Wires are passed through a 19-pin hermetic military connector which is soldered into a drilled flange. Nine twisted pairs of Cu wire are passed through the 5/8" tube, protected by a fiberglass sleeve. These wires are connectorized at both ends.

The tops plug into corresponding connectors at the inside of the feedthrough in the top chamber. At the lower end they plug into a short section of connectorized wires which are wrapped around a copper cylinder, 5/8" long and 1/2" diameter, which is silver soldered to the lower face of the Cu cylinder. Finally wires to the probe head plug into the lower end of this short section of wires. The stainless semirigid coaxial rf cable is connectorized at its top and bottom ends with SMA connectors. At the top end it is attached via a SMA-BNC adapter to the inside of an o-ring based BNC rf feedthrough mounted on a drilled NW-40 flange. Optical fibers are fed through modified Swagelock connectors welded into a drilled NW-40 flange and which have had their o-ring assemblies replaced with Teflon ferrules [98].

5.4 Experiment

Experiments were carried out in high vacuum, at 4.4 K as measured at the Cu plate, and at ~ 7 T. At these conditions, the cantilever was measured to have a resonance frequency $f_0 = 854$ Hz and a quality factor $Q = 43\,900$. The cantilever was custom-fabricated [92] from single-crystal silicon, with a calculated spring constant k of 6×10^{-5} N/m. The calculation was deemed to be reliable because in many other measurements, by the thermal motion spectral method described in section 2.3.2, of cantilevers produced in the same way the spring constant was found to be within 20 % of the calculated value.

The tip was a 9 µm diameter spherical Ni magnet, shown in Figure 5.6. The tip was glued to the cantilever under a long-focal-length stereo microscope using a homebuilt brass fixture and optical micrometers using the following process. Spherical Ni powder[5] was spread out on a polished brass plate. A region with a

[5]NOVAMET, Spherical Ni powder, 4SP-400 Mesh.

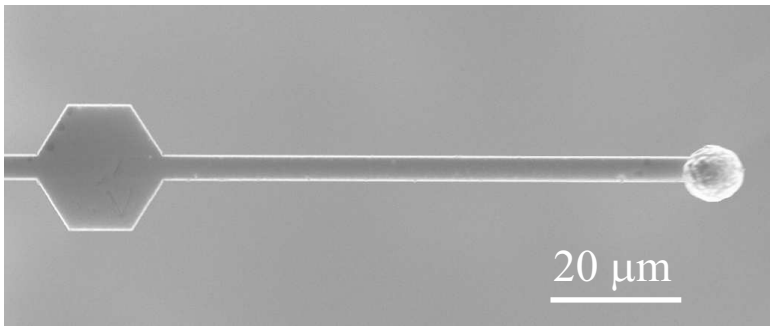

Figure 5.6: A scanning-electron micrograph of the end of the custom-fabricated cantilever and magnetic tip. The wider section of the cantilever is a laser reflection pad used for fiber-interferometric detection of the cantilever displacement. The tip is a 9 μm Ni sphere which was epoxied to the end of the cantilever.

desirable density of Ni spheres—enough that there were many to choose from, but not so many that they are touching each other—was found under the microscope, and a dab of epoxy[6] was placed nearby using the wooden shaft of a cotton swab, broken to produce a very fine point. The cantilever die was attached to a brass mount, which was bolted to a three-axis micrometer stack, with double-stick tape so that the cantilever was pointing downward, perpendicular to the polished brass surface. Using the micrometers for control while monitoring through the microscope, the end of the cantilever was dipped in the epoxy, a few microns deep. When the cantilever was retracted from the glue it held a droplet a few microns across of epoxy, which was then touched to a Ni sphere which adhered to the droplet due to surface tension. In order to achieve the orientation described at the beginning of section 5.3 (see Figure 5.3), the cantilever was then rapidly transported to another building and placed in a specially made fixture which was inserted into a 5 T NMR

[6]Loctite Extra Time, set time ~ 45 min.

magnet, kindly provided by Prof. T. Michael Duncan, while the epoxy set.

Because of the low spring constant of the cantilever, it is highly susceptible to static electricity on other parts of the probe, such as the optical fiber. Static electricity can cause cantilever resonance frequency shifts, and was also found to decrease cantilever sensitivity. To reduce static electricity the area around the cantilever was exposed to a polonium antistatic source[7] for about 60 s as the final step prior to closing the vacuum system.

The external polarizing field $B_0 \sim 7$ T was provided by a liquid-He cooled superconducting magnet. The probe was placed in a vacuum-insulated insert, as described in section 4.2. During experiments the probe was submerged in liquid He, drawn in to the insert by a capillary from the magnet He reservoir.

The sample was GaAs coated with ~ 20 nm of Au, courtesy of Dr. Doran Smith of the U.S. Army Research Laboratory, Adelphi, MD. GaAs contains three magnetic nuclear species, ^{69}Ga, ^{71}Ga, and ^{75}As. All three have spin 3/2. Experiments in this chapter will use the ^{71}Ga, which has a gyromagnetic ratio of $\gamma_{^{71}\mathrm{Ga}} = 12.98$ MHz/T. A similar sample's relaxation times were well characterized at low temperature by previous MRFM experiments [46]. The sample was electrically connected with a dab of silver paint to a wire accessible outside the probe.

The voltage between sample and cantilever was set to 0.4 V, which was found by ring-down time to minimize the drag between the cantilever and the sample surface [16]. This is necessary because a voltage difference between the sample and the cantilever tip can induce a charge patch in the two because of the capacitance between them. Even if both are grounded, a work function difference between the tip and sample can still induce a charge. As the cantilever moves parallel to the

[7] Staticmaster 1U400, AMSTAT Industries.

sample surface this charge patch is dragged back and forth, dissipating cantilever energy resistively and reducing the apparent Q of the cantilever. The dissipation is proportional to the square of the voltage, with a minimum where the work function difference is most effectively offset [80].

The coil was ~ 500 µm in diameter, and at 4 K was tuned and matched with $Q \sim 90$ at 88.075 MHz. This frequency corresponds to a ^{71}Ga resonant field of 6.785 T.

The cantilever resonance frequency was monitored using a positive feedback circuit in which the cantilever acts as a resonant element [78,104]. A block diagram of this arrangement is shown in Figure 5.7. The cantilever is measured with a fiber-optic interferometer, the output of which is a voltage proportional to cantilever displacement. This signal is high-pass filtered to remove the DC component, then sent to a resonant LC filter. This serves both to suppress background noise at frequencies away from the cantilever resonance and to phase shift the cantilever signal by an amount $\phi \approx \pi/2$, provided the cantilever signal is approximately on resonance for the LC circuit. The capacitor in the LC circuit can be switched out to make sure this is true. This signal goes to a frequency counter[8] for measurement, and to a comparator which is referenced to ground and supplied with a standard 5 V TTL reference voltage. The comparator outputs 0 V when the cantilever signal is negative, and 5 V when it is positive, converting the signal to a 5 V square wave. The comparator output is multiplied by a set point voltage V_{set} and used to drive the cantilever.

One advantage of this technique is that the cantilever frequency can in principle shift instantaneously [104], unlike its amplitude, which takes a cantilever

[8]Stanford SR620.

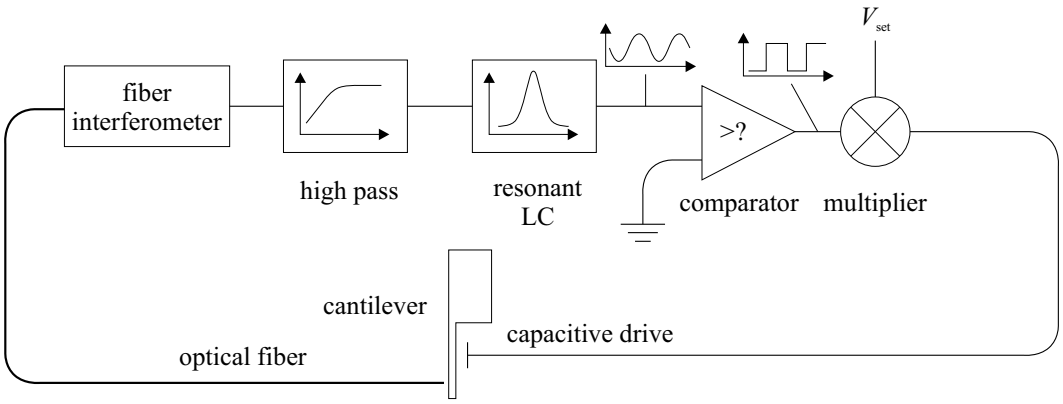

Figure 5.7: A block diagram of the positive-feedback cantilever frequency measurement arrangement.

characteristic time to change (see section 2.3).

5.5 Results

Figure 5.8 shows the output of the frequency counter when ARP sweeps were delivered at various applied magnetic fields. The sweeps generally had no discernible effect on the cantilever frequency when the rf was out of resonance with the sample spins (7.050 T, filled circles, Figure 5.8). Occasionally, a small, short-lived shift was observed after one or both of the sweeps (7.025 T, open circles). The appearance of these responses was unpredictable, possibly because they depend on the phase of the cantilever at the time of the sweep.

At 6.775 T (open triangles) the sweep produced an inverted region of spins (see diagram in Figure 5.1), causing a -70 mHz jump in the cantilever frequency. This shift corresponds, via equation 5.3, to a force gradient of about 10 nN/m. At 6.900 T a positive frequency shift was observed. When a second, identical sweep was applied to return the spins to equilibrium, the recovery of the cantilever frequency was imperfect, consistent with an incomplete restoration of sample magnetization

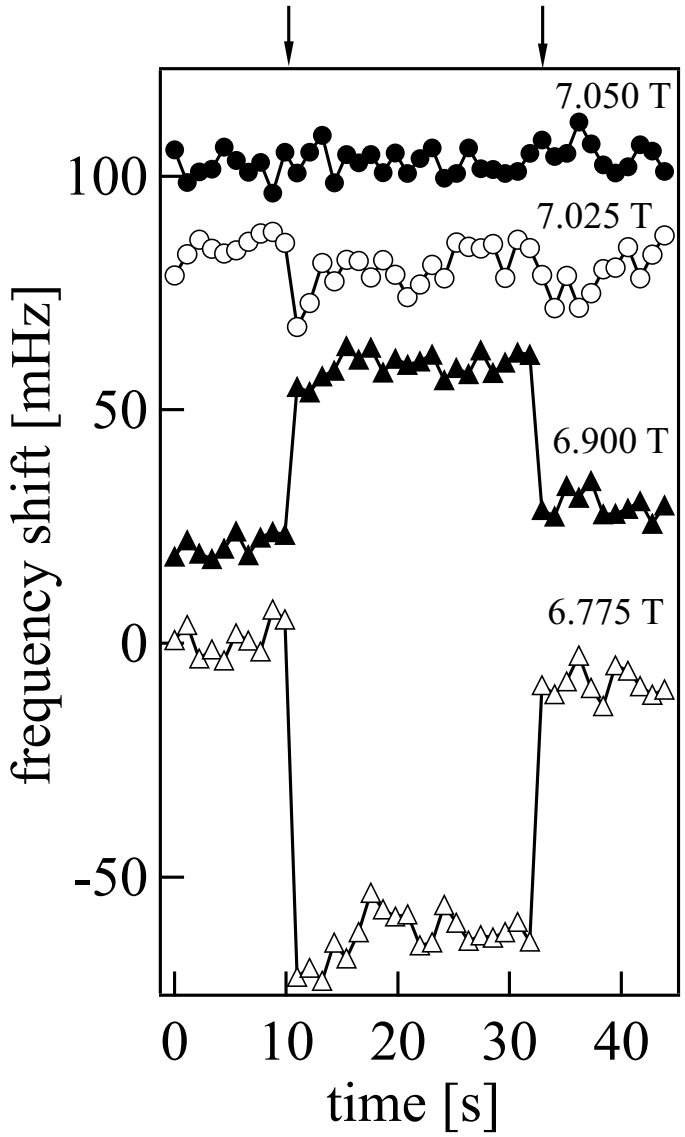

Figure 5.8: Output of the frequency counter when ARP sweeps were given at various fields. Traces are offset for clarity.

(due, possibly, to the "dead" zones at the endpoints of the ARP sweeps).

As an example of the size of the signals involved, at 6.900 T the shift of 38 mHz corresponds to a change in force gradient of 5.3×10^{-9} N/m. Spins contributing to this signal experience an estimated magnetic field second derivative of $\partial^2 B_z/\partial x^2 \cong 2 \times 10^{10}$ T/m^2. Given that the Curie-law magnetic moment of ^{71}Ga is 1.06×10^{-29} J/T per nucleus at 4.4 K and 7 T, this signal is due to $\sim 1.3 \times 10^{10}$ nuclei.

Figure 5.9 is a plot of the cantilever frequency shift versus external magnetic field. Notice that the resonance feature is centered at roughly 6.8 T, compared with an expected resonant field of 6.785 T at 88.075 MHz for ^{71}Ga. For ^{69}Ga, with its gyromagnetic ratio of $\gamma_{^{69}Ga} = 10.2$ MHz/T [22], the peak would be located at ~ 8.6 T, so the two isotopes are clearly distinguishable in this experiment. The lineshape is composed of a negative, low-field peak and a smaller, positive, high-field peak. As will be seen in section 5.6, the high-field peak is due to spins in the high-gradient region near the tip. Here, $\partial^2 B_z/\partial x^2$ is strongly positive and the spins are pointing down, for an overall positive shift (see equation 5.1). The signal collected in this field range is from a small volume of spins localized near the tip, and is of interest for imaging experiments [18, 27].

The negative peak in Figure 5.9 is due more complicated volumes of spins which interact with weaker, negative regions of $\partial^2 B_z/\partial x^2$. These spins experience a much smaller first derivative of the tip field and therefore a much larger volume of spins is inverted by the sweep, resulting in a larger signal despite the smaller second derivative. This is analogous to the "zero-tip-field resonance" observed by Suter *et al.* [109] in ESR MRFM experiments. The shapes of the sensitive slices responsible for the signal at various fields will be considered in detail in section 5.6.

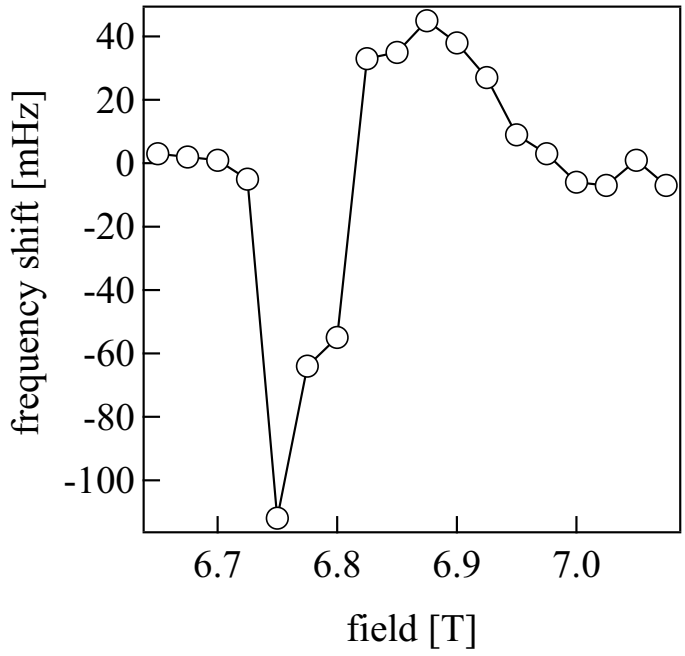

Figure 5.9: Cantilever frequency shift as a function of field.

Sensitivity

The sensitivity of this experiment was limited by a background frequency jitter (Allan variance) of 2 mHz in a one hertz measurement bandwidth, equivalent to fluctuating force gradient with spectral density $S_k^{1/2} = 3 \times 10^{-10}\mathrm{N/m}\sqrt{\mathrm{Hz}}$. Assuming a spherical shape for the tip, a tip-sample distance of 160 nm, and a saturation magnetization for the Ni tip of $M = 0.6T/\mu_0$ gives a field gradient estimate just inside the sample of $\partial^2 B_z/\partial x^2 \cong 2 \times 10^{10}$ T/m^2. The associated minimum detectable nuclear magnetic moment for spins in this region is then $\mu_{\min} = 7.5 \times 10^{-21}$ J/T in a one hertz bandwidth. This is equal to the Curie-law magnetic moment from 7.1×10^8 ^{71}Ga nuclei occupying (0.44 µm)^3 in GaAs.

The frequency measurements in this experiment were not thermally limited. While the position noise of the undriven cantilever was consistent with thermal fluctuations, the observed $S_k^{1/2}$ was six times higher than the thermomechanical

limit [104]. Insufficient vibration isolation is one possible source of the excess frequency jitter.

To put this result into perspective in terms of the larger MRFM goal of single-proton sensitivity, the sensitivity numbers above can be recast in terms of a minimum detectable magnetic moments equivalent to 5×10^5 polarized proton magnetic moments. (This form is also convenient because protons have spin 1/2, and so the question of how many polarized spins are contributing to the signal (i.e. the up spins minus the down spins) makes sense. With spin-3/2 nuclei such as ^{7}1Ga this notion is less clear.) This was, at the time of its publication [48], the highest nuclear MRFM sensitivity ever reported.

5.6 Numerical analysis of results

This section provides some further analysis of the experimental results presented in the previous section. Numerical calculations calculations of the expected signal were performed in order to explain the origin of the peculiar lineshape observed. The results of those calculations are presented here, along with some plots which show the shape of the sensitive slice at various external field values.

5.6.1 Numerical calculation of expected signal

In MRFM imaging experiments, whether of the slice-deconvolution [25] or Fourier-encoded [18] type, it is important to understand the shape of the sensitive slice. For this reason, and to explain the line shape shown in Figure 5.9, numerical calculations of the expected signal were performed in C++. The code was primarily written by another graduate student, Jahan Dawlaty, and will not be presented in detail here. The algorithm used will be described, and results will

be discussed.

As discussed in section 5.2, if the tip's motion is small enough that the adiabatic condition is met, equation 5.2 is a good approximation for the signal in a CERMIT experiment. Assuming that this is the case, and also that the "dead" zones at the two extremes of the slice do not detract significantly from the signal, then performing the integral in equation 5.2 over a the volume enclosed between the surfaces of constant field which are in resonance at the two extremes of the sweep will provide a good approximation to the signal.

The integral was performed on a grid of constant spacing s consisting of $200 \times 100 \times 100$ points, lying in the positive x and z quadrant of the sample. Because the function $\partial^2 B_z/\partial x^2$ is symmetric about the x and z planes, the total integral is then given by four times the result in the calculation volume. Therefore the total calculational volume should be considered to be equal to $200s \times 200s \times 200s$. Each point represents a volume of size s^3, which is assumed to possess a magnetic moment $\rho_m s^3$, where ρ_m is the Curie-law magnetization density as given by equation 2.18. This allows the integral to be cast in a discretized form:

$$\Delta k = 4 \sum_k \frac{\partial^2 B_z}{\partial x^2}(\mathbf{r}_k)\, \rho_m\, s^3. \tag{5.16}$$

Properly, ρ_m should depend linearly on the applied field. However, this effect should be small, since the entire width of the resonance feature in Figure 5.9 represents a change in field of only about four per cent. Furthermore, the sample magnetization takes a time T_1 to equilibrate to a new field value, and in this sample at 4.4 K, T_1 is roughly 20 minutes [46, 47], which is similar to the time it took to collect the entire curve. For these reasons a constant ρ_m was assumed, based on an external field of 6.875 T. The width in field units of the sensitive slice ΔB is given by the frequency width of the ARP sweep divided by the gyromagnetic ratio

for ^{71}Ga, which gives 7.7×10^{-2} T.

The algorithm is as follows. First, the z component of the tip field $B_z(\mathbf{r})$ and it's second gradient $\partial^2 B_z/\partial x^2$ were calculated for each grid point $\mathbf{r}$ and deposited in a file. These were saved so they could be checked later. The calculation proceeded by performing the sum in equation 5.16 for a number of different resonant slices centered at external applied fields B_n. For each B_n, the field value at each grid point was checked. If it fell in the range

$$\frac{B_n - \Delta B}{2} < B_z(\mathbf{r}) \leq \frac{B_n + \Delta B}{2}$$

that point was considered to be inside the sensitive slice, and it contributed to equation 5.16. If not, that point was disregarded. The points which were deemed to be inside the slice were recorded in a file to be examined at a later time. This allowed the slice shapes and locations at each field point to be understood.

The results of this procedure are plotted in Figure 5.10. Figure 5.11 is a representation of the inverted volumes for the field points at which data were taken. The amplitude of the calculated signal was about a factor of four larger than the measured signal. The reason for this discrepancy is not known, but some possible origins are discussed at the end of this section. However, the numerical code excellently predicts the width, location, and overall qualitative shape of the signal with no free parameters. The three regions labelled in Figure 5.10 will be considered separately. Region III, the high-field region, is due to spins near the tip. Region III in figure 5.10 corresponds to the slice represented in Figure 5.11(a) and panels (i) through (iv) in Figure 5.11(b). Panel (v) corresponds to the point on the border between regions II and III.

A three-dimensional view of surfaces of constant field, which form the boundaries of the slices, is shown in Figure 5.12. The inverted volumes in region III in

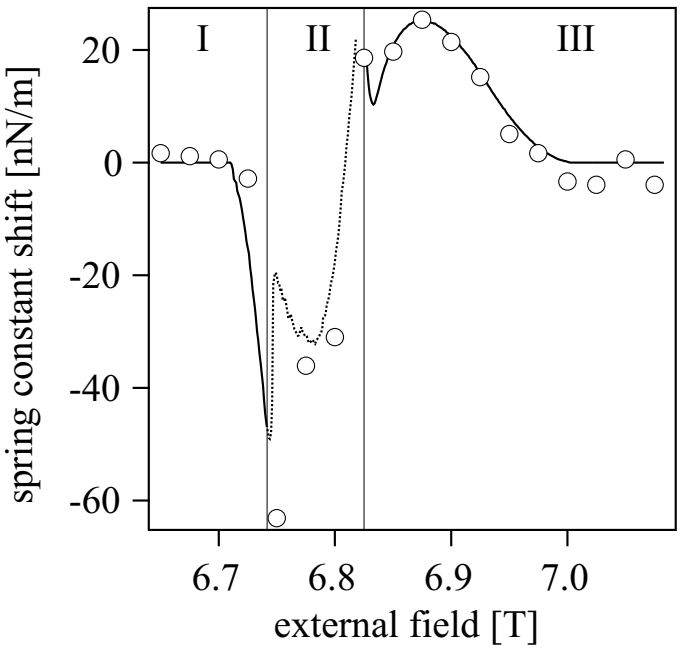

Figure 5.10: A plot of the experimental cantilever spring constant shift as a function of field (circles) with the results of numerical calculations (lines). Numerical results have been scaled by a factor of one fourth for easier comparison with the measured data. The location, width, and overall shape of the resonance feature are predicted extremely well with no free parameters.

Figure 5.10 have boundaries like the red, yellow, and green surfaces in Figure 5.12. (The plots in Figures 5.11 and 5.12 were generated in Matlab, but their shapes were confirmed to match the slice outputs of the C++ code.) Region II is where the sensitive slice intersects the conical surfaces of zero tip field. Here the region which is in resonance, shown in panels (vi)-(viii) in Figure 5.11(b), and by the cyan surface in Figure 5.12, is infinite in extent. Finally, the low-field region, region I, results from non-simply-connected, two-lobe slices as shown in panel (ix) in Figure 5.11, and the blue and purple surfaces in Figure 5.12.

In Region I a grid spacing of $s = 500$ nm was used. Because the behavior at the

extreme low-field end of the resonance line depends on two small lobes displaced in z [see Figure 5.11(b), panel (ix) and Figure 5.12, purple surface], initially a finer grid, displaced in z by an amount designed to capture these lobes, was tried. However, it was found the the behavior only differed from the 500 nm grid by a few percent, so this more complicated approach was discarded. Although only a few experimental data points are available here, the observed behavior is reproduced well by the numerics. A similarly steep negative jump is observed, at a location which agrees well with the data.

Region II was found to be extremely difficult to simulate. This is due to the fact that the slices here are infinite in extent, yet have components near the tip of which the detailed shape is important. Figure 5.11(b), panels (vi)-(viii), show this behavior—far away parts of such a slice have enough volume to matter, requiring a large calculation volume, but the shape of the nearby boundary is also important, requiring a fine grid size. A 500 nm grid seemed to balance these factors the best[9]. It produced a signal magnitude similar to larger grids, but was still fine enough that it did not develop jumps because of slight changes in the shape of the boundary of the inverted volume near the tip. The calculation results are presented in a dotted line here to indicate that these results are considered less reliable than the rest.

In region III a grid spacing of $s = 100$ nm was used. This did not produce significantly different results at the high-field extreme from that of a 50 nm grid, the smallest examined, and was large enough to keep the entire resonant slice inside the calculation volume for all field values in region III. Here we found that

[9]In future experiments it would make sense to collect more data in this rapidly-changing region. In that case it would be worthwhile to perform a numerical calculation with a nonuniform mesh in order to capture the details of the behavior here.

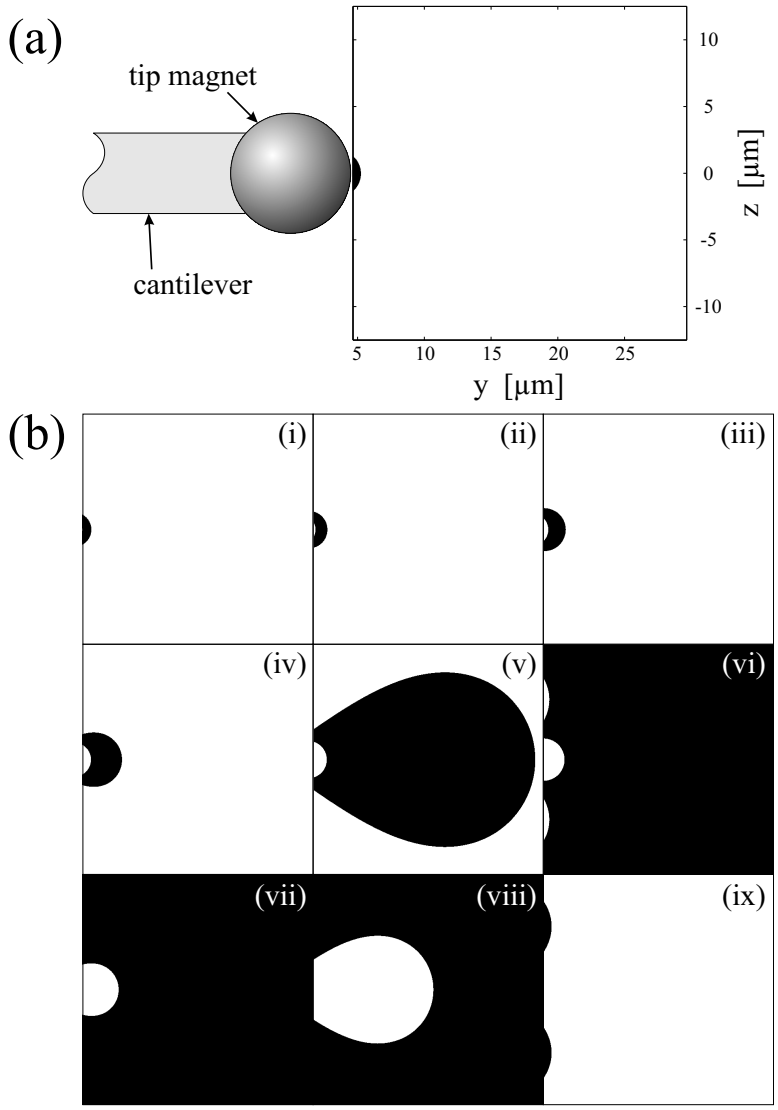

Figure 5.11: Slices at $x = 0$ of resonant volumes, calculated at the field values at which data were taken. The magnetic tip is indicated, to scale, in part (a). The external field in (a) is the resonant field for the experimental conditions in the absence of the tip, 6.785 T, plus a shift of +0.165 T. This corresponds to the sixth data point from the right in Figure 5.10. In (b) the field shifts are: (i) +0.140 T, (ii) +0.115 T, (iii) +0.090 T, (iv) +0.065 T, (v) +0.040 T, (vi) +0.015 T, (vii) -0.010 T, (viii) -0.035 T, (ix) -0.060 T. Panel (v) corresponds to the point on the border between regions II and III in Figure 5.10. Panel (viii) corresponds to the maximal (negative) signal, i.e. the leftmost datapoint in region II of Figure 5.10.

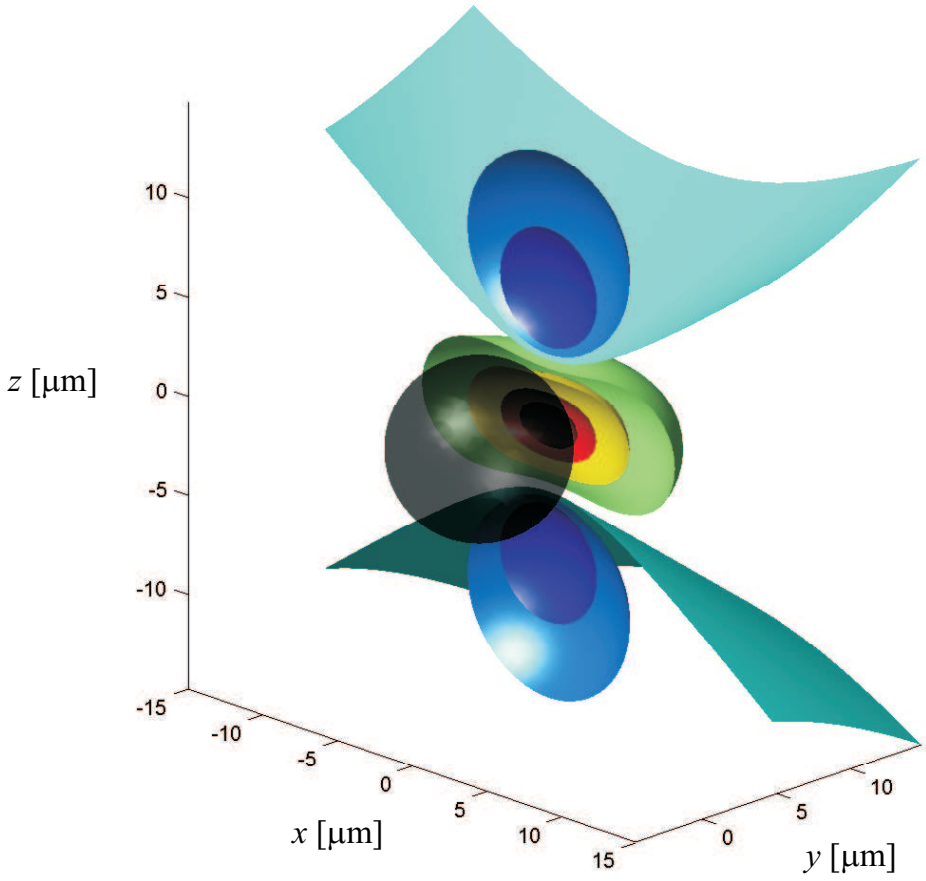

Figure 5.12: Computed surfaces of constant B_z. The magnetic tip is represented, to scale, by the semitransparent black sphere.

the calculations reproduced the observed behavior extremely well. Not only are the location and width of the high-field feature correctly predicted, but the overall shape is matched quite accurately. It is volumes of this type which would be of interest for imaging experiments, and so it is important that these be well understood.

Overall the agreement with experimental observation is quite good. The question of the mismatch in amplitude—recall the calculated curves in Figure 5.10 have been divided by four—remains unanswered, but a number of explanations may be ruled out immediately. It cannot be that the tip magnetization in the experiment differed significantly from that in the numerical model, because this would cause the width of the resonance feature to be significantly different. This can be seen analytically—the width of the resonance feature is the span of fields present in the sample due to the tip, broadened by the slice width—but was also checked numerically. Reducing the tip magnetization by only a factor of two (too small to account for the discrepancy) produced a significantly narrowed resonance feature. An incorrect distance cannot be at fault for the same reason, which was also checked in numerical calculations. The obvious remaining parameter is the sample magnetization—it is possible that the sample was significantly warmer than the probe at the location of the thermometer. If this were true, to explain the discrepancy the actual sample temperature would have to be about 18 K.

5.7 Conclusions

In this chapter a type of MRFM experiments has been described, called CERMIT, in which a force gradient, rather than a force, is responsible for the signal. Using a custom-fabricated cantilever with a spring constant of $k = 6 \times 10^{-5}$ N/m,

a sensitivity of $\mu_{\min} = 7.5 \times 10^{-21}$ J/T in a one hertz bandwidth was achieved at 4.4 K and ~ 7 T. At these experimental conditions this is equal to the Curie-law magnetic moment from 7.1×10^8 ^{71}Ga nuclei occupying $(0.44\ \mu\text{m})^3$ in GaAs, or 5×10^5 polarized proton magnetic moments. This represented, at the time of its publication, the highest sensitivity for nuclear MRFM ever reported.

Unlike the OSCAR protocol, in which a frequency shift is only observed when the spins are locked to the rf field, a single sweep is sufficient to produce a shift with CERMIT. The signal will therefore decay in a time close to T_1 rather than $T_{1\rho}$, which can give a large advantage in signal collection time, especially in cryogenic samples (see section 2.2.8). However, in general a modulated detection strategy is desired in order to avoid the noise of $1/f$ character commonly found in amplifier circuitry, as well as, in the case of CERMIT, any slow cantilever frequency drift which may be present. To achieve this a number of sweeps could be delivered at regular intervals during the signal collection period, and the output of the frequency counter (or other demodulation circuitry) could be lock-in detected. The time between sweeps should be much larger than $1/f_c$, so that a good cantilever frequency measurement can be made between the sweeps, but short enough so that the reduction in $1/f$ noise is worthwhile, say tens of Hz. As long as the periods between the sweeps were much longer than the durations of the sweeps themselves, the signal should still decay in a time similar to T_1 (since the rf is off most of the time). It seems likely that for future CERMIT experiments will be performed in this manner.

Another advantage of the CERMIT method is that it is applicable to uniform samples, i.e. it does not require an imbalance in the spin distribution as OSCAR does. This could turn out to be a valuable feature of future, few-spin

nuclear MRFM experiments. For instance, one method of achieving the large field gradients which will be required is to move back to the sample-on-cantilever configuration, and scan the tip above a planar array of nanomagnets. Such an array could be easier to create than a cantilever-mounted magnet by, say, stencil lithography [23]. The array could be fabricated with various sizes of magnets present in an easily scannable area. The experiment could be "tuned-up" by using the CERMIT protocol with a relatively large, low gradient magnet which would allow many spins to be brought into resonance. Once the external field, rf, etc. were calibrated the cantilever (with sample mounted on it) could be moved near one of the smaller magnets for high-sensitivity measurements. These would be in the statistical-polarization regime, so either CERMIT or OSCAR could be used.

APPENDIX A

SPECTRAL DENSITIES AND PARSEVAL'S THEOREM

A.1 Spectral density convention

This section gives the spectral density convention used in this thesis. Different conventions are used by different authors, usually without comment. Beware!

Let $x(t)$ be a time-dependent signal and $\hat{x}(\omega)$ be its Fourier transform. Then the *energy spectral density*[1] of x at ω is given by $|\hat{x}(\omega)|^2$. Of present interest is the *single-sided energy spectral density*, defined by

$$P_x(\omega) \equiv |\hat{x}(\omega)|^2 + |\hat{x}(-\omega)|^2 , \tag{A.1}$$

since ω and $-\omega$ are related by a phase shift, and so do not represent different frequencies in the intuitive sense. The single-sided energy spectral density extends from zero to positive infinity. If x is real (as will be the case in the laboratory) then $|\hat{x}(\omega)|^2 = |\hat{x}(-\omega)|^2$ and equation A.1 can be rewritten $P_x(\omega) = 2\,|\hat{x}(\omega)|^2$.

For a signal extending in time from $-T/2$ to $T/2$ and zero elsewhere, the *single-sided power spectral density* will be defined

$$\begin{aligned} S_x &\equiv \frac{1}{T} P_x(\omega) \\ &= \frac{2}{T} |\hat{x}(\omega)|^2 . \end{aligned} \tag{A.2}$$

For a signal of infinite duration one can use the definition

$$S_x \equiv \lim_{T\to\infty} \frac{2}{T} |\hat{x}(\omega)|^2 . \tag{A.3}$$

[1] This quantity is called the power spectral density in some books and journal articles.

The notation of a capital S with a subscript indicating the time-domain variable will be used throughout the thesis to indicate the single-sided power spectral density.

Parseval's Theorem

Let $x(t)$ represent any (complex) time-domain variable. Assume a signal of finite duration, which turns on abruptly at time $-T/2$ and off at $T/2$. In this case the mean-squared displacement can be written in terms of an infinite integral

$$\left\langle x^2 \right\rangle = \frac{1}{T} \int_{-T/2}^{T/2} x^2(t)\, dt = \frac{1}{T} \int_{-\infty}^{\infty} x^2(t)\, dt. \tag{A.4}$$

(This will be convenient in what follows.) Substituting the fourier transform for $x(t)$ into the above gives

$$\begin{aligned}
\left\langle x^2 \right\rangle &= \frac{1}{T} \int_{-\infty}^{\infty} \left[\frac{1}{\sqrt{2\pi}} \int_{-\infty}^{\infty} \hat{x}(\omega) e^{-i\omega t}\, d\omega \right] \left[\frac{1}{\sqrt{2\pi}} \int_{-\infty}^{\infty} \hat{x}^*(\omega') e^{i\omega' t}\, d\omega' \right] dt \\
&= \frac{1}{T} \frac{1}{2\pi} \int_{-\infty}^{\infty} \int_{-\infty}^{\infty} \int_{-\infty}^{\infty} \hat{x}(\omega) \hat{x}^*(\omega') e^{-i(\omega-\omega')t}\, d\omega d\omega' dt \\
&= \frac{1}{T} \int_{-\infty}^{\infty} \int_{-\infty}^{\infty} \hat{x}(\omega) \hat{x}^*(\omega') \delta(\omega - \omega')\, d\omega d\omega' \\
&= \frac{1}{T} \int_{-\infty}^{\infty} \left| \hat{x}(\omega) \right|^2 d\omega \\
&= \int_{0}^{\infty} S_x(\omega)\, d\omega,
\end{aligned} \tag{A.5}$$

This important result states that the integral of the power spectral density is equal to the mean-squared displacement, and is known as Parseval's Theorem.

REFERENCES

[1] J. A. Sidles, Applied Physics Letters **58**, 2854 (1991).

[2] L. Ciobanu, D. A. Seeber, and C. H. Pennington, Journal of Magnetic Resonance **158**, 178 (2002).

[3] A. Blank, C. R. Dunnam, P. P. Borbat, and J. H. Freed, Journal of Magnetic Resonance **165**, 116 (2003).

[4] http://www.ncbi.nlm.nih.gov/Genbank/.

[5] http://www.rcsb.org/pdb/.

[6] N. C. Nielsen, A. Malmendal, and T. Vosegaard, Molecular Membrane Biology **21**, 129 (2004).

[7] J. Drenth, *Principles of Protein X-Ray Crystallography*, Springer-Verlag, New York, 1999.

[8] K. Wüthrich, Science **243**, 45 (1989).

[9] D. P. DiVincenzo, Science **270**, 255 (1995).

[10] L. Vandersypen and I. Chuang, Reviews of Modern Physics **76**, 1037 (2004).

[11] G. P. Berman, G. D. Doolen, P. C. Hammel, and V. I. Tsifrinovich, Physical Review B **61**, 14694 (2000).

[12] G. P. Berman, G. D. Doolen, P. C. Hammel, and V. I. Tsifrinovich, Physical Review Letters **86**, 2894 (2001).

[13] G. Binnig, H. Rohrer, C. Gerber, and E. Weibel, Physical Review Letters **49**, 57 (1982).

[14] G. Binnig, C. F. Quate, and C. Gerber, Physical Review Letters **56**, 930 (1986).

[15] D. J. Griffiths, *Introduction to electrodynamics*, Prentice Hall, Upper Saddle River, New Jersey, second edition, 1989.

[16] B. C. Stipe, H. J. Mamin, T. D. Stowe, T. W. Kenny, and D. Rugar, Physical Review Letters **87**, 96801 (2001).

[17] C. L. Degen *et al.*, Physical Review Letters **94**, 207601 (2005).

[18] J. G. Kempf and J. A. Marohn, Physical Review Letters **90**, 087601 (2003).

[19] G. M. Leskowitz, L. A. Madsen, and D. P. Weitekamp, Solid State Nuclear Magnetic Resonance **11**, 73 (1998).

[20] L. A. Madsen, G. M. Leskowitz, and D. P. Weitekamp, Proceedings of the National Academy of Sciences of the United States of America **101**, 12804 (2004).

[21] CODATA (2002) value, http://physics.nist.gov/cuu/Constants/.

[22] D. R. Lide, editor, *CRC Handbook of Chemistry and Physics*, CRC Press, Boca Raton, FL, 85th edition, 2004.

[23] A. Champagne, A. Couture, F. Kuemmeth, and D. Ralph, Applied Physics Letters **82**, 1111 (2003).

[24] D. Rugar, C. S. Yannoni, and J. A. Sidles, Nature **360**, 563 (1992).

[25] O. Züger and D. Rugar, Applied Physics Letters **63**, 2496 (1993).

[26] D. Rugar *et al.*, Science **264**, 1560 (1994).

[27] O. Züger, S. T. Hoen, C. S. Yannoni, and D. Rugar, Journal of Applied Physics **79**, 1881 (1996).

[28] O. Züger and D. Rugar, Journal of Applied Physics **75**, 6211 (1994).

[29] K. J. Bruland, J. Krzystek, J. L. Garbini, and J. A. Sidles, Review of Scientific Instruments **66**, 2853 (1995).

[30] P. C. Hammel, Z. Zhang, G. J. Moore, and R. M. L., Journal of Low Temperature Physics **101**, 59 (1995).

[31] Z. Zhang, M. L. Roukes, and P. C. Hammel, Journal of Applied Physics **80**, 6931 (1996).

[32] K. Wago, D. Botkin, C. S. Yannoni, and D. Rugar, Applied Physics Letters **72**, 2757 (1998).

[33] K. J. Bruland, W. M. Dougherty, J. L. Garbini, J. A. Sidles, and S. H. Chao, Applied Physics Letters **73**, 3159 (1998).

[34] J. A. Marohn, R. Fainchtein, and D. D. Smith, Journal of Applied Physics **86**, 4619 (1999).

[35] G. E. Pake, *Paramagnetic Resonance*, W. A. Benjamin, Inc., New York, 1962.

[36] K. Wago *et al.*, Review of Scientific Instruments **68**, 1823 (1997).

[37] K. Wago, D. Botkin, C. S. Yannoni, and D. Rugar, Physical Review B **57**, 1108 (1998).

[38] B. C. Stipe *et al.*, Physical Review Letters **87**, 277602 (2001).

[39] H. J. Mamin, R. Budakian, B. W. Chui, and D. Rugar, Physical Review Letters **91**, 207604 (2003).

[40] D. Rugar, R. Budakian, H. J. Mamin, and B. W. Chui, Nature **430**, 329 (2004).

[41] A. Schaff and W. S. Veeman, Journal of Magnetic Resonance **126**, 200 (1997).

[42] A. Schaff and W. S. Veeman, Applied Physics Letters **70**, 2598 (1997).

[43] R. Verhagen, A. Wittlin, C. W. Hilbers, H. van Kempen, and A. P. M. Kentgens, Journal of the American Chemical Society **124**, 1588 (2002).

[44] K. Wago, O. Züger, R. Kendrick, C. S. Yannoni, and D. Rugar, Journal of Vacuum Science and Technology B **14**, 1197 (1996).

[45] T. A. Barrett, C. R. Miers, H. A. Sommer, K. Mochizuki, and J. T. Markert, Journal of Applied Physics **83**, 6235 (1998).

[46] K. R. Thurber, L. E. Harrell, R. Fainchtein, and D. D. Smith, Applied Physics Letters **80**, 1794 (2002).

[47] K. R. Thurber, L. E. Harrell, and D. D. Smith, Journal of Magnetic Resonance **162**, 336 (2003).

[48] S. R. Garner, S. Kuehn, J. M. Dawlaty, N. E. Jenkins, and J. A. Marohn, Applied Physics Letters **84**, 5091 (2004).

[49] Z. Zhang, P. C. Hammel, and P. E. Wigen, Applied Physics Letters **68**, 2005 (1996).

[50] Z. Zhang, P. C. Hammel, M. Midzor, M. L. Roukes, and J. R. Childress, Applied Physics Letters **73**, 2036 (1998).

[51] B. J. Suh *et al.*, Journal of Vacuum Science and Technology B **16**, 2275 (1998).

[52] V. Charbois, V. Naletov, J. Ben Youssef, and O. Klein, Journal of Applied Physics **91**, 7337 (2002).

[53] V. Charbois, V. Naletov, J. Ben Youssef, and O. Klein, Applied Physics Letters **80**, 4795 (2002).

[54] O. Klein, V. Charbois, V. Naletov, and C. Fermon, Physical Review B **67**, 220407(R) (2003).

[55] V. Naletov, V. Charbois, O. Klein, and C. Fermon, Applied Physics Letters **83**, 3132 (2003).

[56] D. Seeber, J. Hoftiezer, W. Daniel, M. Rutgers, and C. Pennington, Review of Scientific Instruments **71**, 4263 (2000).

[57] Z. Zhang and P. C. Hammel, Solid State Nuclear Magnetic Resonance **11**, 65 (1998).

[58] B. C. Stipe, H. J. Mamin, T. D. Stowe, T. W. Kenny, and D. Rugar, Physical Review Letters **86**, 2874 (2001).

[59] T. N. Ng and J. A. Marohn, IEEE Transactions on Magnetics , in press.

[60] J. A. Marohn, R. Fainchtein, and D. D. Smith, Applied Physics Letters **73**, 3778 (1998).

[61] Z. Zhang, P. C. Hammel, and G. J. Moore, Review of Scientific Instruments **67**, 3307 (1996).

[62] H. J. Mamin, R. Budakian, and D. Rugar, Review of Scientific Instruments **74**, 2749 (2003).

[63] W. M. Dougherty *et al.*, Journal of Magnetic Resonance **143**, 106 (2000).

[64] M. Löhndorf, J. Moreland, and P. Kabos, Applied Physics Letters **76**, 1176 (2000).

[65] A. Abragam, *Principles of Nuclear Magnetism*, Oxford University Press, New york, 1961.

[66] H. M. Cho, C. J. Lee, D. N. Shykind, and D. P. Weitekamp, Physical Review Letters **55**, 1923 (1985).

[67] S. H. Chao, W. M. Dougherty, J. L. Garbini, and J. A. Sidles, Review of Scientific Instruments **75**, 1175 (2004).

[68] A. N. Cleland and M. L. Roukes, Applied Physics Letters **69**, 2653 (1996).

[69] D. W. Carr, S. Evoy, L. Sekaric, H. G. Craighead, and J. M. Parpia, Applied Physics Letters **75**, 920 (1999).

[70] X. M. H. Huang, C. A. Zorman, M. Mehregany, and M. L. Roukes, Nature **421**, 496 (2003).

[71] Y. Wang, J. A. Henry, A. T. Zehnder, and M. A. Hines, Journal of Physical Chemistry B **107**, 14270 (2003).

[72] J. A. Henry, Y. Wang, and M. A. Hines, Applied Physics Letters **84**, 1765 (2004).

[73] Y. Wang, J. A. Henry, D. Sengupta, and M. A. Hines, Applied Physics Letters **85**, 5736 (2004).

[74] X. Liu *et al.*, Physica B **316**, 393 (2002).

[75] J.-H. Choi *et al.*, Proceedings of SPIE - The International Society for Optical Engineering **5389**, 399 (2004).

[76] C. Ascoli *et al.*, Applied Physics Letters **69**, 3920 (1996).

[77] T. D. Stowe *et al.*, Applied Physics Letters **71**, 288 (1997).

[78] T. D. Stowe, *Extending the lower limits of force sensisivity using micromachined silicon cantilevers*, PhD thesis, Stanford University, 2000.

[79] H. J. Mamin and D. Rugar, Applied Physics Letters **79**, 3358 (2001).

[80] T. D. Stowe, T. W. Kenny, D. J. Thomson, and D. Rugar, Applied Physics Letters **75**, 2785 (1999).

[81] J. D. Hannay, R. W. Chantrell, and D. Rugar, Journal of Applied Physics **87**, 6827 (2000).

[82] D. Mozyrsky, I. Martin, D. Pelekhov, and P. C. Hammel, Applied Physics Letters **82**, 1278 (2003).

[83] A. E. E. Rogers, S. S. Doeleman, , and J. Moran, Astronomical Journal **109**, 1391 (1995).

[84] R. Shankar, *Principles of Quantum Mechanics*, Plenum Press, New York, second edition, 1994.

[85] C. P. Slichter, *Principles of Magnetic Resonance*, Springer-Verlag, Berlin, third edition, 1990.

[86] M. Goldman, *Quantum Description of High-Resolution NMR in Liquids*, Oxford University Press, New york, 1988.

[87] N. Bloembergen, E. M. Purcell, and R. V. Pound, Physical Review **73**, 679 (1948).

[88] R. Lenk, *Brownian motion and spin relaxation*, Elsevier Scientific Pub. Co., Amsterdam, 1977.

[89] I. S. Gradshteyn and I. M. Ryzhik, *Table of Integrals, Series, and Products*, Academic Press, San Diego, CA, 1980.

[90] Veeco technical staff, private communication.

[91] J. P. Den Hartog, *Mechanical Vibrations*, McGraw-Hill, 1956.

[92] N. E. Jenkins *et al.*, J. Vac. Sci. Tech. B **22**, 909 (2004).

[93] D. Rugar, M. H. J., and G. P., Applied Physics Letters **55**, 2588 (1989).

[94] A. D. Drake and D. C. Leiner, Review of Scientific Instruments **55**, 162 (1984).

[95] P. Horowitz and W. Hill, *The art of electronics*, Cambridge University Press, New York, second edition, 1989.

[96] K. J. Bruland *et al.*, Review of Scientific Instruments **70**, 3542 (1999).

[97] R. C. Richardson and E. N. Smith, *Experimental Techniques in Condensed Matter Physics at Low Temperatures*, Addison-Wesley, 1988.

[98] E. R. Abraham and E. A. Cornell, Applied Optics **37**, 1762 (1998).

[99] L. S. Singer and C. Kikuchi, Journal of Chemical Physics **23**, 1738 (1955).

[100] C. Yannoni, private communication.

[101] F. J. Giessibl, Reviews of Modern Physics **75**, 949 (2003).

[102] H. Mamin, R. Budakian, B. Chui, and D. Rugar, 2005, Oral presentation, March Meeting of the American Physical Society.

[103] J. A. Marohn, Unpublished.

[104] T. R. Albrecht, P. Grütter, D. Horne, and D. Rugar, Journal of Applied Physics **69**, 668 (1991).

[105] Y. Martin, C. C. Williams, and H. K. Wickramasinghe, Journal of Applied Physics **61**, 4723 (1987).

[106] D. Seeber, R. Cooper, L. Ciobanu, and C. Pennington, Review of Scientific Instruments **72**, 2171 (2001).

[107] S. Kuehn, PhD thesis, Cornell University, 2006.

[108] W. R. Silveira and J. A. Marohn, Review of Scientific Instruments **74**, 267 (2003).

[109] A. Suter, D. V. Pelekhov, M. L. Roukes, and P. C. Hammel, Journal of Magnetic Resonance **154**, 210 (2002).